

**AN INTELLIGENT STAND-ALONE ULTRASONIC DEVICE FOR  
MONITORING LOCAL DAMAGE GROWTH IN CIVIL STRUCTURES**

A Thesis  
Presented to  
The Academic Faculty

by

Alexander Thomas Pertsch

In Partial Fulfillment  
of the Requirements for the Degree  
Master of Science in  
Engineering Science and Mechanics

School of Civil and Environmental Engineering  
Georgia Institute of Technology  
December 2009

Copyright © 2009 by Alexander Thomas Pertsch

**AN INTELLIGENT STAND-ALONE ULTRASONIC DEVICE FOR  
MONITORING LOCAL DAMAGE GROWTH IN CIVIL STRUCTURES**

Approved by:

Dr. Laurence J. Jacobs, Advisor  
School of Civil and Environmental  
Engineering  
*Georgia Institute of Technology*

Dr. Yang Wang, Co-Advisor  
School of Civil and Environmental  
Engineering  
*Georgia Institute of Technology*

Dr. Jin-Yeon Kim  
School of Civil and Environmental  
Engineering  
*Georgia Institute of Technology*

Date Approved: August 19, 2009

*To my parents  
in deep gratitude*

*and*

*in loving memory of my father.*

## ACKNOWLEDGEMENTS

Firstly, I would like to acknowledge my advisors Dr. Laurence “Larry” J. Jacobs and Dr. Yang Wang for their continuous help and support during my research. I thank Larry for being an outstanding advisor, teacher, friend, and one of a kind personality. His efforts enabled me to attend Georgia Tech in the first place, and his personality significantly contributed to making it a truly unique experience. I thank Dr. Yang Wang for providing me with the resources and the support I needed to succeed. Access to his lab equipment was invaluable for my research. I would also like to express my gratitude towards Dr. Jin-Yeon Kim for helping with the ultrasonic aspects of this work.

I owe a great debt of gratitude to Kyle M. French for his invaluable help and incredible patience with the design of the analog circuits for the prototype device. The prototype device could not have been built in the available time frame without his help.

Also, I am deeply indebted to Prof. Dr.-Ing. Lothar Gaul from the Institute for Applied and Experimental Mechanics at the University of Stuttgart for giving me this unique opportunity by establishing this exchange program. The financial and organizational support provided by the German Academic Exchange Service (DAAD) is greatly appreciated.

Most importantly, I would finally like to express my utmost appreciation to my family and my friends. Your enduring and unprecedented support and encouragement always has been and always will be invaluable to me, and enabled me to successfully complete my studies. I’m especially grateful to my parents, who always encouraged me to find my own way.

# TABLE OF CONTENTS

DEDICATION . . . . .	iii
ACKNOWLEDGEMENTS . . . . .	iv
LIST OF TABLES . . . . .	vii
LIST OF FIGURES . . . . .	viii
LIST OF SYMBOLS AND ABBREVIATIONS . . . . .	x
SUMMARY . . . . .	xii
I INTRODUCTION . . . . .	1
1.1 Motivation and Background . . . . .	1
1.2 Research Objectives . . . . .	4
1.3 Structure of this Thesis . . . . .	5
II HARDWARE AND SOFTWARE LAYOUT OF THE ULTRASONIC DETECTION DEVICE . . . . .	7
2.1 Overview of the Device’s Functionality . . . . .	7
2.2 Overview of the Hardware Used for the Device . . . . .	9
2.3 Sequence of Actions and Interaction Between Different Modules During Ultrasonic Measurements . . . . .	13
2.4 Booting and Memory . . . . .	15
2.5 Wireless Communication . . . . .	16
2.6 Signal Generation Using Pulse-Width-Modulation Signals . . . . .	21
2.6.1 Generation of a 1 MHz Sine Wave Signal Using PWM . . . . .	22
2.6.2 Generation of a Burst Signal Using the PWM Module . . . . .	24
2.6.3 Output Amplification Circuit . . . . .	26
2.7 Analog-Digital Conversion . . . . .	32
2.7.1 Delay Between Start of Output Signal and Start of Sampling . . . . .	33
2.7.2 Signal Conditioning Circuit . . . . .	34
2.7.3 Sampling Registers and DMA Data Transfer . . . . .	45
2.8 Signal Processing and Data Compression . . . . .	46
2.8.1 Fourier Transform and Fast Fourier Transform . . . . .	47

2.8.2	Envelope Detection with the Hilbert transform . . . . .	52
2.8.3	Calculation of the Discrete-Time Hilbert Transform . . . . .	55
2.8.4	Data Compression and Wireless Transfer . . . . .	59
2.8.5	Cyclic Redundancy Check (CRC) Checksum . . . . .	64
2.9	Power Consumption and Cost of the Device . . . . .	65
2.9.1	Power Consumption . . . . .	65
2.9.2	Cost of the Device . . . . .	67
III	THEORETICAL AND PRACTICAL BACKGROUND FOR RAYLEIGH WAVE MEASUREMENTS IN STEEL SPECIMENS . . . . .	69
3.1	Wave Propagation in Elastic Solids . . . . .	69
3.1.1	Linear Elasticity and the Wave Equation . . . . .	70
3.1.2	Propagation of Plane Longitudinal and Shear Waves . . . . .	71
3.1.3	Reflection and Refraction of Plane Waves at Interfaces . . . . .	72
3.1.4	Propagation of Rayleigh Waves . . . . .	75
3.2	Generation of Rayleigh Waves Using Contact Wedges . . . . .	77
3.3	Crack Detection Using Rayleigh Waves . . . . .	83
IV	ULTRASONIC MEASUREMENTS: EXPERIMENTS AND RESULTS . . . . .	87
4.1	Test Specimen and Measurement Procedure . . . . .	88
4.2	Results of Measurements Taken with Commercial Ultrasonic Equipment	90
4.3	Influence of Sampling on the Ultrasonic Signals . . . . .	93
4.4	Results of Measurements Taken with the Prototype Device . . . . .	98
V	CONCLUSION AND FURTHER WORK . . . . .	101
5.1	Conclusion . . . . .	101
5.2	Outlook on Further Work . . . . .	103
5.3	Contribution and Impact . . . . .	105
APPENDIX A	ANALYSIS OF THE SIGNAL CONDITIONING CIRCUIT . . . . .	106
APPENDIX B	PROGRAM CODE . . . . .	108
REFERENCES	. . . . .	110

## LIST OF TABLES

1.1	Scheduled inspection intervals for bridges in the U.S. in 2008 . . . . .	2
2.1	Measured power consumption of the ultrasonic device . . . . .	66
2.2	Cost of the main active components of the ultrasonic device . . . . .	68
3.1	Approximate material properties for steel (cf. [1, Table 4.1]) . . . . .	72
4.1	Dimensions of the notches cut into the test specimen . . . . .	89
4.2	Amplitude ratios, direct signal over mode converted reflected signal for measurements taken with commercial equipment . . . . .	93
4.3	Comparison of the absolute amplitudes of original vs. downsampled signal for measurement series no. 1 . . . . .	95
4.4	Comparison of the amplitude ratios original vs. downsampled signal for measurement series no. 1 . . . . .	97
4.5	Amplitude ratios, direct signal over mode converted reflected signal for measurements taken with the prototype device . . . . .	100

## LIST OF FIGURES

2.1	Overview of the functionality of the device . . . . .	8
2.2	Overview of the parts of the device . . . . .	9
2.3	Photos of the circuit boards that are part of the device. . . . .	11
2.4	Interaction between different modules during measurements . . . . .	14
2.5	Memory mapping on the <i>TMS320F28335</i> DSP (Source: [39, p. 35]) . . . . .	17
2.6	Pulse-width-modulation signal . . . . .	21
2.7	Frequency spectrum of a square wave and frequency response of a transducer	23
2.8	Principle of the output signal generation . . . . .	25
2.9	Schematic of the output amplification circuit . . . . .	28
2.10	Power supply for the output amplification circuit . . . . .	28
2.11	Electric input and output signals of the output amplifier circuit for a 5 cycle square wave burst input with transducer attached. . . . .	30
2.12	Comparison of the output amplifier signal with resulting wave form . . . . .	31
2.13	Sampled attenuated output signal and comparison with continuous square wave . . . . .	34
2.14	Power supply for signal conditioning circuit . . . . .	36
2.15	Signal conditioning circuit . . . . .	37
2.16	Frequency response of the low-pass filter . . . . .	39
2.17	Measured amplitude of the frequency response of the amplifier circuit . . . . .	41
2.18	Input and output of the amplification circuit for a sinusoidal input of 1 MHz. . . . .	42
2.19	Influence of noise and signal distortions in the signal conditioning circuit to the ADC output for a constant input of 150 mV to the signal conditioning circuit . . . . .	43
2.20	Influence of noise and signal distortions in the signal conditioning circuit to the ADC output for a 1 MHz sinusoidal input to the signal conditioning circuit with 300 mV amplitude . . . . .	44
2.21	Data transfer using the DMA controller . . . . .	46
2.22	Computation scheme for an 8-point decimation-in-time in-place FFT . . . . .	49
2.23	Signal with envelope curve obtained from the Hilbert transform of the downsampled signal ( $f_s = 3.125$ MHz) . . . . .	58
2.24	Example for a noisy measurement signal with two signal bursts . . . . .	60

2.25	Repacking of 12-bit data into 8-bit packets for transmission . . . . .	61
2.26	C-Code for repacking of 12-bit data into 8-bit packets . . . . .	62
2.27	Data structure for the transfer of the samples to the server . . . . .	62
3.1	Reflection and refraction of waves at an interface . . . . .	73
3.2	Generation of Rayleigh waves using a contact transducer and a wedge . . .	78
3.3	Different coupling wedges and the resulting time domain signals . . . . .	80
3.4	Measured propagation times for different propagation distances for a Rayleigh wave in steel. . . . .	82
3.5	Scattering of Rayleigh waves at a surface crack . . . . .	84
3.6	Conversion of a Rayleigh wave to a bulk wave at the bottom of a crack . . .	85
4.1	Test specimen with notches made using electric discharge machine . . . . .	88
4.2	Ultrasonic examination of notches in test specimen . . . . .	89
4.3	Ultrasonic measurement signals in the time domain for different notch depths, taken with commercial ultrasonic equipment. . . . .	91
4.4	Downsampled and quantized ultrasonic measurement signal for 1.2 mm deep notch . . . . .	94
4.5	Ultrasonic measurement signals in the time domain for different notch depths, taken with the prototype device. . . . .	99
A.1	Amplifier with offset correction . . . . .	106
A.2	Filter circuits . . . . .	107
B.1	Yong's [53] bit reversal algorithm, adapted for complex numbers . . . . .	108
B.2	Pseudo-code for the complex FFT algorithm . . . . .	109

## LIST OF SYMBOLS AND ABBREVIATIONS

ADC	Analog-digital converter
bps	Bits per second
CRC	Cyclic redundancy check
CPV	Caucy principal value of an improper integral
dBi	Forward gain of an antenna in decibels compared to the hypothetical isotropic antenna
DMA	Direct memory access
DFT	Discrete Fourier transform
DoT	Department of Transportation
DSP	Digital signal processor
EDM	Electrical discharge machining
FFT	Fast Fourier transform
FHSS	Frequency hopping spread spectrum
FHWA	Federal Highway Administration
FPU	Floating point unit
IDFT	Inverse discrete Fourier transform
IEEE	Institute of Electrical and Electronics Engineers
ISM radio band	Industrial, scientific and medical radio band
JTAG	Joint Test Action Group
MOSFET	metal-oxide semiconductor field effect transistors
NBI	National Bridge Inventory
PWM	Pulse width modulation
SARAM	Single access random access memory
SHM	Structural health monitoring
SNR	Signal-to-noise ratio
SRAM	Static random access memory

<i>TMS320F28335</i>	Model number of the Texas Instruments DSP
UART	Universal asynchronous receiver/transmitter
U.S.	United States
XINTF	External memory interface of the <i>TMS320F28335</i>
$c_T, c_L, c_R$	Shear, longitudinal and Rayleigh wave speed in steel
$c_W$	Longitudinal wave speed in the wedges
$C_i$	Capacitance or capacitor
$\mathcal{F}$	Fourier transform; capital letters denote functions in the frequency domain
$f$	Frequency
$f_{\text{cutoff}}$	Cutoff frequency of the low-pass filter
$f_{\text{Nyquist}}$	Nyquist frequency, $f_{\text{Nyquist}} = f_s/2$
$f_s$	Sampling frequency/sampling rate of the ADC, $f_s = 8.3334 \text{ MHz}$
$\mathcal{H}$	Hilbert transform
$j$	Imaginary unit, $j^2 = -1$
$k$	Index in the frequency domain (context: signal processing)
$k$	Wave number (context: wave propagation), $k = \omega/c$
$n$	Index for sequences in the time domain
$N$	Number of samples
$R_i$	Resistance or resistor
$T$	Signal period, $T = 1/f$
$V$	Voltage
$x[n], y[n]$	Discrete time sequences in the time domain, e.g. sampled signals
$X[k], Y[k]$	DFTs of the sequences $x[n], y[n]$
$\omega$	Angular frequency, $\omega = 2\pi f$

Symbols only used in one section or chapter are explained in their context and are not included in this list.

## SUMMARY

Throughout the decades of its life cycle, civil infrastructure is exposed to adverse environmental conditions and mechanical loading, which may gradually cause deterioration of its condition. Damage that arises can interfere with the safe use of the structure. The intervals between regular scheduled human inspections are typically too long to detect critical deterioration in a timely manner. Therefore, a continuous structural health monitoring (SHM) methodology is desirable. Existing approaches for continuous SHM are suitable for monitoring a structure's global condition, but they are insensitive to local damage. If such damage grows at locations that are crucial to a structure's stability, it may lead to a catastrophic failure, which is often associated with a significant number of fatalities. Ultrasonic examination techniques are well-established for manual inspection of local damage, but today's commercially available equipment is not suitable for permanent deployment due to its size, weight and power requirements.

This research investigates how ultrasonic damage monitoring can be implemented on a small, battery-powered, self-contained device. The device is intended for the continuous monitoring of surface breaking cracks in steel using Rayleigh waves. This study presents in detail the challenges that are to be considered for ultrasonic monitoring, with the objective to provide a foundation for the future development of a fully autonomous monitoring device.

The study at hand proposes a hardware and software layout suitable for ultrasonic measurements. A prototype device is built using a *Texas Instruments TMS320F28335 digital signal processor*, a *Digi 9XCite OEM RF wireless transceiver*, and custom amplification circuits. Using two *Panametrics A103S narrowband ultrasonic contact transducers* in a pitch-catch setup and appropriate contact wedges, the wave field that arises from scattering of an incident tone burst wave at a crack is measured. The resulting output signals

are acquired by an analog-digital converter (ADC), and the envelope curve of the samples is obtained using the Hilbert transform. A data analysis algorithm uses this envelope curve to extract wave burst signals from the samples in order to minimize the data that is to be transmitted. Additional compression of this data and the implementation of a communication protocol allow for a reliable and efficient wireless transmission.

In order to demonstrate the feasibility of the proposed ultrasonic examination method, measurements of notches in a steel plate with different depths are taken. Data obtained from experiments using commercial ultrasonic equipment is downsampled to match the device's specifications, and the influence of the sampling distortions on the signals are analyzed. Data from these experiments is compared to the results of measurements taken with the prototype device. The scope of this study is limited to a qualitative analysis of the experimental results; quantitative methods to determine the dimensions of a crack or notch from measured ultrasonic data are not included.

The research conducted demonstrates that taking ultrasonic measurements with a small, self-contained device is feasible. The proposed hardware and software layout ensures fast data acquisition with reliable timing and a predictable, low delay. Comparison of frequency-based to time-based signal analysis methods yields the conclusion that frequency-based methods are preferable, as they are affected less by sampling effects. The experimental results show that the intended ultrasonic examination technique can be used for qualitative damage assessment. For quantitative assessments, the effects of sampling have to be taken into account. Although a possible output amplification circuit is presented which can be used for measurements with the desired wave bursts, its efficiency needs further improvement. Generation of large amplitude output signals to obtain a suitable signal-to-noise ratio remains a major challenge of the device. Measurements of the power consumption illustrate the need to implement low-power sleep states when the device is inactive in order to prevent a fast depletion of the battery supply.

The knowledge gained in this study contributes to improving the safety of civil infrastructure. Continuous local damage monitoring as proposed helps to detect critical conditions in-time, and to take countermeasures to avoid catastrophic failures.

# CHAPTER I

## INTRODUCTION

### *1.1 Motivation and Background*

The service life time of civil infrastructure is typically on the order of several decades. During this period, the infrastructure is exposed to adverse environmental conditions and mechanical loading, which may gradually cause deterioration in the structure's condition. While some damage may be harmless and does not interfere with the safe use of the structure, infrequent failures of civil infrastructure with often fatal consequences, like the collapse of the I35W Mississippi river bridge, demonstrate the risks that are associated with slow degradation in civil structures. This study proposes a new concept for ultrasonic monitoring of damage growth in steel, which can be applied to a variety of civil structures.

As an example for the ongoing degradation of civil infrastructure, bridges in the United States of America are considered. As of December 2008, the National Bridge Inventory (NBI)<sup>1</sup> lists a total of 71,469 bridges as structurally deficient<sup>2</sup> [45]. Considering that close to 50 % of the over 600,000 bridges listed in the NBI have been built before 1969 and thus are more than 40 years old, with close to 60,000 (or roughly 20 %) of these already classified as structurally deficient (cf. data given in [46]), the number of "structurally deficient" bridges is likely to increase in the future. The situation is even worse for the roughly 85,000 bridges that have been built before 1939, which constitute about 14 % of the bridges in the U.S.: slightly more than 30 % of them currently are classified as structurally deficient.

These example figures demonstrate the need for a regular inspection of bridges, for

---

<sup>1</sup>The Federal Highway Administration (FHWA) of the United States Department of Transportation (U.S. DoT) maintains data about bridges "located on public roads, including Interstate Highways, U.S. highways, State and county roads, as well as publicly-accessible bridges on Federal lands" in the NBI [43].

<sup>2</sup>"Structural deficiencies are characterized by deteriorated conditions of significant bridge elements and reduced load-carrying capacity." [47]

which the *U.S. Code of Federal Regulations, Title 23, Section 650.301* sets forth standards for the U.S. The prescribed intervals between mandatory inspections vary depending on different factors, which include previous damage and the load that the bridges are subject to. Table 1.1 lists the actual inspection intervals for different bridges as they are listed in the NBI for the year 2008. Only about 10% of the bridges are inspected once a year, and the majority of roughly 85% are inspected every other year.

These regularly scheduled inspections mainly consist of visual inspections, which are time- and labor-intensive; the results obtained from visual inspections are subjective, and the classification of damage varies significantly among different examiners, as a recent study [29] of the FHWA shows. Visual inspections also only have the potential to detect damage at the surface, other damage may remain undetected. To obtain reliable and objective results, many structural health monitoring (SHM) techniques have been proposed (e.g. [8,11,36]). One possible approach for SHM calculates the modal response of a structure based on stress, strain, or acceleration data acquired by a network of sensors that are spread over the structure. Changes in the modal behavior can be used to assess the structural health of the structure. However, these global approaches are insensitive to local failures, and may miss the growth of local damage, which – if the damage grows at structurally critical points – may lead to catastrophic consequences. Thus, global SHM approaches need to be supplemented with local approaches to increase their sensitivity, one of which is examined in this study.

The use of ultrasonic waves for damage detection in solid materials is a well-established local examination technique. Current ultrasonic methods are suitable and regularly used

**Table 1.1:** Scheduled inspection intervals for bridges in the U.S. in 2008

Interval (months)	No. of bridges	Percentage
12	61733	10.06 %
24	518867	84.57 %
48	30688	5.00 %
other	2268	0.37 %

(compiled from data of the National Bridge Inventory, U.S. Department of Transportation [44])

for manual human inspections. Literature references, which present some examination techniques for the assessment of cracks using Rayleigh waves, will be given in the introduction to Chapter 3.3. However, commercial ultrasonic equipment usually depends on the connection to a power grid or a comparably-high energy source. Devices currently used for the ultrasonic measurement setup, which normally includes at least one pulser or other signal generator and one data acquisition device, are due to their size, weight, and cost not suitable for a permanent deployment on a structure for continuous monitoring. However, continuous monitoring is desirable in the 24 month interval that typically occurs between inspections, which may exceed the critical time frame during which cracks grow to a critical size. Shorter intervals for human inspections are not feasible due to the associated labor costs. Also note that these 24 month bridge inspections typically don't make use of ultrasonic examination techniques.

Existing SHM systems for the short-term inspection of a civil structure usually consist of a central data acquisition device, to which the sensors are wired. Such a centralized approach requires running long cables from the data acquisition device to the sensors all over the structure, which is expensive in terms of both time and money. Installation of such a tethered SHM system typically makes up for over 75% of the total testing time [38]. Considering the costs, Çelebi approximates typical expenses for an SHM system of \$1,000 per sensing channel with additional costs of \$2,000 per channel for the installation [7]. As one alternative, Straser and Kiremidjian [38] demonstrate the feasibility and cost-effectiveness of wireless SHM systems in order to reduce the costs associated with the installation of tethered systems. Wang et al. [50–52] develop a distributed sensor network, which consists of multiple compact, self-contained data-acquisition and processing devices that run off batteries and that communicate over a wireless connection, which eliminates the need for cabling. Lynch, Wang et al. [22, 49] demonstrate that the performance of this device in field tests is comparable to the performance of a commercial tethered system.

The SHM approaches presented so far typically only require sampling rates on the order of several tens to hundreds of Kilohertz to acquire data, as the signal frequencies

of the modal responses of structures normally lie in the Hertz to low KiloHertz range. Ultrasonic signals, however, by definition are signals with frequencies above 20 kHz, and signals in practice typically have frequencies in the range 500 kHz–20 MHz. Therefore, for ultrasonic measurements, data must be acquired at much higher frequencies than those necessary for global SHM approaches.

Most SHM systems are passive devices as far as the measured data is concerned. This means, these systems only measure signals that are generated by other sources. Active ultrasonic testing, however, requires the generation of ultrasonic wave signals. The response to these known excitations is recorded and used for damage assessment. A strong excitation signal will yield a strong output signal and a good signal-to-noise ratio. However, limited to batteries as power supply, a compromise between signal quality and power requirements must be found.

## *1.2 Research Objectives*

This study investigates how ultrasonic detection methods can be implemented on a small, battery-powered, self-contained device based on a digital signal processor (DSP), which uses a wireless link to communicate with a central server. For the ultrasonic examination of surface breaking cracks in steel, Rayleigh waves with a frequency of 1 MHz are used. The work conducted during this study serves as a foundation for future research efforts towards the goal of a fully autonomous ultrasonic detection device. Therefore, the main focus of this study is to present in detail the challenges that have to be considered for the development of such a device. Although building a prototype is part of this study, the development of a ready-to-market device is beyond the scope of this work. In particular, the objective of this research is

1. to find suitable components and assemble them in a hardware setup, which can be used to continuously monitor steel components for damage in an economically feasible fashion,
2. to investigate a method for efficient Rayleigh wave generation and detection with this hardware using contact transducers to obtain a reasonable signal-to-noise ratio,

3. to investigate the effects of a limited sampling rate and resolution on the detected signals, and the impacts on the signal's capability to indicate damage in the material,
4. to develop a software layout that allows for fast data acquisition with reliable timing and a predictable, low delay,
5. to implement basic data analysis algorithms on-board, which allow for an efficient data compression for wireless transmission, and which can also be used as basis for the development of autonomous damage assessment algorithms, and
6. to adhere to limits in power supply as imposed by the use of batteries.

To illustrate the feasibility of the proposed ultrasonic measurements, experiments are conducted with a test specimen, in which notches of different depths have been cut. Measurements are taken with commercial ultrasonic equipment and then converted to match the sampling rate and resolution of the proposed device to separate effects of sampling and quantization from noise and other imperfections in the device. The results from these measurements are compared to measurements taken with the prototype device. The scattered field of Rayleigh waves at these notches is measured on the opposite side of a notch. However, this research does not examine the theoretical behavior of Rayleigh waves at cracks, nor does it derive a quantitative relation between the measured signals to the notch dimensions; with regard to the signals of the scattered wave field, the scope is limited to a phenomenological explanation of the observed features.

### ***1.3 Structure of this Thesis***

An introduction to the research conducted and background information has been given in this chapter, and the research objectives have been stated. Chapter 2 introduces the hardware and software layout of the proposed device in depth, and gives the technical details for all parts of the device. The second chapter also presents the signal processing algorithms implemented, and shows how data is compressed and packed for wireless transmission. It ends with considerations about the power consumption and cost of the hardware used. Chapter 3 gives the theoretical background for wave propagation in

elastic solids and explains the generation of Rayleigh waves in steel in the setup used. It also illustrates, from a qualitative view, the expected features observed in a Rayleigh wave signal that is scattered at a notch. Chapter 4 describes the experimental procedure, presents the results of ultrasonic measurements, and examines the effects of sampling and quantization on the signals. The study ends with the conclusions and an outlook on further work in Chapter 5.

## CHAPTER II

### HARDWARE AND SOFTWARE LAYOUT OF THE ULTRASONIC DETECTION DEVICE

This chapter presents details on the physical and functional layout of the ultrasonic measurement device. First, a general overview of the device's functionality is given. Next, an overview on the hardware layout of the device is presented, and the device is described by its sub-parts or modules, each with its own individual function. An overview of the interaction of different modules during ultrasonic measurements is provided, which helps to understand the significance of the in-depth technical details of each module presented thereafter. The proposed signal processing algorithm and data transmission protocol is introduced, and the chapter concludes with an analysis of the power consumption and an estimation of the cost of the device.

#### *2.1 Overview of the Device's Functionality*

The general task description for the ultrasonic device, "to monitor the crack growth in steel," can be broken into two main tasks: data acquisition from ultrasonic measurements, and data processing. Aside from these two tasks, the wireless communication with the server is an important supplemental function for the device.

Figure 2.1 gives an overview of the device's functionality. Starting with the booting process, the device and its peripherals are initialized, which essentially means that peripheral configuration registers are set to appropriate values. Next, if the device is booting from flash, code that might be later used while the device runs, is copied from flash to single access random access memory (SARAM). Additional information about this booting process and the use of memory will be provided in Section 2.4. After the successful initialization, the device waits for incoming server commands, handles them upon receipt and calls the appropriate functions. The device only acts on the server's request, which

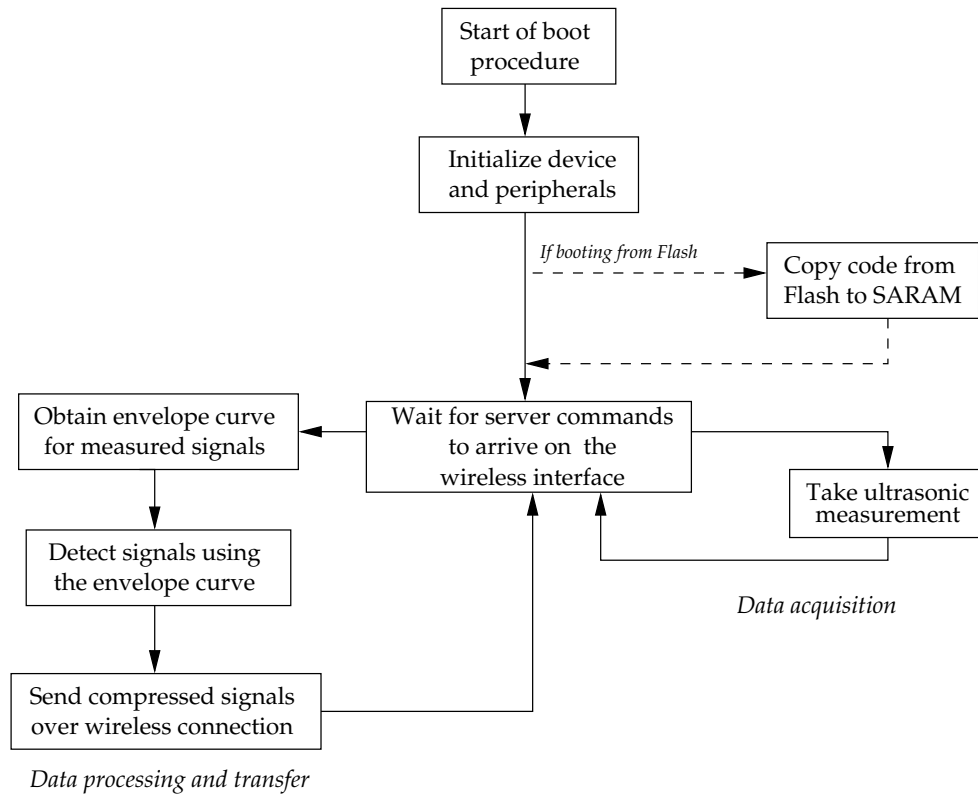


**Figure 2.1:** Overview of the functionality of the device

gives the server full control over the device’s function. As an example, the server can request the device to acquire new data, in which case the device makes an ultrasonic measurement. The necessary steps for such a measurement are outlined in Section 2.3. After data has been acquired, the next server command will typically be to process the data on-board. In the current prototype, the data processing consists of calculating the envelope signal based on the Hilbert transform, extracting burst signals based on this envelope curve, and finally packing the data and transmitting it to the server over the wireless connection. The proposed signal processing method is presented in Section 2.8.

After this brief introduction to the basic functional layout of the device, an overview of the physical components with their most important characteristics is given in the next section, before all sub-modules of the device will be explained in detail.

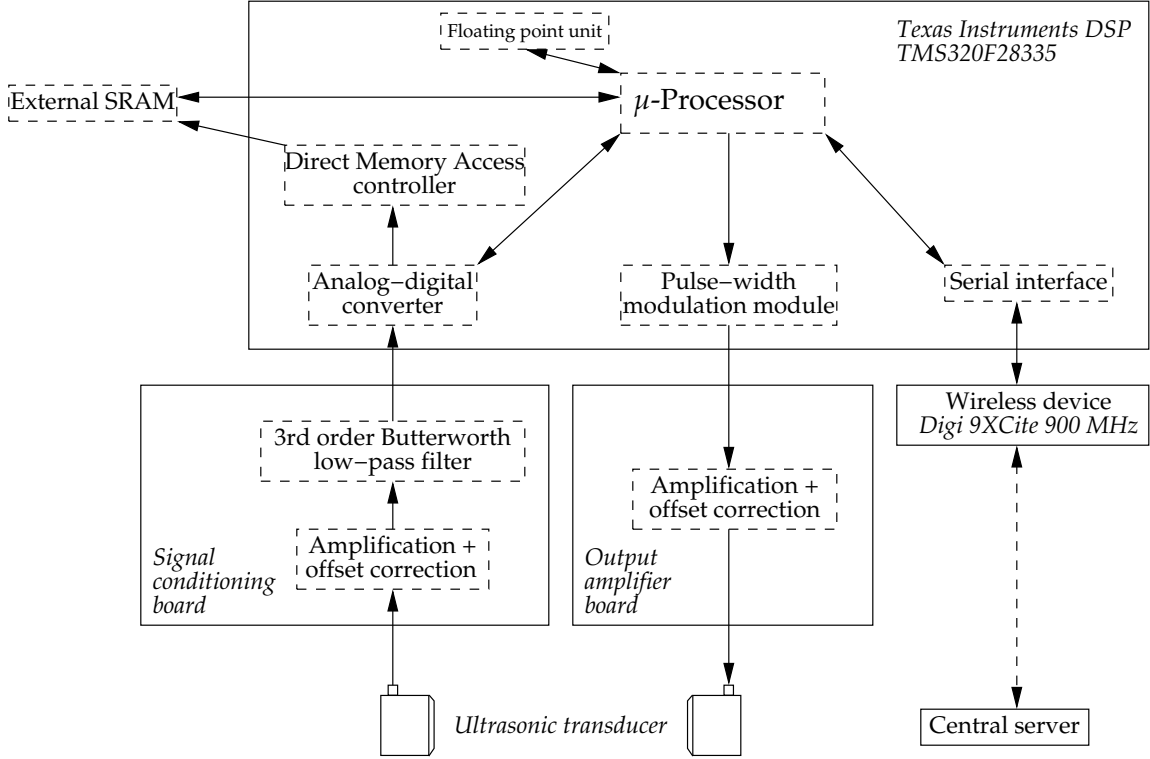


**Figure 2.2:** Overview of the parts of the device

## 2.2 Overview of the Hardware Used for the Device

The ultrasonic detection device is built around a *Texas Instruments Digital Signal Processor (DSP) TMS320F28335* as its main component. Aside from the computational core (CPU, central processing unit) with single precision (32-bit, IEEE 754) floating point unit (FPU), this DSP<sup>1</sup> also includes several additional functional modules on-chip; of these, the analog-digital converter (ADC), the pulse-width modulation (PWM) module, the Direct Memory Access (DMA) controller, the external memory interface (XINTF) and the serial interface are used in this project. Figure 2.2 illustrates, how the modules build up the ultrasonic device.

The *TMS320F28335* includes  $256\text{ K} \times 16\text{ bit}$  flash and  $34\text{ K} \times 16\text{ bit}$  single access RAM (SARAM) on-chip [39]. Access to SARAM generally is faster than to flash memory, but

<sup>1</sup>In this thesis, the Term “DSP” for “digital signal processor” will be used as synonym for the physical *TMS320F28335* chip with all included modules. “CPU” and “microprocessor” will be used interchangeably as references to the computational core.

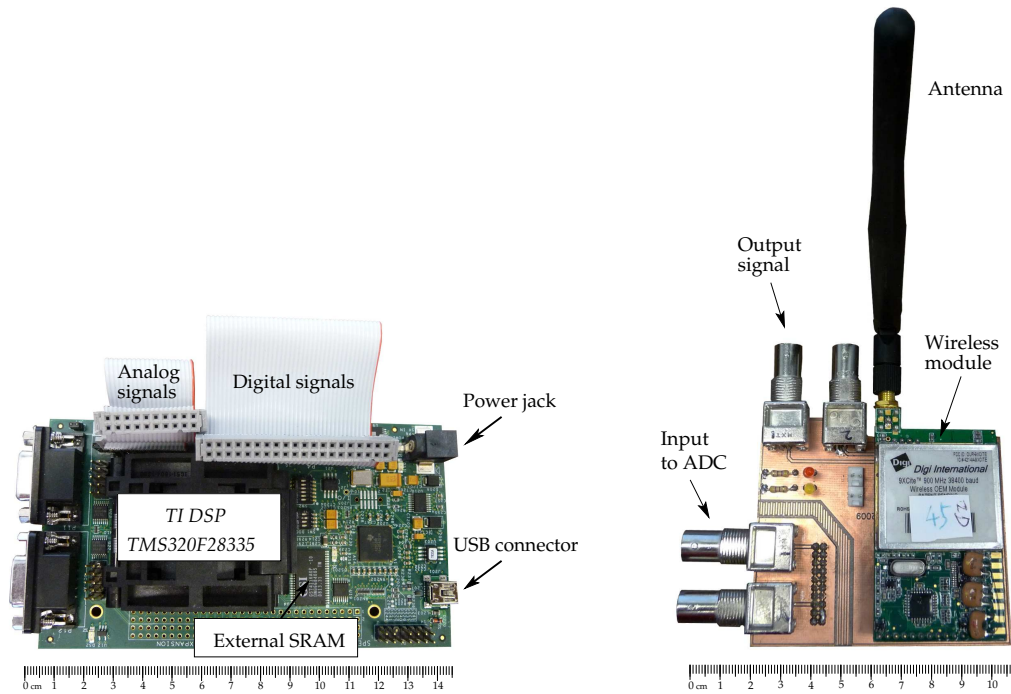
since flash is a non-volatile memory, it offers the advantage of keeping its stored content when the device is powered off. The device can boot from either SARAM or the flash memory; more details on the memory use is provided in Section 2.4. The *TMS320F28335* DSP supports 96 individual interrupts, which are grouped into blocks of eight by a multiplexer and fed into one of 12 core interrupt lines. The CPU responds quickly to these interrupts: it only takes nine CPU cycles for the corresponding interrupt routine to be called [42]. In the ultrasonic device, interrupts are used to send commands between different modules and the CPU.

The prototype ultrasonic device is built using an *eZdsp<sup>TM</sup> F28335* evaluation board, which is shown in Figure 2.3a. The board includes the power supply for all components, a JTAG controller for programming and debugging the *TMS320F28335* chip, connectors to attach external circuitry, and an external SRAM chip with  $256\text{K} \times 16\text{bit}$  memory<sup>2</sup>. Despite the fact that the external SRAM has  $256\text{K} = 2^{18}$  physical memory addresses, only  $2^{17} = 128\text{K}$  are accessible on the *eZdsp<sup>TM</sup> F28335* board, as only 17 address lines are routed between the microprocessor and the external SRAM. Therefore, the external SRAM will subsequently be referred to by its usable memory size  $128\text{K} \times 16\text{bit}$ .

Two flat ribbon cables are connected to the *eZdsp<sup>TM</sup> F28335* board, providing links to external devices. The left 20-wire cable in Figure 2.3a carries the analog signals, the right 40-wire cable carries the digital signals and the power supply voltage for the wireless module. These cables are connected to a custom designed connector board, shown in Figure 2.3b, which provides a socket to attach the *Digi 9XCite OEM RF* wireless transceiver module to, and which routes the input and output signals from the ribbon cables to BNC connectors. The ultrasonic device is currently designed for one-channel operation. However, the connector board has four BNC connectors, two each for the input and the output sides, so that the device can be enhanced to two-channel operation without replacing the connector board.

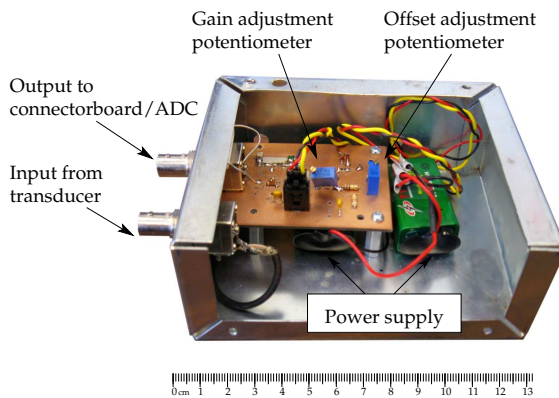
---

<sup>2</sup>In computer science, the prefix K commonly means  $2^{10} = 1024$ , which should not be confused with the SI-prefix k for  $10^3$ . The same is valid for  $\text{M} \triangleq 2^{20}$ ,  $\text{G} \triangleq 2^{30}$ , etc.

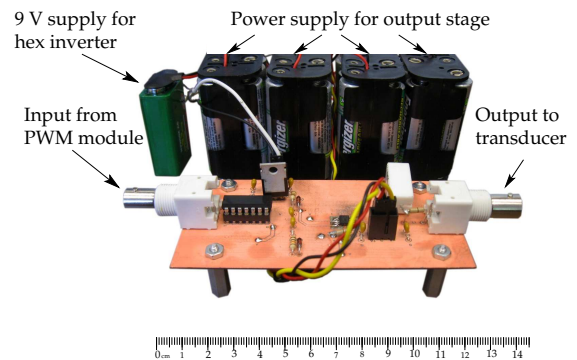


(a) *eZdsp™ F28335* evaluation board

(b) Connector board with wireless module attached



(c) Signal conditioning board



(d) Output amplification board

**Figure 2.3:** Photos of the circuit boards that are part of the device. The flat ribbon cables in the top left picture (a) are connected to matching pin-header sockets on the bottom side of the connector board (b). Connection between the connector-board (b) and the signal conditioning board (c) resp. the output amplification board (d) are made using standard coaxial cables with  $50\ \Omega$  impedance.

The *Digi 9XCite OEM RF* wireless transceiver module provides two-way communication with a central server. Data transfer between the transceiver and the wireless module uses a serial communication protocol with a data rate of 38400 bps (bits per second). The wireless module can send and receive data over a distance of up to 90 m indoors or in urban environments, and up to 300 m line-of-sight distance outdoors. More details about the wireless module will be given in Section 2.5.

Output signals to create Rayleigh waves in the material are generated using the pulse-width modulation (PWM) module. This module generates a square wave which alternates between a “high” and a “low” level with a configurable duty cycle. By changing this duty cycle, i.e. the percentage of time during which the signal is on the “high” level during one base period, the average voltage of the output PWM signal can be varied between the “low” and the “high” level. In the ultrasonic device, the PWM module is used to generate a signal with the base frequency 1 MHz and a fixed duty cycle of 50%. The resulting output signal, a 1 MHz square wave with 3.3 V amplitude and 1.65 V offset, is amplified by the output amplification board shown in Figure 2.3d, and sent to the ultrasonic transducer, which converts the alternating voltage signal into a mechanical wave. Chapter 2.6 provides details about generating the output signal using the PWM module, and Chapter 3 describes how Rayleigh waves are generated in the material.

After passing through the material, the ultrasonic wave is received by a second transducer, which generates an alternating voltage signal proportional to the physical vibration. The resulting voltage signal is amplified and offset-corrected by a signal conditioning circuit shown in Figure 2.3c. The offset free signal from the transducer is shifted to a mean value of approximately 1.5 V so that it completely lies inside the 0–3 V input range of the analog-digital converter (ADC) module. An analog 3<sup>rd</sup> order active Butterworth filter with a cutoff frequency  $f_{\text{cutoff}} = 2.5 \text{ MHz}$  is included in the signal conditioning circuit to prevent aliasing effects in the sampled signal. The signal conditioning board is placed inside a separate metal casing to shield it from electromagnetic interference caused by other parts of the device or outside sources, in order to reduce the noise on the amplified analog signal. After passing through the signal conditioning board, the analog signal is

fed into the analog-digital converter (ADC) module, which provides a 12 bit-resolution over its input range of 0–3 V. The ADC includes a sample-and-hold circuit and is configured to run at a sample rate of 8.3334 MHz. Sampled values are stored in one of the 16 ADC result registers, which form a circular buffer, i.e. after a value has been written to the last register, the next value will be written to the first one, overwriting the existing value. To save the data before it is overwritten, the Direct Memory Access (DMA) controller continuously transfers the sampled values from the buffer to the external SRAM. DMA transfers bypass the microprocessor, so that the transfer can not be stalled by a high CPU load or an interrupt handling routine, as long as concurrent memory access is avoided. This ensures that the transfer will finish in time. Details about the sampling process and the data transfer are given in Chapter 2.7.

Most of the different tasks that the device performs only involve some of the modules of the device. Only the most demanding task, taking the ultrasonic measurements, involves all modules (except for the FPU). The next chapter therefore describes how the different modules interact during this task. The overview given in the next section will clarify how the modules interact, which helps to understand the more detailed information presented in the successive chapters.

### ***2.3 Sequence of Actions and Interaction Between Different Modules During Ultrasonic Measurements***

Figure 2.4 illustrates the sequence of events that occur during an ultrasonic measurement, with all modules except for the FPU involved:

1. The central server sends the command to start the measurement. This command is received by the wireless module and passed on to the microprocessor, which translates it into the appropriate function calls.
2. The microprocessor enables the clock signal to the PWM module; the PWM module starts generating the output square wave signal.
3. The PWM module instructs the ADC to start the sampling process. This signal does not pass through the CPU. After receiving this signal, the ADC starts sampling the

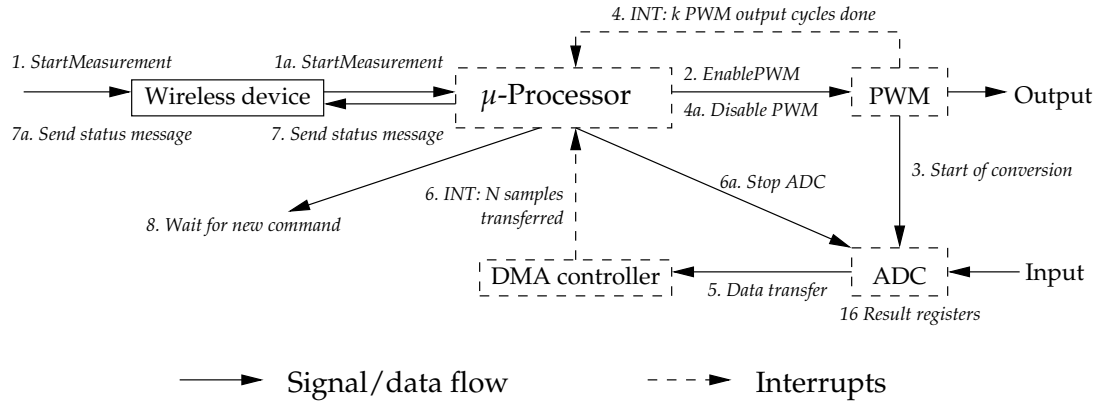


**Figure 2.4:** Interaction between different modules during measurements

input channel at the preconfigured sampling rate, and stores the sampled output sequentially into one of its 16 result registers.

4. After a configurable number of  $k$  signal cycles have been generated by the PWM module, the PWM module sends an interrupt signal to the CPU. The appropriate interrupt handling routine forces the output to low level and then disables the clock to the PWM module which stops the output signal.
5. Meanwhile, after each 8 data points that have been sampled, the ADC signals the DMA controller to transfer these samples from the ADC result registers to the external SRAM. While data is transferred, the ADC continues sampling to the other 8 result registers. As the DMA transfer bypasses the CPU, interrupt requests like the PWM interrupt do not interfere with the data transfer.
6. The DMA controller is configured to transfer only  $N$  samples. After  $N$  samples have been transferred, the DMA controller generates an interrupt request to the CPU and the corresponding interrupt service routine stops the sampling process. As the data transfer is stopped after  $N$  samples, delays in switching off the ADC are of no consequences as only values in the ADC result registers are overwritten, but none in the SARAM.
7. After switching off the ADC, the microprocessor sends a status signal over the wireless connection to the central server.

8. The microprocessor then goes back into the wait state and waits for the next server command.

The collaboration of the different device modules over different separate signal paths enables the device to provide a sufficiently fast performance so that ultrasonic measurements can be taken. If all actions had to be controlled only by the CPU, a much faster running processor would be required to achieve the desired timings. The ADC sampling and data transfer would pose hard realtime requirements to the microprocessor.

## **2.4 Booting and Memory**

As mentioned in Chapter 2.2, the *TMS320F28335* possesses a total of  $34\text{ K} \times 16$  bit internal single access random access memory (SARAM), and  $256\text{ K} \times 16$  bit internal flash memory. SARAM can be read and written during normal operation. Flash can only be read by the device, and can only be written using a special programming interface, which is included in the *eZdsp<sup>TM</sup> F28335* board. Flash memory offers the advantage of being non-volatile, i.e. it holds its content even when the power supply is turned off. SARAM only keeps its content as long as the device is continuously powered, after a power cycle the contents are lost. So for a power-independent operation, any program code and pre-initialized variables have to be written into the flash code while values that are calculated or acquired during operation go into SARAM.

The *TMS320F28335* offers the option to boot from either SARAM or flash memory, which can conveniently be used when developing code. As long as a continuous power supply is guaranteed, the program code can be written into SARAM, which is a lot faster than erasing and reprogramming flash memory. This allows for a rapid test of changes in program code during development. After the program code has been compiled, the linker decides which parts of the program code are mapped into which physical memory locations on the target device [28]. For the ultrasonic device, a set of linker configuration files has been created, which allows for the switch between writing the program code into flash or SARAM. The booting target from which to load the program code is determined by the logic state of four input pins of the DSP chip. On the *eZdsp<sup>TM</sup> F28335* board, a

hardware switch is used to set the input pins either to “high” or to “low” level. The *eZdsp<sup>TM</sup> F28335* data manual [37, p. 2-24] lists how the possible combinations are mapped to the different booting targets.

As established before, for power-cycle proof operation, the program code has to be written to the non-volatile flash memory. However, read operations from flash are slower than from SARAM. For time-critical code, like interrupt handler routines, this longer access time might delay the microprocessor’s response noticeably. Therefore, all time-critical code like interrupt routines should be copied from flash to SARAM before they are executed [40]. As the ultrasonic device saves sampled data to the external SRAM, the internal SARAM provides adequate space to copy not only interrupt routines, but all functions which might be called after the initialization of the device is completed. This ensures a fast device operation and minimizes delays during execution. Additionally, after copying the code to SARAM, the flash memory can be powered down, which reduces the power consumption of the device.

Not only are the flash and the SARAM accessible over the memory interface, but also all peripheral registers and the external interface are mapped to one of the 4 M memory addresses which the DSP can address. As all peripherals are treated similarly to regular memory, no special CPU commands are necessary for CPU input-output operations, which reduces the complexity of the set of CPU commands. Figure 2.5 shows the memory mapping on the *TMS320F28335* (cf. [39, p. 35]).

## ***2.5 Wireless Communication***

For the wireless communication with the central server, the ultrasonic device includes a commercial *Digi 9XCite OEM RF Module*. As established before, this module provides communication with a continuous data stream of up to 38400 bps over a distance of up to 90 m indoors or up to 300 m outdoors line-of-sight with its 2.1 dBi<sup>3</sup> dipole antenna attached. The module with attached antenna is shown in Figure 2.3b. The wireless

---

<sup>3</sup>(forward) gain of an antenna in dB compared to the hypothetical isotropic antenna, which uniformly radiates energy in all directions

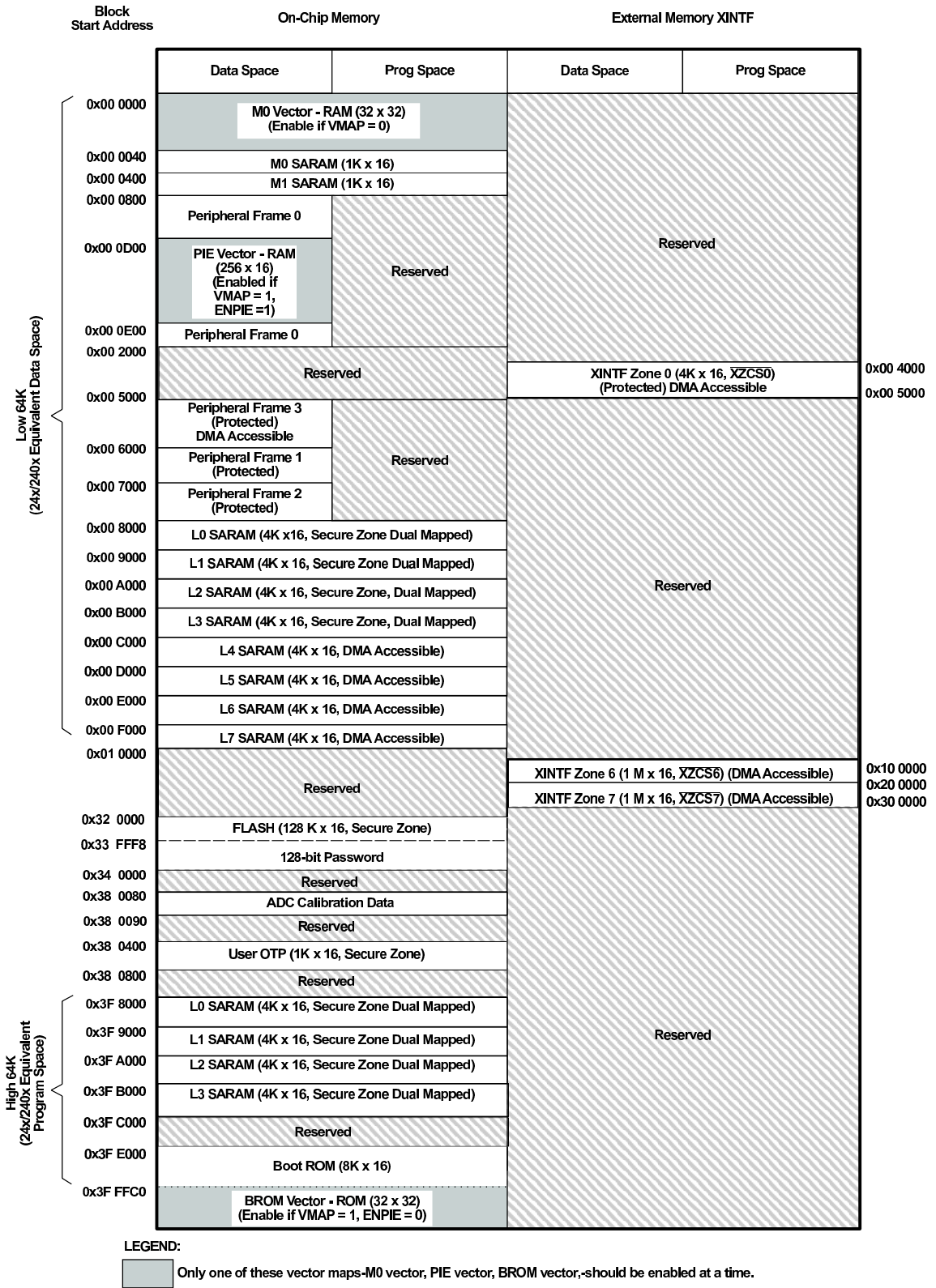


Figure 2.5: Memory mapping on the TMS320F28335 DSP (Source: [39, p. 35])

transceiver operates with a transmit power of 4 mW in the 902–928 MHz ISM (industrial, scientific and medical) radio band, which allows unlicensed operation in North America, Australia and Israel [10]. The wireless communication device specifically is certified for use in the USA by the U.S. Federal Communications Commission (FCC) and for Canada by the Industry Canada (IC) [26]. Radio operation in the 900 MHz ISM radio band restricts the device to be used only in the mentioned countries, but in return 900 MHz devices typically offer longer range, lower power and lower cost communication compared to 2.4 GHz devices, which could be used worldwide [10].

The wireless module can operate on up to 25 different frequencies in the ISM radio band, which are spaced 300 kHz apart from each other. In fixed frequency mode, in which the transceiver only uses one carrier frequency, each of these 25 frequencies can be used as a possible communication channel. However, since each channel occupies a 500 kHz bandwidth, adjacent channels overlap, which can lead to interference problems between different devices operating in close range. Interference is a common problem on the unlicensed ISM radio band. To reduce the influence of interfering signals, the wireless module can also use one of 7 channels in a “hopping channel mode.” In this mode, the device uses Frequency Hopping Spread Spectrum (FHSS) technology to transfer data. In FHSS transmissions, the carrier frequency is rapidly switched among different known base frequency channels, using a pseudo-random sequence which both the transmitter and receiver know. As the transmission is spread over a range of distinct frequencies, it is less prone to narrow-band interference, which is to be expected in an unlicensed radio band in an uncontrolled environment. Therefore, the use of the FHSS mode is preferable over a single-frequency mode during field experiments.

Besides distinct transmission channels, the *9XCite* wireless module uses two more addressing layers: the vendor identification number (VIN) and the destination address. An incoming packet is first checked if the vendor identification number of this package matches the receiving radio’s VIN. The upper half of the 16 bit VIN is factory set, whereas the lower half can be configured, which enables multiple radios in the vicinity to be separated into different networks. Next, the packet is checked if the transmitter’s and

the receiver's channels match. As a third step, the destination address is checked. Each packet contains the transmitting radio's destination address. A receiving radio accepts the package if the transmitting and the receiving radio's destination addresses match. If any of these verification steps fails, i.e. either VID, channel or destination address does not match, the package is discarded. If a wireless device needs to communicate with different radios – as the central server in this research does – it can set its destination address to match the other radio's address, in order to establish a point-to-point communication channel. In the current design for the ultrasonic device, data transfer is always initiated by the central server. The ultrasonic device only responds to the server's requests, so a point-to-point communication is suitable; collisions between packets sent by different devices are avoided as only one device is allowed to communicate at a time. However, if active message transmission initiated by the ultrasonic devices is desired in the future, the server's wireless unit can be configured to listen to several devices, by setting an appropriate netmask. If the result of a bitwise and-conjunction of the transmitter's (in that case any ultrasonic device) destination address and the receiving (server) radio's netmask matches either the receiving radio's destination address or its netmask, the package is accepted [25]. However, the packet's destination address is not passed on by the receiving wireless module, so the sending ultrasonic device has to identify itself as part of the transmitted data.

Communication between the *TMS320F28335* DSP and the *9XCite* wireless module is realized using a serial data transfer protocol. The CPU writes data to, and reads data from its serial interface module (UART module, universal asynchronous receiver/transmitter), to which the serial interface of the wireless module is connected to, in 1 byte (8 bit) packets. Packets are transmitted over the serial line with one start, one stop, and no parity bit. The chosen serial data rate of 38400 bps equals the RF transmission rate of the wireless radio. If the serial data rate exceeded the actual transmission data rate, flow control would have to be implemented, which is so rendered unnecessary.

When receiving data on the serial interface for transmission, the wireless transmitter groups the data into packets of up to 64 bytes each, adds the header data and a cyclic

redundancy check (CRC) checksum, and then transmits the data [25]. Calculation of the CRC checksum will be explained in Section 2.8.5. The checksum is used to detect erroneous data transmission. When receiving packets over the wireless link, the *9XCite* module only accepts packets which contain the correct CRC checksum. If the checksum is correct, the data is passed on to the serial output; if the checksum is incorrect, the package is dropped. The *9XCite* does not ask for a retransmission if a package is dropped, so the application has to ensure that the data has been successfully received. In the current design, communication between the server and the ultrasonic device mainly consists of the server sending commands and the device replying with the respective status message. Additionally, for the implementation of the prototype device, all measurements and transactions are assumed to be initiated by a human operator at the server. Therefore, an incorrectly transmitted or missing command or status message will be detected by the human operator, who can solve the problem by re-sending the request. An equivalent error handling mechanism can be implemented in the server software when the operation shall be independent from a human operator: if the status message of the device does not arrive at the server in the expected time frame, the server resends the command. The only operation, when a transmission error might not be detected that easily is when the server polls the sampled data from the client. For this case, a communication protocol has been developed, which is described in Section 2.8.4.

While the wireless module transmits data, it consumes about 55 mA current when powered with a 2.85 V supply, and while receiving data, the consumed current is about 45 mA [26]. To minimize the power consumption, the wireless device can be sent into a pin sleep mode by asserting the appropriate input pin, during which it consumes only about 20  $\mu$ A. It can only be woken up by de-asserting the sleep pin. While the device is in the pin sleep mode, the server has no access to the ultrasonic device until the wireless module is re-enabled by the microcontroller. The ultrasonic radio also offers a cyclic sleep mode, during which it repeatedly checks for incoming data in a user-selectable wake-up interval. Between these intervals, the device goes into sleep mode. Possible intervals range from 0.5 s up to 16 s, and the wireless module typically consumes about 76  $\mu$ A

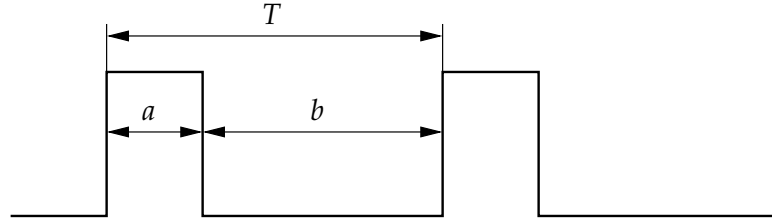


**Figure 2.6:** Pulse-width-modulation signal

while sleeping. When the device operates in this cyclic sleep mode, a wake-up signal has to precede each newly initiated communication. This signal has to be longer than the wakeup interval, to make sure that data is received reliably. So a longer sleep interval decreases the power consumption of the device, but also increases the response time to server requests. For the prototype device, the sleep mode has only been tested so far; as the possible use of sleep modes has to be designed in tandem with the future server for a fully automatic measurement system, the decision which sleep states will finally be used in which ways has not yet been made.

## 2.6 Signal Generation Using Pulse-Width-Modulation Signals

The *TMS320F28335* DSP contains six enhanced pulse-width-modulation (PWM) modules, each of which has two channels and so can generate two PWM output signals [41]. A typical PWM signal consists of a series of pulses, which can – depending on the type of PWM signal – be located at the beginning, center, or the end of a PWM signal period, which is the inverse of the PWM frequency. In each period, the PWM module outputs one analog value as average voltage over the period by switching between the “high” and the “low” state at the appropriate time. An example of a PWM signal with period  $T$  is shown in Figure 2.6. The average value of the output signal during the period  $T$  is determined by the duty cycle  $\alpha$ , which is defined as the percentage of time during which the signal is on the “high” state divided by the signal period  $T$ . For the signal in Figure 2.6, the duty cycle is

$$\alpha = \frac{a}{a + b} = \frac{a}{T}. \quad (2.1)$$

The average voltage of a PWM signal that alternates between  $V_{\text{high}}$  and  $V_{\text{low}}$  during one cycle, which is without loss of generality assumed to start at  $t = 0$ , is

$$V_{\text{avg}} = \int_{t=0}^T V(t) dt = \int_{t=0}^{\alpha T} V_{\text{high}} dt + \int_{t=\alpha T}^T V_{\text{low}} dt = \alpha T V_{\text{high}} + (1 - \alpha) T V_{\text{low}}. \quad (2.2)$$

If, like for the *TMS320F28335*, the lower logic level is 0 V, the average voltage is simply given as  $V_{\text{avg}} = \alpha T V_{\text{high}}$ . The output signal can be smoothed using a low-pass filter, which eliminates the high-frequency signal content, including the PWM base frequency.

This chapter explains how the output voltage signal is generated that will be fed into the transmitting transducer. The transducer converts the electric signals into mechanical signals in the form of longitudinal waves. Chapter 3 explains how the longitudinal waves are converted into Rayleigh waves, which are used for the measurements in this study.

### 2.6.1 Generation of a 1 MHz Sine Wave Signal Using PWM

Alter [3] described how the PWM module of a similar DSP can be used as a digital-analog-converter (DAC) to generate a desired output signal by changing the duty cycle and therefore changing the average voltage over time. However, he only considered signals of much lower frequency than the desired output signal for the ultrasonic device, a 1 MHz tone burst signal. With the system clock at 150 MHz, the PWM module can not operate fast enough to generate that signal by alternating the duty cycle.

Instead, the PWM signal generates a 1 MHz square wave burst. The offset-shifted square wave of 50% duty cycle

$$s(t) = \begin{cases} V_{\text{ss}} & kT \leq t < \frac{2k+1}{2}T \\ 0 & \frac{2k+1}{2}T \leq t < (k+1)T \end{cases}, \quad k \in \mathbb{N} \quad (2.3)$$

can be described by its Fourier series

$$\hat{s}(t) = \frac{a_0}{2} + \sum_{k=1}^{\infty} a_k \cos(k\omega_0 t) + \sum_{k=1}^{\infty} b_k \sin(k\omega_0 t), \quad (2.4)$$

with the angular frequency  $\omega_0 = 2\pi f_0 = 2\pi/T$ . The DC component is given as

$$a_0 = \frac{2}{T} \int_0^T s(t) dt = \frac{2}{T} V_{\text{ss}} \int_0^{\frac{T}{2}} 1 dt = V_{\text{ss}}, \quad (2.5a)$$

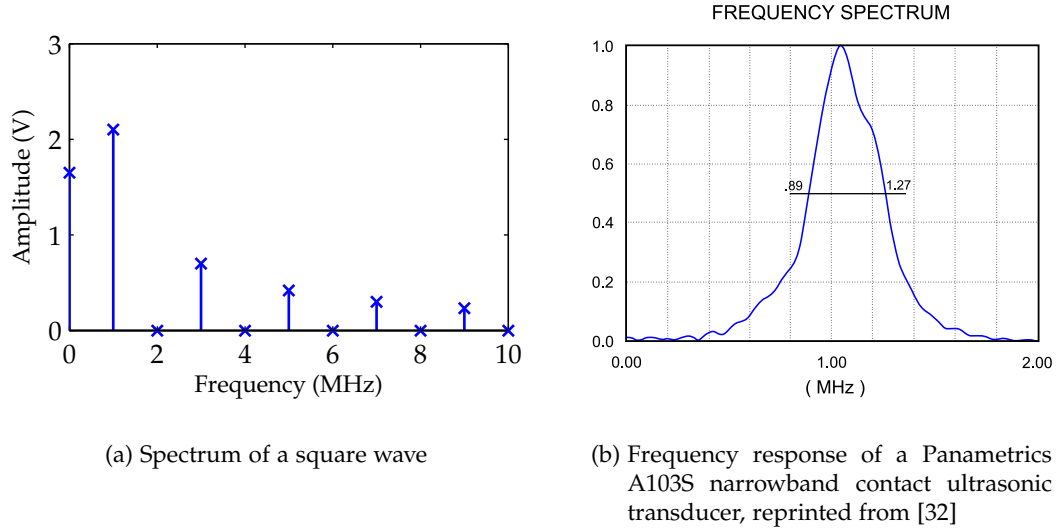


**Figure 2.7:** Frequency spectrum of a square wave and frequency response of a transducer

and the Fourier coefficients at frequencies  $k\omega_0$  are given as

$$a_k = \frac{2}{T} \int_0^T s(t) \cos(k\omega_0 t) dt = \frac{2}{T} V_{ss} \int_0^{\frac{T}{2}} \cos(k\omega_0 t) dt = 0 \quad (2.5b)$$

$$\begin{aligned} b_k &= \frac{2}{T} \int_0^T s(t) \sin(k\omega_0 t) dt = \frac{2}{T} V_{ss} \int_0^{\frac{T}{2}} \sin(k\omega_0 t) dt = \frac{2}{T} V_{ss} \left[ -\frac{1}{k\omega_0} \cos(k\omega_0 t) \right]_0^{\frac{T}{2}} \\ &= \frac{1}{k\pi} V_{ss} \left[ (-1)^{k+1} + 1 \right] = \begin{cases} \frac{2}{k\pi} V_{ss} & k \text{ odd} \\ 0 & k \text{ even.} \end{cases} \end{aligned} \quad (2.5c)$$

It is not surprising, that the Fourier series of the square wave signal consists only of sine terms. All cosine terms vanish, as a mean-free square wave signal is an odd function, i.e. it is point symmetric to the origin, and the offset-shift of  $s(t)$  only contributes to the DC component  $a_0$ . The frequency spectrum of the signal  $s(t)$  can directly be deduced from the signal's Fourier series

$$\hat{s}(t) = V_{ss} \left[ \frac{1}{2} + \frac{2}{\pi} \sum_{k=1,3,\dots}^{\infty} \frac{\sin(k\omega_0 t)}{k} \right]. \quad (2.6)$$

The frequency spectrum, shown in Figure 2.7a, only has non-zero values at zero frequency and at odd integer multiples of the base frequency  $f_0$  resp.  $\omega_0$ . To obtain a sinusoidal waveform of 1 MHz, the square wave signal can be band-pass filtered with a filter, for which 1 MHz lies inside the pass band, and which eliminates the DC offset and attenuates the 3 MHz and higher frequency content. This filter does not necessarily have

to be an electric filter. To generate Rayleigh waves, narrow-band transducers are used in this research, which act as mechanical band-pass filters. An example frequency response of such a transducer is plotted in Figure 2.7b. This frequency response shows that the DC component and signals above 2 MHz are filtered out by the transducer. Not including an electrical band-pass filter allows for an easy adaption of the device to possible future uses with other signal frequencies, as only the transducer must be changed, but not the electric band-pass filter.

While the method of filtering out the fundamental oscillation from a square wave signal allows for a simple signal generation using the on-board PWM unit of the *TMS320F28335* DSP, one inherent drawback of the method is that even with an ideal filter, which has no attenuation in the pass band, and regardless of whether the filter is electrical or mechanical, the maximum amplitude of the filtered sinusoidal 1 MHz output signal is only  $2/\pi = 63.7\%$  of the square wave's signal amplitude. While the optimal use of power is a core requirement for the self-contained ultrasonic device, which may make this loss of signal amplitude seem unappealing, it should be kept in mind that an external signal generation chip, which could directly generate a sine wave, would consume additional power, add to the cost of the device, and also make the design of a printed circuit board more complicated as signals from the microprocessor would have to be routed to the signal generation chip. Also, whereas generating a constant sine wave is not as complicated, the generation of the desired tone burst signal requires the output signal to be switched off after the end of the tone burst, which requires a fast response of an external signal generation chip. Additionally, the sampling process of the ADC has to be started with a reliable delay, which is simpler when generating the output signal on the *TMS320F28335* DSP instead of on an external chip. The following section describes how this burst signal can be generated using the on-chip PWM module.

## 2.6.2 Generation of a Burst Signal Using the PWM Module

Two of the six PWM units of the *TMS320F28335* collaborate to generate a tone burst signal of 1 MHz and  $k$  cycles. The first module, referred to as the "signal channel," is

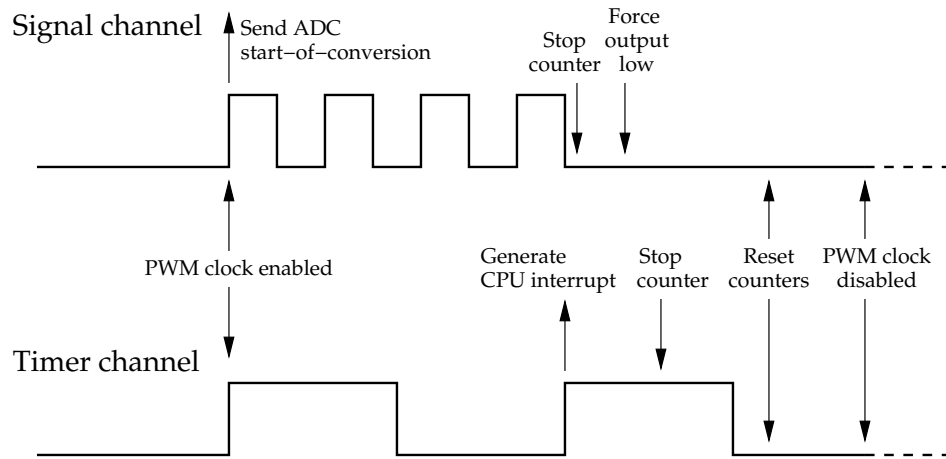


**Figure 2.8:** Principle of the output signal generation. Timing of the events after generation of the CPU interrupt are in the correct sequence, but the time delays are not to scale.

used to generate a basic output square wave of 1 MHz, and the second channel, called “timer channel,” provides the timing for when to switch the signal channel off. Figure 2.8 illustrates the wave forms generated by the two channels.

The basic frequency of a PWM signal is specified as an integer multiple of clock cycles of the CPU clock frequency. To generate a 1 MHz square wave on the *TMS320F28335* which runs at 150 MHz, the PWM output will toggle after each 75 clock cycles. This yields the desired PWM period of 150 times the system clock, i.e. 1 MHz. In theory, the PWM period for the timer channel could be set to  $k$  times the basic frequency, so that after one period of the timer channel, the output can be switched off. For this, the timer channel generates a CPU interrupt, and the appropriate interrupt service routine disables the PWM output. However, there is a slight delay from the generation of the interrupt until the interrupt service routine can disable the output. The *TMS320F28335* needs 9 CPU cycles to save critical CPU registers and to fetch the interrupt vector, after which the interrupt service routine is executed [42], and executing the interrupt service routine further adds to the delay. In experiments, the total delay has been found to be approximately 280 ns; therefore, the PWM timer channel’s period has been purposely shortened by 45 system clock cycles, or 300 ns, which is enough to reliably switch off the PWM output signal after the desired tone burst length.

Figure 2.8 illustrates the described sequence of events. Both output signals are enabled at the same time, and their period counters start to run. The PWM sends a start-of-conversion signal to the ADC, which then starts sampling its input. After one period of the timer channel, this channel generates the CPU interrupt. In the interrupt service routine, the counter of the PWM output signal is stopped, which stops the signal from toggling. When the counter is stopped, the signal is supposed to be in the low state. To ensure that the system is in the low state even if an additional short delay should have given the signal time to switch back to the high level when the channel's clock is stopped, the output is forced to low after stopping the PWM. This ensures that for the next tone burst signal generation, the signal will again start with a rising flank at the desired start time. After the output has been forced to the low state, the counter of the timer channel is stopped, reset, and the entire PWM module is disabled.

### 2.6.3 Output Amplification Circuit

The burst signal, which is generated by the PWM module as described in the preceding chapter, alternates between 0 V and 3.3 V, i.e. the signal amplitude is 3.3 V with an offset of 1.65 V. However, to generate wave signals with a better signal-to-noise ratio, stronger signals are required. Therefore, an external amplification circuit is used, which is intended for boosting the output signal to a level of approximately  $\pm 18$  V, a supply voltage that is provided by a set of stacked batteries. The output amplification or boost circuit is shown in Figure 2.9. This circuit is based on the schematic given in [17], which is adapted to work on the desired power levels and with the capacitive load of a piezoelectric transducer.

In the output boost circuit, the input first passes the driver stage consisting of a *74LS04* hex inverter. This chip includes six (therefore the term "hex") separate logical inverters, components for which for an input on logic "high" level leads to an output on "low" level and vice versa. Here, the *74LS04* is used to boost the 3.3 V input signal of the circuit to a 5 V level, which is required to drive the metal-oxide semiconductor field effect transistors (MOSFET) in the output stage. For that, all six inverters are connected in parallel to divide the load equally among all six inverters. The *74LS04* requires a stable 5 V power

supply, which is provided by a 9 V battery and a 7805 power regulator. The capacitors  $C_3$  and  $C_4$  in the power supply circuit, which is shown in Figure 2.10a, dampen noise and voltage ripples on the power supply lines.

After passing through the hex inverter, the PWM signal enters the power stage of the boost circuit. This power stage is built symmetrically, with the upper half being active during the positive output signal half-cycle, and the lower half during the negative output signal half-cycle. The two halves only differ by the type of MOSFET transistor used: a p-channel enhancement mode transistor in the upper, and a n-channel enhancement mode transistor in the lower half. MOSFETs control the current flow from source (S) to drain (D) with the voltage applied at their gate (G). If the gate-source voltage  $V_{GS}$  is positive and exceeds the transistor's threshold voltage  $V_{th}$ , i.e. the gate is at a higher voltage level than the source, an n-channel enhancement mode MOSFET starts to conduct current from source to drain. Vice versa, for a p-channel enhancement mode, current is conducted if the gate-source voltage falls below  $-V_{th}$ , i.e. the gate is at a lower voltage level than the source. The following analysis only considers the upper half of the circuit; these considerations can equally be applied to the lower half.

First, consider the case when the lower terminal of  $C_1$  is on the high level of the driver stage, i.e. a 5 V potential is active. Due to the voltage difference between the +18 V supply potential and the 5 V potential, the capacitor  $C_1$  is charged over the resistor  $R_1$ . Assuming the charging starts at  $t = 0$ , the voltage over the capacitor is

$$v_{C_1}(t) = 13 \text{ V} \left( 1 - e^{-\frac{R_1 C_1}{t}} \right). \quad (2.7)$$

When the capacitor  $C_1$  is sufficiently loaded, so that the gate-source potential of  $N_3$  exceeds the negative threshold voltage,  $V_{GS} > -V_{th}$ , with  $V_{th} \approx 1.6 \text{ V}$ , the p-channel MOSFET  $N_3$  switches off. The source-gate voltage is given as  $v_{GS}(t) = 5 \text{ V} + v_{C_1}(t) - 18 \text{ V}$ . With the time constant  $\tau = R_1 C_1 = 1 \text{ ms}$ , the switch-off voltage is reached after  $477 \mu\text{s}$ . Thus, the time constants are large compared to the signal period of  $1 \mu\text{s}$ , and once the capacitor is sufficiently loaded, its main purpose is only to decouple the DC voltages in the positive output part of the circuit from the DC voltages in the driver stage, the charge

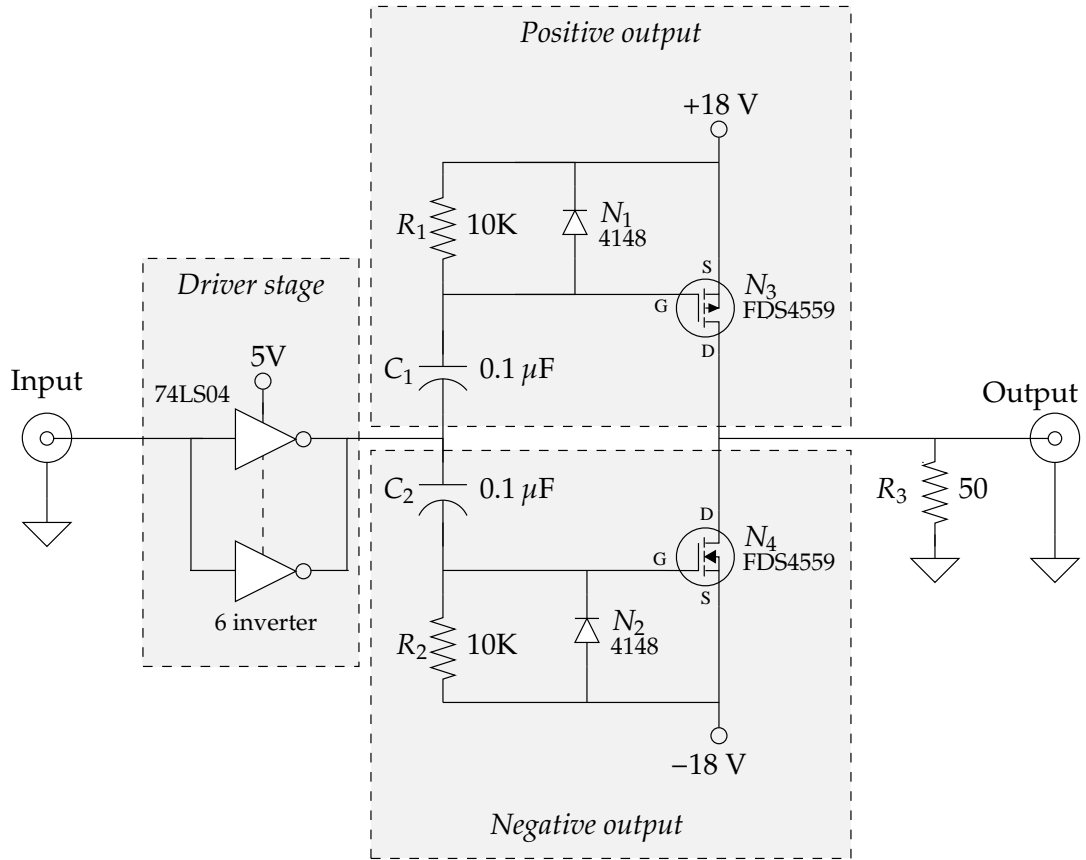
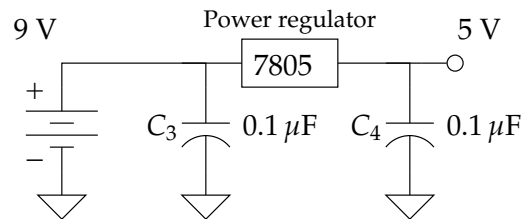
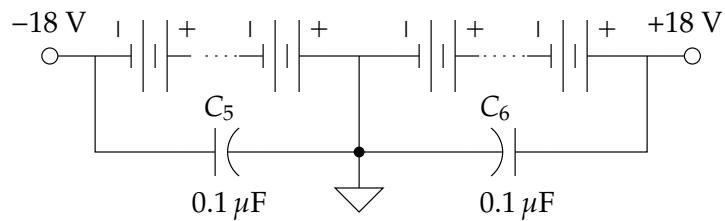


Figure 2.9: Schematic of the output amplification circuit



(a) 5 V supply for hex inverter



(b)  $\pm 18$  V supply for output push-pull stage

Figure 2.10: Power supply for the output amplification circuit

or discharge of  $C_1$  during one signal period is negligible.

Next, assume the voltage output of the driver stage switches from 5 V down to 0 V, which corresponds to a rising edge on the input signal. As the potential on the lower terminal of  $C_1$  drops by the same amount, but the charge on and therefore also the voltage across  $C_1$  remains unchanged, the potential at the gate of  $N_3$  drops by 5 V. As a consequence, the gate-source voltage  $V_{GS}$  drops below the negative threshold voltage and the MOSFET  $N_3$  builds a channel between source and drain, i.e. is switched on, and the output of the circuit switches to +18 V.

When the output of the driver stage switches back to +5 V, the potential at the top terminal of  $C_1$  rises by 5 V, which causes the gate-source voltage to exceed the negative threshold voltage, i.e.  $V_{GS} > -V_{th}$ . The p-channel MOSFET switches off. Diode  $N_1$  helps enhancing the switch-off time and rapidly lowers the gate potential to approximately 18.7 V, which is one diode voltage drop above the supply voltage 18 V.

The circuit is intended to drive the output transducer, a piezo device, which is a predominantly capacitive load. A capacitive load charges and discharges slowly in the presence of DC current. To avoid distortions in the output, the resistor  $R_3$  provides a path to ground for the DC current, and so allows for a fast response of the transducer. The resistance of  $R_3$  is chosen to match the nominal impedance of the transducer. Note that as long no alternating current enters the input of the amplification circuit, both MOSFETs  $N_3$  and  $N_4$  inhibit current flow, thus no current can flow through resistor  $R_3$  and no energy is dissipated.

Figure 2.11 compares the input and the output signal of the amplification circuit for a 5 cycle square wave input generated by a signal generator. This input signal is similar to the signal that the PWM interface generates. Aside from the first signal peak, no significant delay occurs between the rising or falling edges of the input and the output and signal. Rising edges in the input signal with their associated positive signals peaks are amplified to the desired output level. Falling edges in the input signal, however, do not pull the output to the desired low level. Aside from the short negative peak, the output stays close to ground instead of at the desired negative output level. It is assumed,

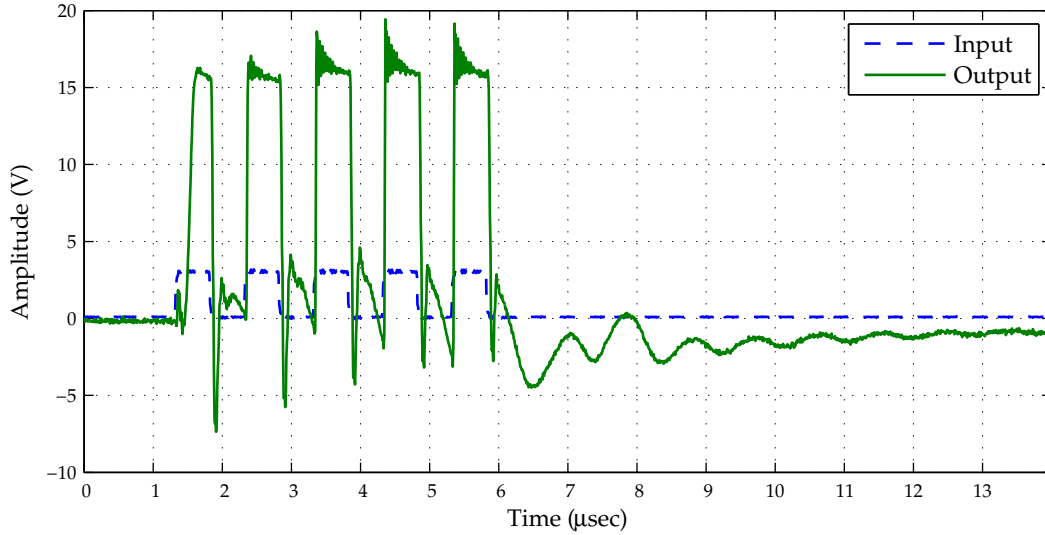
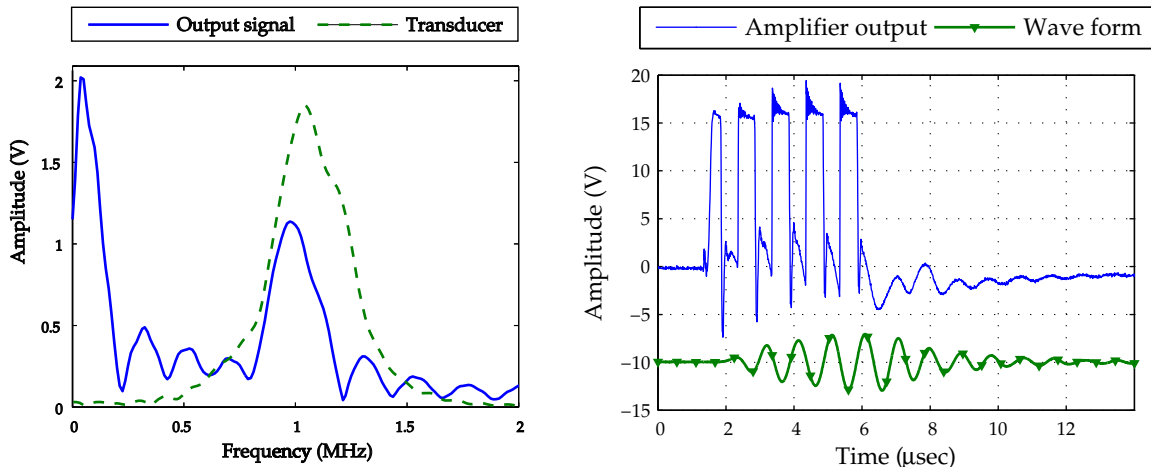


**Figure 2.11:** Electric input and output signals of the output amplifier circuit for a 5 cycle square wave burst input with transducer attached.

that the when the purely positive 0–5 V output of the hex inverter switches on, the DC content of the output signal causes the floating ground between  $C_1$  and  $C_2$  to be offset from 0 V for a short period of time. If the floating ground does not settle fast enough back to ground level, the square wave burst signal with 5 V amplitude is not able to switch on the n-channel MOSFET in the negative output side. A thorough analysis of the problem is still pending.

Notwithstanding the deficient performance of the amplification circuit in generating a symmetric output signal, the present output signal can still be used to generate a sufficiently clean wave form with the narrowband transducers, as the bandpass characteristics of the transducers filters out unwanted signal distortions as well as DC offsets, as explained in Section 2.6.1. Figure 2.12a shows the frequency content of the amplifier output signal, which is obtained from the FFT of this signal for positive frequencies, and compares it to the frequency response of the transducer. The transducer’s bandpass characteristic leads to generation of the wave form shown in Figure 2.12b from the output signal. The wave form is measured by a second transducer of the same type, which is



(a) FFT of the output signal and frequency response (normalized) of the transducer

(b) Time domain signal of amplifier output and resulting wave form. The wave is shifted by an offset of -10 V.

**Figure 2.12:** Comparison of the output amplifier signal with resulting wave form

clamped face-to-face to the generating transducer. Expansion of the transmitting transducer will lead to compression in the receiving transducer, which leads to a  $180^\circ$  phase shift between input and detected wave form. After the input and therefore also the output signal are switched off, the wave burst decays slowly, due to the low mechanical damping of the transducer face. As a piezo device, the transducer not only changes its shape in the presence of an electric field, but vice versa mechanical deformation also leads to changes in the voltage at its terminals. The voltage changes generated by the decaying mechanical oscillation show up in the measured output signal in Figure 2.12b after  $6 \mu\text{s}$ , the point in time when the input has been switched off.

The output stage is driven by the symmetric power supply shown in Figure 2.10b. The supply is built by stacking a sufficient number of batteries to reach  $\pm 18 \text{ V}$ . Any type of battery can be used, while 9 V block batteries are smaller compared to 1.5 V AA batteries, but provide less energy. Figure 2.3d on page 11 shows the stacked AA batteries that are used as power supply for the prototype circuit. As in every power supply, the capacitors  $C_5$  and  $C_6$  are used to stabilize the supply voltage.

The driver stage and the output booster stage are powered by separate power supplies.

In principle, they could all be run from the same  $\pm 18\text{ V}$  battery supply. However, this would either require a voltage divider circuit, which would dissipate limited energy in heat, or if only some of the stacked batteries would be used to also supply the driver stage, these would deplete faster than the other batteries. Thus, even though the separate battery for the driver stage requires additional space, it also prolongs the time during which the device can operate on the same set of batteries.

The MOSFETs are rated to handle voltages of up to  $60\text{ V}$ . Therefore, to avoid the problems that the prototype amplification circuit exhibits when switching from the positive to the negative supply rail, the output stage can instead also be driven by a purely positive  $0\text{--}36\text{ V}$  supply. This supply provides higher amplitudes in the output signal. However, the voltage offset of  $18\text{ V DC}$  leads to energy being dissipated by DC current passing through  $R_3$  to ground. When driven by a purely positive supply, only the p-channel MOSFET in the upper half of the output stage switches on and off. The lower half of the output stage is disabled.

## 2.7 *Analog-Digital Conversion*

Once the generated wave signal passes the test specimen, it is detected by a second transducer. This receiving transducer converts mechanical waves into electric signals. The weak analog signals are amplified and offset-corrected in a signal conditioning circuit. Details about this circuit will be provided in Section 2.7.2.

The output of the signal amplification circuit is then fed into the analog-digital converter (ADC) that is included in the *TMS320F28335* DSP. The ADC converts analog input signals in the range  $0\text{--}3\text{ V}$  with a 12 bit resolution to digital values in the range  $0\text{--}4095$  ( $= 2^{12} - 1$ ). Signals lower than or equal to  $0\text{ V}$  will be converted into the digital value  $0$ , signals equal to or above  $3\text{ V}$  will lead to the digital value  $4096$ . The ADC converter runs at a sampling rate of  $f_s = 8.3334\text{ MHz}$ , and saves the sampled digital values into one of its 16 result registers. These result registers can separately be addressed in memory, which is used for the DMA data transfer, explained in Chapter 2.7.3.

The ADC can sample up to 16 separate input channels. For the ultrasonic monitoring

device, only one input channel is used. Triggered by a start-of-conversion signal, which is generated by the PWM module as described in the last section, the ADC samples this channel continuously until the sampling sequencer is stopped. In the current prototype of the ultrasonic monitoring device, 4096 values are sampled during one measurement, which at the given sampling rate  $f_s = 8.3334$  MHz corresponds to  $491.5 \mu\text{s}$  sampling duration. With this sampling frequency, signal content of frequencies less than the Nyquist frequency  $f_N = f_s/2 = 4.1667$  MHz can be reconstructed without loss of information. The chosen sampling rate is thus sufficiently high for sampling the band-limited output of a transducer (cf. Figure 2.7b).

### 2.7.1 Delay Between Start of Output Signal and Start of Sampling

As the analog-digital conversion is triggered by the PWM module, whereby the micro-processor is bypassed, a reliably short delay between the start of the output signal and the start of the input sampling can be achieved. To determine this delay, the output of the pulse-width-modulation signal is sampled by the ADC circuit. To ensure that the measured results are not affected by signal delays in the output amplification or input signal conditioning circuit, these circuits are omitted; also no transducers are connected. The output of the PWM module is attenuated by a passive voltage divider, as the PWM high level output voltage of 3.3 V exceeds the maximum ADC input level of 3 V.

The sampling rate  $f_s = 8.3334$  MHz allows a time resolution of  $\Delta t = 1/f_s = 120$  ns. However, the position where the signal toggles might actually lie at any position in between two of these sampling points. Reading the apparent switching point from the time signal can therefore only give the time delay with an unsatisfactory precision. To increase the precision, the sampled data is plotted against square waves of much higher sampling rate, which have the same frequency and amplitude, and varying delays. Figure 2.13 illustrates this process for one measurement. Examining 10 measurements, the delays between the start of the output signal and the start of the sampling are found to be on the order of 120–140 ns, which is about one ADC sampling period. More importantly, the variation in the time delay is less than 25 ns, which is only one fifth of the sampling

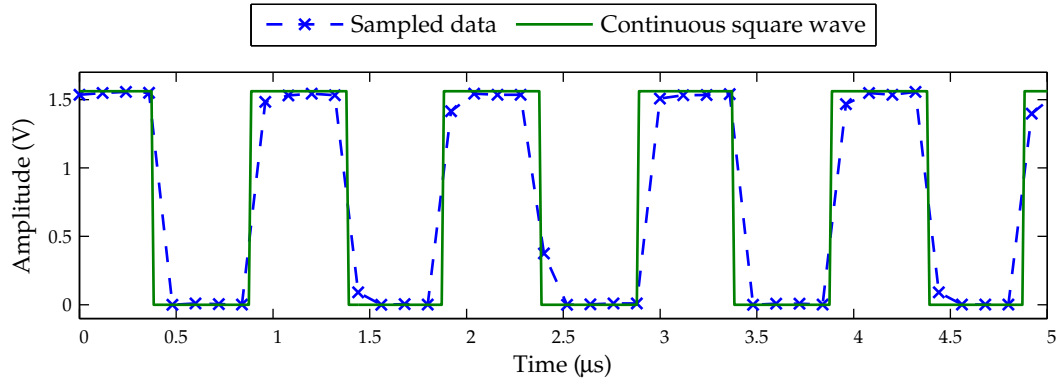


**Figure 2.13:** Sampled attenuated output signal and comparison with continuous square wave. The delay between start of output and start of sampling is about 120 ns.

period. Thus, the timing of the start of the sampling is very reliable. Furthermore, the waves that are generated by the transducers propagate through plexiglass wedges before they are converted to Rayleigh waves at the interface of the wedge with the specimen. Chapter 3.2 explains this process in detail. For now, just note that the propagation delay for waves inside the wedges is about  $23.3 \mu\text{s}$ . Compared to this propagation delay, the delay caused by the microprocessor is negligible.

The experimentally found time delay complies with the specifications of the microcontroller [39, Ch. 6.15]. The specifications say that a delay of 2.5 times the ADC clock period is to be expected from the start-of-conversion signal (SOC) until the sample-and-hold element starts acquiring data. The duration during which the sample-and-hold (S/H) element acquires data adds to the delay until the first sample is digitized. With the ADC clock running at a frequency of 25 MHz, and the S/H acquiring data for 2 ADC cycles, a delay of 4.5 cycles is expected until the first sample is digitized. This corresponds to a total delay of 180 ns. The fact that the actual delay is shorter than the specified delay indicates that the PWM module also shows a short delay between generating the SOC signal until the output signal switches to the high level for the first time.

## 2.7.2 Signal Conditioning Circuit

The ADC samples signals that are detected by the receiving transducer. These signals are relatively weak. For the excitation used in the ultrasonic device, the received signals

are on the order of 300–400 mV peak-to-peak for an undamaged specimen. These signals could directly be sampled by the analog-digital converter. However, in damaged specimens or over longer propagation distances, a signal’s amplitudes decrease. The ADC’s resolution of 12 bit over the input range of 0–3 V allows for voltages to be distinguished in the sampled signal, which are

$$\Delta V_{\text{ADC}} = \frac{3\text{ V}}{2^{12} - 1} = 0.733\text{ mV} \quad (2.8)$$

different. This quantization error impairs the quality of the sampled signal. To alleviate the influence of the quantization error and to improve the signal-to-noise ratio in the sampled signal, the analog signal is amplified so that it uses a large part of the input range of the analog-digital converter. The signal also has to be shifted to an offset of 1.5 V, as negative signal amplitudes could otherwise not be detected within the ADC’s strictly positive input range 0–3 V.

Besides the quantization error, aliasing effects also have to be considered. Following the Nyquist-Shannon sampling theorem, a signal can uniquely be reconstructed from a sampled sequence if its highest frequency content is lower than the so-called Nyquist frequency, which is half the sampling frequency [31, Ch. 4.2]. If a signal has a higher frequency content, i.e.

$$f_{\text{max}} \geq f_{\text{Nyquist}} = \frac{f_s}{2}, \quad (2.9)$$

this higher frequency content will show up as a phantom or aliased signal on lower frequencies. To prevent aliasing effects, an analog anti-aliasing low-pass filter is used.

These three functions, amplification, offset shift and low-pass filtering, are performed by the signal conditioning circuit. Figure 2.14 shows the power supply for this signal conditioning circuit, which driven by two 9 V batteries provides the symmetric supply voltage of  $\pm 9\text{ V}$  for the signal conditioning circuit. The capacitors  $C_1$  and  $C_2$  stabilize the power supply and filter noise ripples from the supply voltage, which would otherwise show up in the output of the signal conditioning circuit shown in Figure 2.15.

In the signal conditioning circuit, the incoming signal first passes two diodes, which clip the amplitude of the incoming voltage signals to the forward voltage drop of a diode,

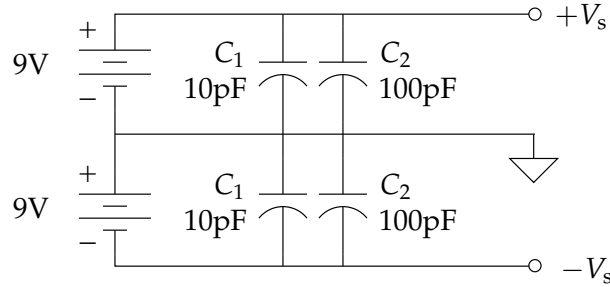


**Figure 2.14:** Power supply for signal conditioning circuit

which is about 0.6–0.7 V. Signals lower than the forward voltage drop are not affected. If, however, the amplitude of an incoming signal exceeds the forward voltage drop of a diode, this diode conducts current and shortens the input to ground. Thus, the maximum voltage that can enter the circuit equals one forward voltage drop. The diodes protect the rest of the circuit and the analog-digital converter from harmful peak surge voltages, which can for example occur when the piezo elements of the transducers are carelessly bumped against a hard surface. As these surge voltages may have either sign, two oppositely biased diodes are necessary to protect the circuit.

Next, the signal passes a high-pass filter consisting of the capacitor  $C_3$  and the resistor  $R_9$ . This filter blocks any low-frequency content in the signal coming from the transducer. If the input signal is not symmetric, its DC component charges the capacitor  $C_3$ , which blocks DC from entering into the amplification circuit. This charging would lead to distortions in the output. The resistor  $R_9$  provides a path to ground to avoid these distortions. The cutoff frequency  $f_{\text{cutoff,h}} = 1/2\pi R_9 C_3 = 159 \text{ Hz}$  of the high-pass filter is sufficiently high to block any low frequency distortions, but low enough so that it does not affect the high-frequency ultrasonic measurement signal.

The next stage of the circuit is a non-inverting amplifier (cf. [16, Ch. 3.05]) with variable gain and offset adjustment. The following analysis of the circuit assumes that the operational amplifier (op-amp) is ideal, which in particular means that it has infinite voltage gain, infinite input impedance and zero output impedance. With these assumptions the voltage at both the positive and negative input of the op-amp will always be equal; this voltage is denoted as  $v_{\text{in}}$ . Voltage at the output is denoted as  $v_{\text{out}}$ , and the voltage

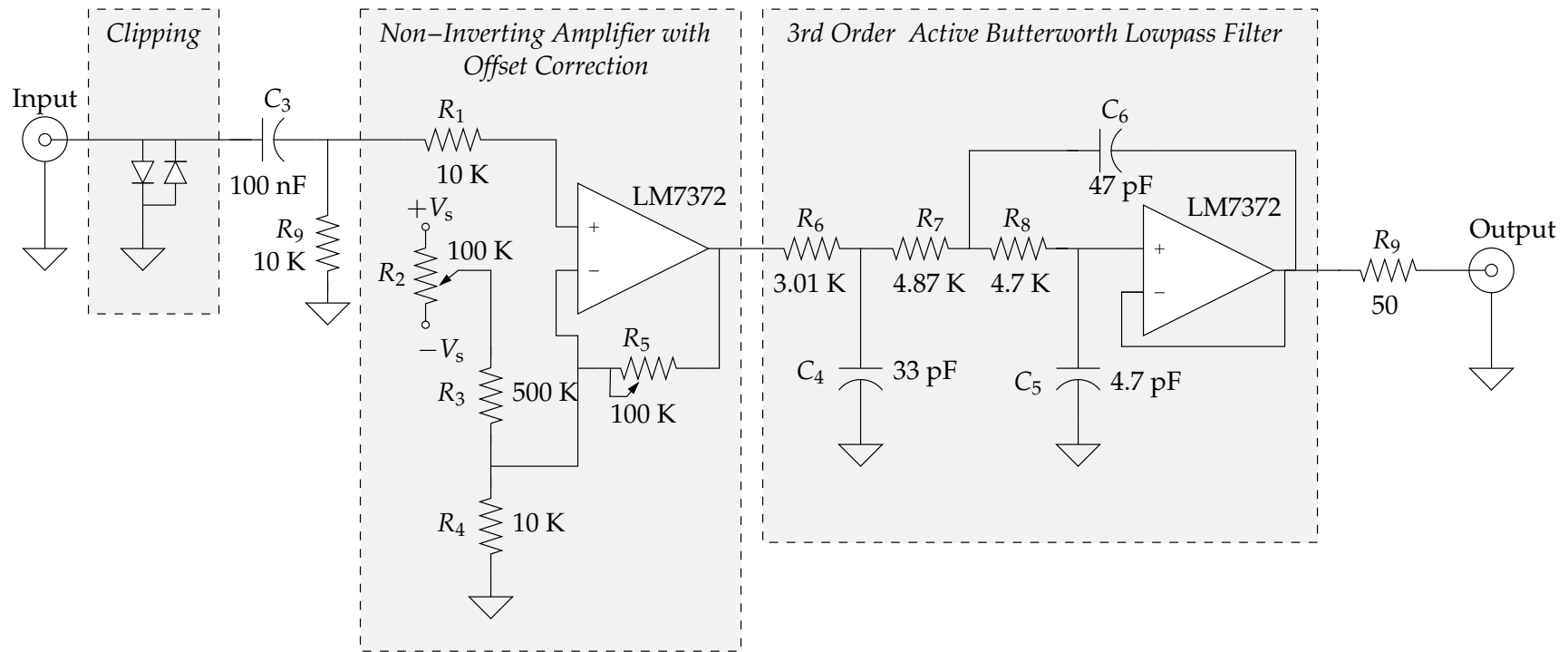


Figure 2.15: Signal conditioning circuit

at the wiper of  $R_2$  is denoted as  $V_{\text{wiper}}$ . The wiper is the adjustable connection point in between the two endpoints of a potentiometer. Let  $\alpha \in [0, 1]$  be the position of the wiper of  $R_2$ , where  $\alpha = 0$  corresponds to the position next to the negative supply rail for which  $V_{\text{wiper}} = -V_S$ , and  $\alpha = 1$  corresponds to the position at the positive supply rail, i.e.  $V_{\text{wiper}} = +V_S$ . Further,  $\beta \in [0, 1]$  denotes the wiper position of potentiometer  $R_5$ , where  $\beta = 0$  is the “right” end in the schematic, i.e. the potentiometer is shorted, and  $\beta = 1$  is the “left” end of the potentiometer, where the maximum possible resistance  $R_5 = 100 \text{ k}\Omega$  is connected across the op-amp feedback loop. Using Kirchhoff’s current law, the following relation between the output and the input can be obtained

$$v_{\text{out}} = \underbrace{-\frac{(2\alpha - 1)\beta R_5}{(1 - \alpha)\alpha R_2 + R_3} V}_{\text{Offset}} + \underbrace{\left[ \frac{\beta R_5}{(1 - \alpha)\alpha R_2 + R_3} + \frac{\beta R_5}{R_4} + 1 \right]}_{\text{Gain}} v_i. \quad (2.10)$$

The derivation of this expression is shown in Chapter A.1 in the appendix.

The resistor  $R_3$  is used to limit the current flow from the offset correction into the amplification circuit. Noting also that  $0 \leq (1 - \alpha)\alpha \leq 0.25$  for  $\alpha \in [0, 1]$ , the practical assumption

$$R_3 \gg (1 - \alpha)\alpha R_2 \quad (2.11)$$

can be made. Under this assumption, the output voltage can be approximated as

$$v_{\text{out}} = \underbrace{-\frac{\beta R_5}{R_3}(2\alpha - 1)V}_{\text{Offset}} + \underbrace{\left[ \beta R_5 \left( \frac{1}{R_3} + \frac{1}{R_4} \right) + 1 \right]}_{\text{Gain}} v_i. \quad (2.12)$$

Changing the amplification gain by changing  $\beta$  will also affect the output offset. So any change in the desired amplification gain also requires to adjust the offset by changing the position of the wiper of  $R_2$ . The amplification circuit can provide a maximum voltage gain of 11.2 or 20.98 dB, and a maximum offset of  $0.2V_S = 1.8 \text{ V}$ . The yet unmentioned resistor  $R_1$  owes its presence to the non-ideal behavior of a real op-amp. It increases the input impedance of the positive input and limits the current flow into the op-amp. For the signal conditioning circuit, a *National Semiconductor LM7372* op-amp is used, which offers a gain bandwidth product of 100 MHz and a slew rate of  $700 \text{ V}/\mu\text{s}$  when driven by  $\pm 5 \text{ V}$  [30]. With higher supply voltages, these values will further increase, so the *LM7372*

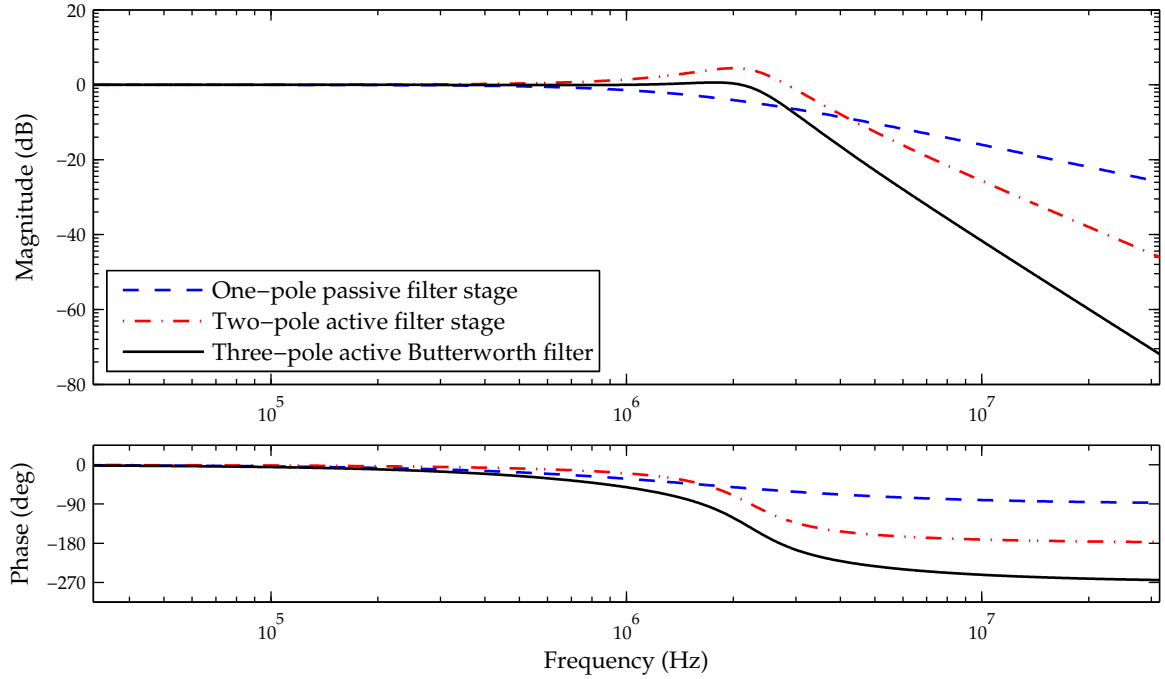


**Figure 2.16:** Frequency response of the low-pass filter

offers a sufficiently high gain and a sufficiently fast response for the desired 1 MHz, 1.5 V peak-to-peak sine wave output signal, whose maximum slope does not exceed  $10 \text{ V}/\mu\text{s}$ .

After passing the amplifier stage, the signal enters a 3<sup>rd</sup> order (also called 3-pole) active Butterworth low-pass filter with a cutoff frequency  $f_{\text{cutoff}} = 2.5 \text{ MHz}$ , which is well below the Nyquist frequency  $f_{\text{Nyquist}} = 4.1667 \text{ MHz}$ . Butterworth filters feature a maximum flat passband response, at the expense of steepness in the transition region from passband to stopband, and also the expense of a poor phase characteristic (cf. [16, Ch. 4.05]). As the ultrasonic device presented in this study is designed to detect the amplitude changes in ultrasonic signals, the advantage of a maximum flat passband response surpasses the aforementioned disadvantages of a Butterworth filter. To match the desired filter response, the use of capacitors and resistors with low tolerances is vital.

For the analysis of the filter behavior, the filter may be separated into a 1-pole low-pass consisting of  $R_6$  and  $C_4$ , which obeys the frequency response

$$G_{\text{filt},1}(j\omega) = \frac{1}{j\omega R_6 C_4 + 1}, \quad (2.13)$$

and a 2-pole active filter in Sallen-Key topology, which has the frequency response

$$G_{\text{filt},2}(j\omega) = \frac{1}{(j\omega)^2 R_7 R_8 C_5 C_6 + j\omega(R_7 + R_8)C_5 + 1}. \quad (2.14)$$

The derivation of these frequency responses is shown in Chapter A.2 in the appendix. The resulting frequency response of the 3-pole filter is given as the product of the two frequency responses,

$$G_{\text{filt}}(j\omega) = \frac{1}{(j\omega R_6 C_4 + 1) [(j\omega)^2 R_7 R_8 C_5 C_6 + j\omega(R_7 + R_8)C_5 + 1]}. \quad (2.15)$$

The frequency response of the two filters and of the resulting 3-pole filter are shown in Figure 2.16. As expected, the passband response is maximum flat, and as each filter pole contributes a magnitude drop of 20 dB per decade in the stopband, the magnitude in the stopband decreases with a total of 60 dB/decade. Using an active filter has advantages over a passive filter, as a good response for an active filter can be achieved without using inductances in the filter circuit. The active filter also acts as buffer stage, decoupling the filter input and output, and decreasing the output impedance. The *LM7372* is a dual op-amp, i.e. it contains two op-amps in one physical package. One op-amp is used for the amplification and offset correction circuit, so the second one can be used for the active filter without the need for an additional, separate op-amp package for the active filter.

An ideal op-amp has an output impedance of zero; the *LM7372* has a very low open loop output resistance of  $15 \Omega$ , which is further decreased by the negative feedback [16], so that the actual output impedance virtually reaches the ideal zero output impedance. However, the impedance mismatch between the zero output impedance of the filter circuit output and the  $50 \Omega$  impedance of coaxial cables, which are used to connect the amplification circuit to the microcontroller board, would cause energy to be reflected back and forth. These energy reflections would lead to standing waves in the circuit. As the standing waves are generated after the signal already has passed the low-pass filter, this filter can't attenuate them, so that these signals would show up in the sampled analog-digital converted signals – either directly or in form of aliased signals. To avoid standing waves, the resistor  $R_9$  increases the output impedance of the signal conditioning circuit to  $50 \Omega$  to match the impedance of the coaxial connectors and cables.

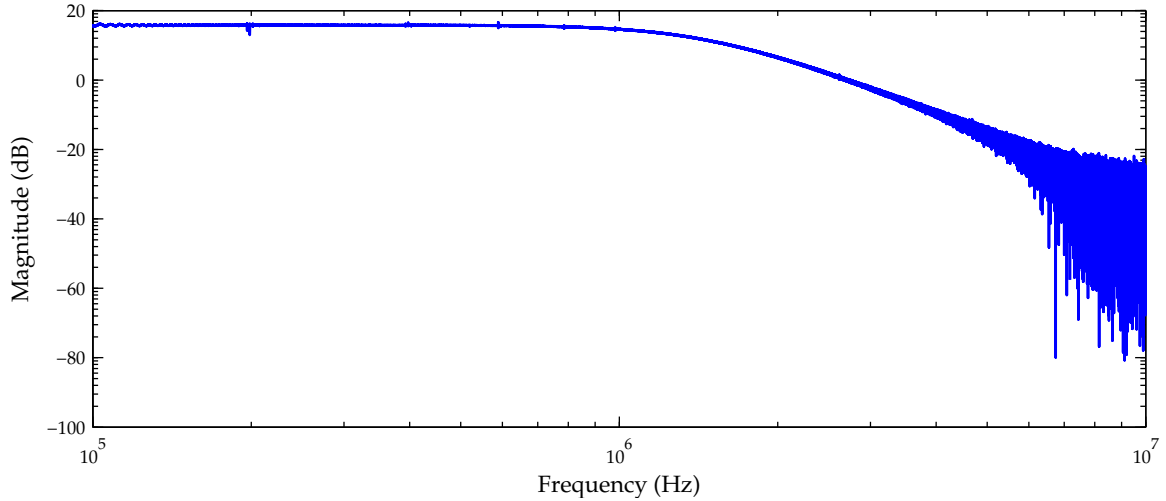


**Figure 2.17:** Measured amplitude of the frequency response of the amplifier circuit, obtained using a sine sweep signal, and amplitude corrected to account for the amplitude distortion of a sweep signal.

Figure 2.17 shows the measured frequency response of the amplification circuit. This frequency response has been obtained by applying a sine sweep signal at the input and calculating the DFT of the recorded output. Clearly visible is the desired flat passband response, and decay after the cutoff frequency. The distortions in the frequency response above 5 MHz are attributed to imperfections and deviations of the parts used for the filter from their nominal values. Figure 2.18 shows the output of the amplification circuit when an offset-free sinusoidal signal with 300 mV amplitude and 1 MHz frequency is fed into the circuit's input. The output is amplified by nearly 14 dB and offset corrected. The phase of the output signal is about  $76.3^\circ$  delayed to the phase of the input. The nominal Butterworth filter delays the phase of a 1 MHz signal by  $51.4^\circ$  (cf. Figure 2.16). The non-ideal operational amplifier adds some additional phase delay, and tolerances of the parts used lead to deviations of the actual filter response from the nominal one. The amplitude of the Butterworth filter is highly desirable when examining the amplitudes of signals, other filter designs like the Bessel filter offer better performance when a good phase behavior is important (cf. [16, Ch. 4.05]).

To assess the influence of noise in the signal conditioning circuit on the output of the ADC, a constant voltage of 150 mV generated by an *Agilent 33250A* function generator

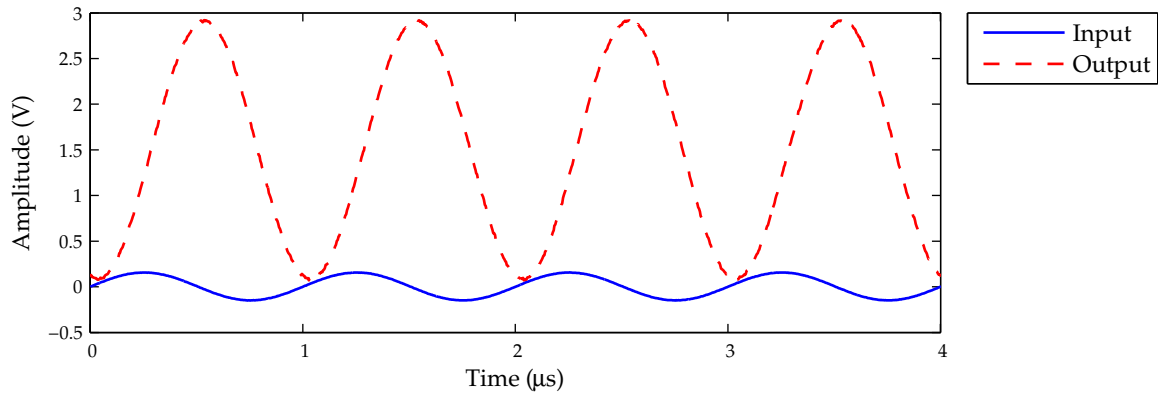
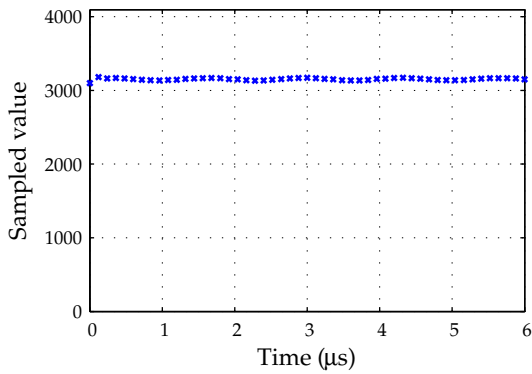


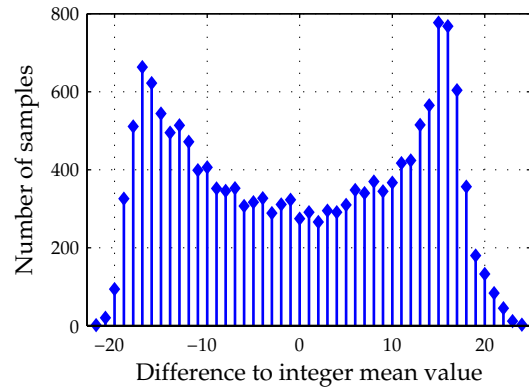
**Figure 2.18:** Input and output of the amplification circuit for a sinusoidal input of 1 MHz.

is applied to the input of the signal conditioning circuit. The noise on the output of the signal generator is about 2.6 mV peak-to-peak. Four measurements of 4096 samples each are taken. Figure 2.19a shows the resulting ADC converted signal for one of the measurements. The constant value is superimposed by a nearly purely harmonic oscillation in the ADC sampled signals, which suggests that the main part of the distortions in the output signal originates either from reflected energy due to a remaining slight impedance mismatch in the connection from the signal generator through the signal conditioning circuit to the ADC, or from electro-magnetic interference. The values of the first two samples in each measurement are distinctly different from the remaining values. This larger difference to the mean value of the signal when sampling a constant input is attributed to the start-up process of the ADC converter and does not reflect the noise that affects the output during the sampling of AC signals. Therefore, the first two samples of each measurement are discarded for the further analysis; for the remaining samples, the difference of their values to the mean value, which has been rounded to the nearest integer, is calculated. Figure 2.19b shows the resulting distribution of differences.

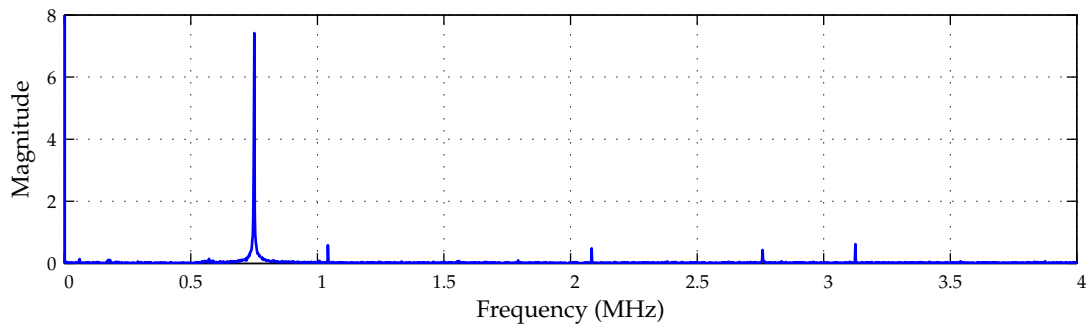
The differences span a total range of 46 integer values, which equals 5.52 bits. These disturbances therefore affect the lowest 6 bits of the sampled signal, and reduce the output resolution of the ADC to 6.48 bits if the actual output values are directly considered. However, the frequency content of the sampled signal, plotted in Figure 2.19c, shows that



(a) Time domain signal, the ordinate scale corresponds to the full output range of the ADC



(b) Histogram of the difference of the sampled values from the integer mean value



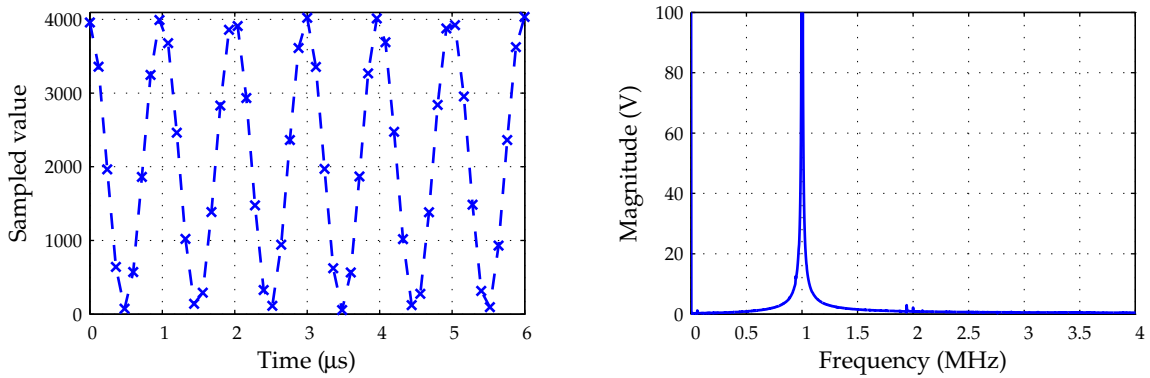
(c) FFT magnitude of the sampled signal, the DC component has been clipped in the plot

**Figure 2.19:** Influence of noise and signal distortions in the signal conditioning circuit to the ADC output for a constant input of 150 mV to the signal conditioning circuit

the main distortion is at a single frequency of 750 kHz. A digital notch filter can thus be used to eliminate the influence of the distortion on the sampled output signal.

Despite the distortions found for DC signals, the circuit shows a better performance when AC signals are sampled; the distortions in the output signal are significantly alleviated. Figure 2.20a shows the sampled signal when a 1 MHz input signal of 300 mV amplitude is applied to the signal conditioning circuit. The frequency spectrum, Figure 2.20b has a dominant peak at the signal frequency; distortions at other frequencies are negligible compared to this frequency content. A typical ultrasonic signal consists of short, band-limited wave bursts, which are AC signals, and only noise in between. Therefore, the signal distortions for DC input signals are only of minor interest, but they have to be considered when distinguishing signals from noise.

The considerations about the noise content in the sampled signal suggest to use frequency-based data analysis methods. These are also less prone to the effects of sampling distortions. Section 2.8 provides more details about the proposed data analysis methods, and Chapter 4.3 illustrates the effects of sampling on the data analysis of measured data.



(a) Time domain signal, the ordinate scale corresponds to the full output range of the ADC

(b) FFT magnitude of the sampled signal

**Figure 2.20:** Influence of noise and signal distortions in the signal conditioning circuit to the ADC output for a 1 MHz sinusoidal input to the signal conditioning circuit with 300 mV amplitude

### 2.7.3 Sampling Registers and DMA Data Transfer

During measurements, the analog digital converter (ADC) samples data continuously with a sampling rate of 8.3334 MHz. Each 120 ns a new value has to be stored into one of the 16 ADC result registers. These 16 result registers are used as cyclic buffer. After a result has been written to the 16<sup>th</sup> result register, the next one will be written to the first result register, overwriting the value already stored in it. Therefore, the data has to be continuously copied from the result registers to the external SRAM, where the sampling results are saved.

To avoid swamping the microcontroller with the data transfer, the direct memory access (DMA) controller included in the *TMS320F28335* DSP is used to transfer the sampled data to the external SRAM. DMA data transfers directly copy data from the source memory location to the destination, bypassing the CPU. If data is transferred without a DMA controller, the CPU has to read each value from memory and write it to the desired destination. This transfer might be interrupted by an interrupt handler routine, so that the data transfer can not be guaranteed to finish in time. With a DMA controller, the CPU is free to handle other tasks while the data transfer is running; as long as no concurrent accesses to the same memory location occur, which would stall one of the memory accesses, both tasks execute independently.

The principle of the data transfer from the ADC result registers to external SARAM is shown in Figure 2.21. After eight data points have been sampled into the registers 1–8, the ADC signals the DMA controller to start the first transfer. The DMA controller then copies the values stored in the registers 1–8 to the next free memory location in the external SRAM, sorting the data from the cyclic buffer into a sequence. Meanwhile, the ADC continues sampling data to the result registers 9–16. When a sampling value has been written to result register 16, the ADC signals the DMA controller to start transferring the next eight data points from registers 9–16. As the result registers are used as cyclic buffer, after writing to register 16, the ADC again continues to sequentially store sampled values to the registers 1–8. This process is repeated until 4096 samples (i.e. 512 transfers of

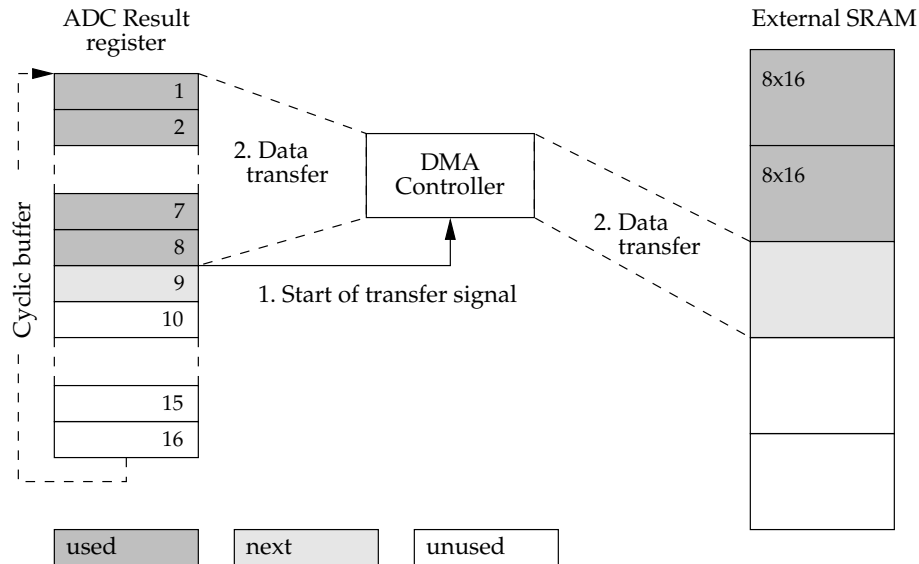


**Figure 2.21:** Data transfer using the DMA controller

8 samples each) have been transferred. Thereafter, the ADC will still continue to sample data to its result registers, but the DMA controller no longer transfers data. Rather, the DMA controller sends an interrupt to the CPU to signal that the desired number of samples has been transferred. The interrupt handler routine then stops the ADC. As the DMA controller stops transferring data, switching off the ADC is no longer time critical, as all data that might be overwritten by new samples is already stored at another location.

The DMA controller transfers the data to a temporary storage location in the external memory. Afterwards, the data has to be copied to the desired final storage location, which is done by the CPU. Instead of only copying the data, the CPU can also combine the data with previously acquired data, which offers the possibility to average multiple measurements in order to reduce noise in the signal.

## 2.8 Signal Processing and Data Compression

The TMS320F28335 DSP can be used very efficiently to process sampled data on-board. This DSP includes an IEEE-754 Single-Precision (32 bit) floating point unit (FPU). Floating point operations are beneficial for calculations compared to fixed point operations, as

signals don't need to be scaled for the computation. The IEEE-754 single precision format separates numbers into fractional part and exponent. The fractional part is stored with 24 bit precision, which corresponds to slightly more than 7 decimal digits ( $\log_{10} 2^{24} \approx 7.2$ ).

Processing data on-board significantly reduces the amount of data that has to be transmitted. In the prototype, a fast Fourier transform (FFT) algorithm is implemented, which can be used to analyze signals in the frequency domain. The FFT is also used to obtain the Hilbert transform of a signal. The Hilbert transform is an integral transform that can be used to calculate the envelope curve of a signal, which is useful to extract wave bursts from measured ultrasonic data. These two steps, calculation of the Hilbert transform and extracting wave bursts, will be presented in Section 2.8.2. The envelope signal may also later be used for the autonomous evaluation of measured ultrasonic signals to assess material damage.

### 2.8.1 Fourier Transform and Fast Fourier Transform

The discrete Fourier transform (DFT) is a transform, which for a given time-discrete finite sequence yields a corresponding frequency representation of the signal. Most commonly, the DFT of a sequence  $x[n]$  of length  $N$ , where  $n = 0 \dots N - 1$ , is defined as [31]

$$X[k] = \sum_{n=0}^{N-1} x[n] W_N^{kn}, \quad k = 0 \dots N - 1, \quad (2.16)$$

where  $W_N = e^{\frac{-2\pi j}{N}}$ . The inverse transform is defined as

$$x[n] = \frac{1}{N} \sum_{k=0}^{N-1} X[k] W_N^{-kn}, \quad n = 0 \dots N - 1. \quad (2.17)$$

The DFT is identical to samples of the Fourier transform at equally spaced frequencies, each  $\Delta f = f_s/N$  apart. Aside from the factor  $1/N$  and the sign of the exponent of  $W_N^{\pm kn}$ , the discrete Fourier transform and its inverse are identical, so as far as computational methods are considered, they can be treated equally.

Direct computation of one value of the DFT as given by Equation (2.16) would require  $N$  complex multiplications and  $N - 1$  complex additions. For the entire sequence,  $N^2$  complex multiplications and  $N(N - 1)$  complex additions are required, where each complex multiplication requires four real multiplications and two real additions, and each

complex addition requires two real additions [31, Ch. 9.1]. Thus, the direct computation of the DFT requires  $\mathcal{O}(N^2)$  operations.

However, using an FFT algorithm, the computational effort can be reduced to order  $\mathcal{O}(N \log_2 N)$ . One possible FFT algorithm is the so-called decimation-in-time algorithm. For the algorithm, it is assumed that the number of samples  $N$  is an integer power of 2, i.e.  $N = 2^\nu$ ,  $\nu \in \mathbb{N}$ . Then, the sum in Equation (2.16) can be split into the even and odd numbered samples,

$$X[k] = \sum_{r=0}^{N/2-1} x[2r] W_N^{2kr} + \sum_{r=0}^{N/2-1} x[2r+1] W_N^{k(2r+1)}. \quad (2.18)$$

As  $W_N^2 = e^{\frac{-2\pi j}{N/2}} = W_{N/2}$ , the last equation may also be written as

$$\begin{aligned} X[k] &= \sum_{r=0}^{N/2-1} x[2r] W_{N/2}^{kr} + W_N^k \sum_{r=0}^{N/2-1} x[2r+1] W_{N/2}^{kr} \\ &= G[k] + W_N^k H[k], \quad k = 0 \dots N-1 \end{aligned} \quad (2.19)$$

Each of the sums in the last equation is a  $N/2$ -point DFT:  $G[k]$  the DFT of the even samples and  $H[k]$  the DFT of the odd samples. Each of the  $N/2$ -point DFTs can again be split up into two  $N/4$ -point DFTs, each of which again can be split up into two  $N/4$ -point DFTs, and so forth, down to 1-point DFTs, whose results are identical to the original values. The results of these sub-transformations must be combined as defined by Equation (2.19). Figure 2.22 shows the computation scheme for an 8-point decimation-in-time FFT. Notably, only in the very last stage of the computation scheme uneven powers of  $W_N$  appear, in the stages before only even powers are used. This is due to the fact, that in the second to last stage DFTs of  $N/2$ -point sequences are computed for which powers of  $W_{N/2}$  are used, which are equivalent to powers of  $W_N^2$ . Similarly, in the third from last stage, powers of  $W_{N/4} = W_N^4$  are used.

In the first stage of a decimation-in-time algorithm, the  $N$ -point DFT is split into the  $N/2$ -point DFT of the even samples, and the  $N/2$ -point DFT of the odd samples. For this, the samples are reordered, so that first all even and then all odd samples are in sequence. Now consider only the even numbered samples, which can again be numbered from 0 to  $N/2 - 1$ . For the second stage of the FFT algorithm, the “even” numbered even samples

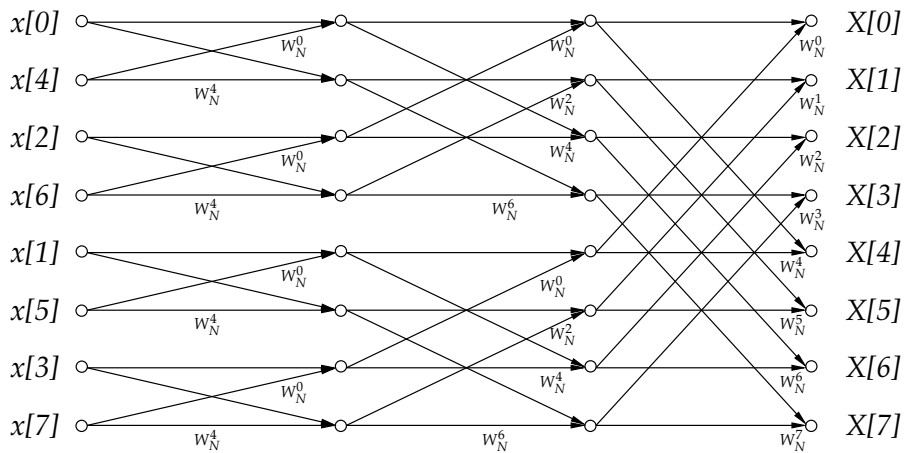


**Figure 2.22:** Computation scheme for an 8-point decimation-in-time in-place FFT, cf. [31, Fig. 9.7]. Circles are summation points. If an arrow has a variable next to it, the value at its start must be multiplied with variable before being added .

are separated from the “odd” numbered ones. In terms of the original numbering of the samples, the indices of the “even” numbered even samples are multiples of four, and the “odd” numbered even samples have original indices which are given as  $2(2l + 1)$ ,  $l \in \mathbb{N}$ . While the final sequence is elaborate to describe in radix-10 math, it is simply the bit reverse of the original indices in binary math. Sorting a sequence of binary numbers by the last (least significant, LSB) bit separates even (LSB is 0) from odd (LSB is 1) numbers. In the next step, the same sorting can be done with the second to last bit separately for the even and the odd numbers, which will separate the “even even” from the “even odd” numbers, and the “odd even” from the “odd odd” numbers. So by bit-reversing the indices, they will appear in the right order, as for an ascending order of binary numbers first the most significant bit (MSB) is considered, then the second and so forth.

The computation scheme for the FFT displayed in Figure 2.22 allows for in-place computations. In calculations in each stage, two numbers are combined and saved at the same memory locations again. Only temporary storage is required to hold these two values, but no additional memory for the samples. An implementation of the decimation-in-time FFT algorithm is given in [33, Ch. 12.2]. This FFT algorithm uses the bit reversal algorithm by Gold and Rader [12], which does not require a table to store the bit-reversed sequences. This is beneficial, as memory is precious on a microprocessor. Gold and Rader’s algorithm

reverses a sequence by running a loop  $N - 1$  times. Karp [18] compares the performance of different bit reversal algorithms, including Yong's heuristic algorithm [53], which is similar to the algorithm presented by Gold and Rader, but reduces the loop count to  $N/4$ . Therefore, Yong's algorithm is adapted to handle complex numbers, which are stored as real part followed by imaginary part in the next memory location, and the algorithm is implemented on the microprocessor. The bit reversal algorithm is given in Figure B.1 in the appendix.

Each FFT algorithm needs powers of the complex exponential  $W_k$ ,  $k = 1 \dots N$  for the different stages of the FFT algorithm. In the algorithm presented by Press et al., standard C sine and cosine functions are used. To save computation time and to be independent from the availability of an implementation of a sine and cosine function on the microprocessor, the needed base values  $W_k$  are saved in an array, from which the appropriate values are read by the algorithm. Pseudo code for the main part of the FFT algorithm is shown in Figure B.2 in the appendix.

So far, the DFT of a complex sequence has been considered. For a purely real sequence, the DFT at negative frequency values is the complex conjugate of the transform at the corresponding positive frequency values. Thus, the DFT of a  $N$ -point real sequence can completely be described by  $N/2 + 1$  complex values, instead of  $N$  complex values as necessary for a  $N$ -point complex sequence. Also, the first element corresponding to the frequency zero, and the element corresponding to the Nyquist frequency are purely real [33, Ch. 12.3]. By storing the value at the Nyquist frequency as the imaginary part of the DC value, the complex DFT of a real-valued sequence can be stored in the same memory locations as the original sequence.

For calculating the DFT of a purely real input sequence  $x[n]$ , the sequence can be split into two sequences: one containing the even and one containing the odd numbered samples. The even numbered samples are considered to be the real parts and the odd numbered samples to be the imaginary parts of the  $N/2$ -length complex sequence  $y[n]$ . The DFT of the resulting sequence  $y[n] = x[2n] + jx[2n + 1]$ ,  $n = 0 \dots N/2 - 1$  is given as the complex sequence  $Y[k] = X^e[k] + jX^o[k]$ ,  $k = 0 \dots N/2 - 1$ , with  $X^e[k]$  the DFT of the even

samples, and  $X^o[k]$  the DFT of the odd samples, both of which are complex sequences. For the DFT  $F[k]$  of the purely real sequence  $f[n]$  of length  $N$ , it holds  $F[N - k] = (F[k])^*$ , where the asterisk denotes complex conjugation. This is the DFT's equivalent to the complex conjugate symmetry of a continuous time Fourier transform of a real function  $f(t)$ , for which  $\mathcal{F}\{f(t)\}|_{-\omega} = (\mathcal{F}\{f(t)\}|_{+\omega})^*$ . Thus, as  $x[2n]$  and  $x[2n + 1]$  are both purely real  $N/2$ -length sequences, it holds  $X^e[N/2 - n] = (X^e[n])^*$  and  $X^o[N/2 - n] = (X^o[n])^*$ . Using these two identities, it is found that  $(Y[N/2 - k])^* = X^e[k] - jX^o[k]$ . Thus,

$$X^e[k] = \frac{1}{2} (Y[k] + (Y[N/2 - k])^*) \quad (2.20a)$$

$$X^o[k] = \frac{1}{2j} (Y[k] - (Y[N/2 - k])^*) = -\frac{j}{2} (Y[k] - (Y[N/2 - k])^*). \quad (2.20b)$$

Equation (2.19) shows how the DFTs of the subsequences are combined to obtain the DFT of the original sequence. Using this equation in conjunction with the last two equations finally makes it possible to recover the DFT of the original real sequence from the result of the complex FFT,

$$X[k] = \frac{1}{2} (Y[k] + (Y[N/2 - k])^*) - \frac{j}{2} (Y[k] - (Y[N/2 - k])^*) W_N^k, \quad k = 0 \dots \frac{N}{2} - 1. \quad (2.21)$$

The element at  $N/4$  should be treated separately to save unnecessary calculations. As  $W_N^{\pm N/4} = \pm j$ , it follows

$$X[N/4] = \text{Re } Y[N/4] \pm j \text{Im}(Y[N/4]). \quad (2.22)$$

Thus, only the sign of the imaginary part has to be adjusted depending on whether the FFT is defined with the positive or negative exponent of  $W_N$ . Also, the complex FFT does not yield the element  $Y[N/2]$ . But, as  $W_{N/2}^{N/2} = W_{N/2}^0 = 1$ , from Equation (2.19) it follows that  $Y[N/2] = Y[0]$ . Therefore, Equation (2.21) yields  $X[0] = \text{Re } Y[0] + \text{Im } Y[0]$  and  $X[N/2] = \text{Re } Y[0] - \text{Im } Y[0]$ .

The decimation-in-time algorithm presented before assumes that complex numbers are saved with their real parts followed by their imaginary parts in the next memory location. Therefore, the purely real  $N$ -element sequence needs not to be reordered before the complex  $N/2$ -length FFT algorithm is called.

## 2.8.2 Envelope Detection with the Hilbert transform

The Fourier transform can be used for a convenient calculation of the Hilbert transform, another integral transform commonly used in signal theory. One particular application of the Hilbert transform, for example, is the modulation and the demodulation of signals for transmission. Given a real-valued signal in time, the Hilbert transform serves as basis to find the corresponding complex “analytic signal.” The term “analytic” refers to the definition of analytic functions in the sense of complex algebra. The notion of an analytic signal can be seen as a generalization of Euler’s formula  $\exp(jz) = \cos z + j\sin z$ . Hahn [14] provides a thorough study of the properties and applications of the Hilbert transform. Within the study at hand, the Hilbert transform is used to detect the envelope curve of a modulated signal; only the main properties necessary to understand that process will be presented, following Hahn’s presentation of the material.

For a given function  $u(t)$ , the Hilbert transform yields the transformed function  $\mathcal{H}\{u(t)\} = v(t)$ , for which the complex function  $\psi(t) = u(t) + jv(t)$  is analytic. Other than the Fourier transformation, which maps a function in time onto a function in the frequency domain, the Hilbert transform maps a function in one domain onto another function in the same domain, i.e. the Hilbert transform for a function of time will also be a function of time. The Hilbert transform is defined by the integral

$$v(t) = \mathcal{H}\{u(t)\} = -\frac{1}{\pi} \text{CPV} \int_{-\infty}^{\infty} \frac{u(\eta)}{\eta - t} d\eta \quad (2.23)$$

where CPV is the Cauchy principal value of the improper integral, i.e.

$$v(t) = -\frac{1}{\pi} \lim_{\substack{\varepsilon \rightarrow 0 \\ A \rightarrow \infty}} \left\{ \int_{-A}^{t-\varepsilon} (\cdot) d\eta + \int_{t+\varepsilon}^A (\cdot) d\eta \right\}. \quad (2.24)$$

Note that two functions, which constitute a Hilbert pair, are orthogonal, i.e.

$$\int_{-\infty}^{\infty} u(t)v(t) dt = 0. \quad (2.25)$$

The Hilbert transform may also be written as the convolution  $v(t) = 1/\pi t * u(t)$ . The convolution notation is helpful for determining the spectrum of an analytic signal  $\psi(t) = u(t) + j\mathcal{H}\{u(t)\}$ , which is given by the Fourier transformation  $\mathcal{F}\{\psi(t)\}$ . The convolution of two functions in the time domain is equivalent to the multiplication of these

in the frequency domain. The Fourier transform of the kernel of the Hilbert transform is given as

$$\mathcal{F} \left\{ \frac{1}{\pi t} \right\} = -j \operatorname{sgn}(\omega), \quad (2.26)$$

with the signum function defined as

$$\operatorname{sgn}(f) = \begin{cases} 1 & \text{for } f > 0 \\ 0 & \text{for } f = 0 \\ -1 & \text{for } f < 0. \end{cases} \quad (2.27)$$

As the Fourier transform is a linear transformation, the spectrum of the analytic signal  $\psi(t)$  is given as

$$\Psi(\omega) = \mathcal{F}\{\psi(t)\} = \mathcal{F}\{u(t)\} + j\mathcal{F} \left\{ \frac{1}{\pi t} \right\} \mathcal{F}\{u(t)\} = U(\omega)(1 + \operatorname{sgn}(\omega)). \quad (2.28)$$

From the last equation it can be seen, that the spectrum  $\Psi(\omega)$  of an analytic signal is zero for negative frequencies, equal to  $U(0)$  at  $\omega = 0$ , and  $\Psi(\omega) = 2U(\omega)$  for  $\omega > 0$ . With this knowledge, instead of directly evaluating the integral given in Equation (2.23), the Hilbert transform can be calculated using the Fourier transform of a signal, “correcting” the spectrum as given by Equation (2.28), and taking the inverse Fourier transform. This process will yield the analytic signal. The original function is the real part of the obtained analytic function, and the Hilbert transform is the imaginary part.

As mentioned in the introduction to this section, the Hilbert transform can be seen as a generalization of Euler’s formula  $e^{j\omega t} = \cos(\omega t) + j \sin(\omega t)$  (here written for real-valued functions). Thus, the Hilbert transform of  $\cos(\omega t)$  is  $\sin(\omega t)$ . As  $\cos^2(\omega t) + \sin^2(\omega t) = 1$ , this transform pair together with Bedrosian’s theorem can be used to find the envelope curve of a modulated signal:

**Theorem 1 (Bedrosian’s theorem [5])** *Let  $f(x)$  and  $g(x)$  denote generally complex functions in  $L^2(-\infty, \infty)$  of the real variable  $x$ . If*

1. *the Fourier transform  $F(u)$  of  $f(x)$  vanishes for  $|u| > a$  and the Fourier transform  $G(u)$  of  $g(x)$  vanishes for  $|u| < a$ , where  $a$  is an arbitrary positive constant, or*
2.  *$f(x)$  and  $g(x)$  are analytic (i.e., their real and imaginary parts are Hilbert pairs),*

then the Hilbert transform of the product of  $f(x)$  and  $g(x)$  is given by

$$\mathcal{H}\{f(x)g(x)\} = f(x)\mathcal{H}\{g(x)\}. \quad (2.29)$$

In other words, if the two functions have separate spectra, only the Hilbert transform for the function with the higher frequency content has to be determined to obtain the Hilbert transform of their product. Next, consider an amplitude modulated signal with carrier frequency  $\omega_0$  and amplitude  $e(t) \geq 0$ ,

$$s(t) = e(t) \cos(\omega_0 t + \varphi). \quad (2.30)$$

The frequency of the carrier function commonly is much higher than the frequency content of the modulating envelope signal. For the ultrasonic testing examined in this work, the carrier frequency is 1 MHz. If the envelope signal is band limited, i.e. it has no frequency content of or above 1 MHz, the corresponding analytic signal is obtained by applying Bedrosian's theorem:

$$s_{\text{analytic}}(t) = e(t) [\cos(\omega_0 t + \varphi) + j \sin(\omega_0 t + \varphi)]. \quad (2.31)$$

Taking the absolute value of the analytic signal finally yields the envelope signal:

$$|s_{\text{analytic}}(t)| = |e(t)| \underbrace{|\cos(\omega_0 t + \varphi) + j \sin(\omega_0 t + \varphi)|}_{=1} = e(t). \quad (2.32)$$

In practice, the requirement of a band limited spectrum for the envelope signal does not limit the application of the envelope detection for the ultrasonic signals considered in this work. Figure 2.7b on page 23 shows that the transducer acts as bandpass filter. The highest frequency for a modulating signal, that can be picked up by the transducer, is given as the maximum distance from the carrier signal; for a 1 MHz signal, the highest possible modulation signal is on the order of 800 kHz. Signals, which might violate the assumptions of Bedrosian's theorem would show up close to 0 Hz and  $2\omega_0$ . Signals at these frequencies are sufficiently attenuated by the transducer. Thus, the assumptions of the theorem are met.

Even though the receiving transducer does not allow DC signals to pass, the sampled signals contain a DC offset, which is introduced by the signal conditioning circuit, as it

centers the signals in the purely positive input range of the ADC. Therefore consider an amplitude modulated signal with an offset, which can be described as

$$s(t) = S_0 + e(t) \cos(\omega_0 t + \varphi). \quad (2.33)$$

As the Hilbert transform is linear, the two terms of the sum may be transformed separately. A constant signal only has frequency content at  $\omega = 0$ , and as the spectrum of the associated analytic signal must be zero for negative frequencies, it directly follows that the Hilbert transform of a constant can only be zero. Thus, the corresponding analytic signal is given as

$$s_{\text{analytic}}(t) = S_0 + e(t) [\cos(\omega_0 t + \varphi) + j \sin(\omega_0 t + \varphi)]. \quad (2.34)$$

To obtain the envelope curve, the offset  $S_0$  first has to be subtracted from the signal, then  $e(t)$  can be obtained as the absolute value of the offset-free signal as described before, and finally the offset is added again.

### 2.8.3 Calculation of the Discrete-Time Hilbert Transform

So far, only continuous time functions have been considered. However, the microprocessor works with a sequence of samples instead of a continuous function. Discrete time sequences inherently can not be “analytic,” as they are only functions of integers and not of a continuous variable. However, an “analytic-like” sequence can be defined, whose DFT has no negative frequency content. Marple [23] summarizes two common approaches: Oppenheim and Schaffer [31, Ch. 11.4.1] suggest to use dual quadrature FIR filters to approximate the real and imaginary part of an analytic-like sequence  $z[n] = z_r[n] + jz_i[n]$ , that belongs to a sequence  $u[n]$ . This approach fulfills the finite-length orthogonality condition

$$T \sum_{n=0}^{N-1} z_r[n] z_i[n] = 0, \quad (2.35)$$

but does not preserve the real part signal, i.e.  $z_r[n] \neq u[n]$ . Another approach is suggested by Reilly et al. [35], who apply a single FIR filter to generate  $z_i[n]$ .  $z_r[n]$  is simply taken identical to the original sequence. This method obviously preserves the real part,

but the orthogonality condition (2.35) is not satisfied. Marple proposes to calculate the analytic signal based on the DFT of the original sequence, using the knowledge about the spectrum of the analytic signal given by Equation (2.28). For the  $N$ -point DFT  $X[k]$  of a sequence  $x[n]$  as defined by Equation (2.16), the values  $X[k]$ ,  $k = 0 \dots N/2$  correspond to positive frequencies,  $X[N/2]$  is the frequency content at the Nyquist frequency  $f_{\text{Nyquist}}$ , and  $X[k]$  for  $k = N/2 + 1 \dots N - 1$  corresponds to negative frequencies. Thus, the spectrum  $Z[k]$  of the analytic sequence  $z[n]$ , that corresponds to  $x[n]$ , is given by

$$Z[k] = \begin{cases} X[0] & \text{for } k = 0 \\ 2X[k] & \text{for } 1 \leq k < \frac{N}{2} \\ X[\frac{N}{2}] & \text{for } k = \frac{N}{2} \\ 0 & \text{for } \frac{N}{2} < k \leq N - 1. \end{cases} \quad (2.36)$$

Note that even though the Nyquist frequency is positive, the appropriate value is not multiplied by 2. This is necessary to fulfill the orthogonality condition and to preserve the original real data sequence. An intuitive justification, stated by Marple, is that  $X[N/2]$  and  $X[0]$  are both shared boundaries between the positive and negative frequency halves of the periodic spectrum, and therefore these terms have to be split when dividing the spectrum into positive and negative halves. A formal justification can be found in [23, Sec. IV].

To calculate the analytic-like signal that belongs to a real-valued sequence  $x[n]$ , first the DFT is obtained using the FFT algorithm for real valued data presented in Chapter 2.8.1. Next, the data is modified as given in Equation (2.36). The real valued FFT only yields values for  $k = 0 \dots N/2$ , whereas it is noted that  $X[N/2]$  is stored as the imaginary part of the 0Hz element  $X[0]$ . For the  $N$ -point inverse DFT, however,  $N$  complex numbers have to be saved, which requires  $2N$  memory locations. By splitting the inverse DFT (IDFT) in the IDFT of the even and the IDFT of the odd numbered samples, the additionally needed space can reside anywhere in memory and does not have to be contiguous to the  $N$  memory locations, in which the result of the real valued DFT are saved.

The inverse DFT to obtain the even numbered samples is

$$x[2r] = \sum_{k=0}^{N-1} X[k] W_N^{-2rk}, \quad r = 0 \dots N/2 - 1. \quad (2.37)$$

As  $W_N^{-2r(k+N/2)} = W_N^{-2rk}W_N^{-rN} = W_{N/2}^{-rk} \cdot 1 = W_{N/2}^{-rk}$ , the last equation can also be written as

$$x[2r] = \sum_{k=0}^{N/2-1} (X[k] + X[k + N/2]) W_{N/2}^{-rk}, \quad r = 0 \dots N/2 - 1 \quad (2.38)$$

This can be identified as the  $N/2$ -point inverse DFT of the spectral sequence  $G[k] = X[k] + X[k + N/2]$ ,  $k = 0 \dots N/2 - 1$ . Using Equation (2.36) and neglecting the steady-state part given as  $X[0]$  to obtain an offset-free inverse analytic-like signal, Equation (2.38) can be expressed as

$$x[2r] = X[N/2] + \sum_{k=1}^{N/2-1} X[k] W_{N/2}^{-rk}, \quad r = 0 \dots N/2 - 1. \quad (2.39)$$

The inverse DFT to obtain the odd numbered samples is given as

$$x[2r + 1] = \sum_{k=0}^{N/2-1} (X[k] - X[k + N/2]) W_N^{-k} W_{N/2}^{-rk}, \quad r = 0 \dots N/2 - 1, \quad (2.40)$$

which can again be simplified using Equation (2.36) and neglecting the DC component  $X[0]$ :

$$x[2r + 1] = X[N/2] + \sum_{k=1}^{N/2-1} X[k] W_N^{-k} W_{N/2}^{-rk}, \quad r = 0 \dots N/2 - 1. \quad (2.41)$$

The  $N$ -point inverse Fourier transform has been split into the two  $\frac{N}{2}$ -point inverse Fourier transforms of the sequences

$$Y_1[k] = \begin{cases} X[N/2] & k = 0 \\ 2X[k] & 1 \leq k < N/2 \end{cases}, \quad k = 0 \dots N/2 - 1 \quad (2.42)$$

and

$$Y_2[k] = \begin{cases} -X[N/2] & k = 0 \\ 2X[k] W_N^{-k} & 1 \leq k < N/2 \end{cases}, \quad k = 0 \dots N/2 - 1. \quad (2.43)$$

The inverse DFT of  $Y_1[k]$  yields the even-numbered points of the time sequence, the inverse Fourier transform of  $Y_2[k]$  yields the odd-numbered points. The sequence  $Y_2[k]$  can be constructed in any arbitrary memory location. Then, two  $N/2$ -point inverse DFTs are necessary to obtain the even and odd numbered samples of the complex analytic-like signal. For the envelope detection, the absolute value of the complex-valued analytic-like sequence is of interest. As first step, the absolute values of the complex values of  $y_1[n]$  can be calculated. These are stored in the memory locations where the real parts of the sequence had been stored before. Next, the absolute values of the odd-numbered

samples, given as  $y_2[n]$ , is calculated and stored in the memory locations where the imaginary parts of  $y_1[n]$  had been saved. The final sequence only occupies the same memory locations as the original sequence. The temporary storage used for  $Y_2[k]$  in the frequency domain resp.  $y_2[n]$  in the time domain can be used for other purposes after the envelope signal has been calculated.

Calculating the absolute value of the envelope signal involves evaluating  $N$  square roots. However, for most signal processing steps, the squares of the absolute values can be used as well. This avoids the computational effort that is associated with calculating the square root. Especially for distinguishing signals from noise, the squared values is sufficient.

Envelope detection using the Hilbert transform is beneficial when compared to other time- or frequency-based approaches. Figure 2.23a shows the signal

$$f(t) = e^{-\gamma(t-t_d)^2} \sin(2\pi f_0 t), \quad (2.44)$$

an amplitude modulated signal with carrier frequency  $f_0 = 1$  MHz. The modulating exponential function has the decay coefficient  $\gamma = 3 \cdot 10^{11}$  and the delay  $t_d = 5$  ms. The magnitude spectrum of the signal is shown in Figure 2.23b. The signal has been sampled

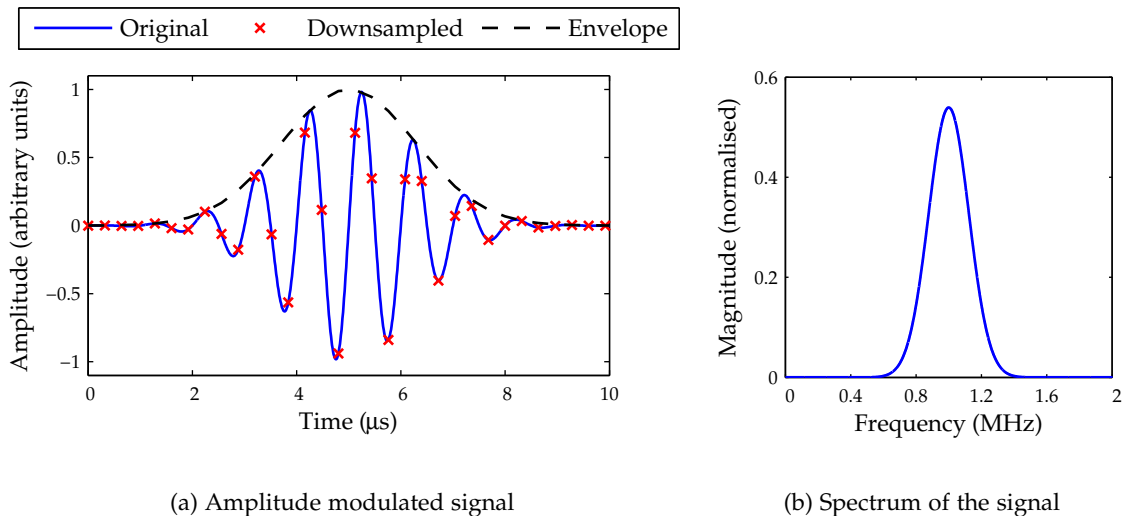


**Figure 2.23:** Signal with envelope curve obtained from the Hilbert transform of the down-sampled signal ( $f_s = 3.125$  MHz)

with a sampling frequency of 3.125 MHz, which is well below the ADC sampling frequency, so that the effects of downsampling are more pronounced. The sampled points are indicated by the black markers. Even though the sampled values at some points are well below the highest points of the continuous signal in the time domain, the dashed envelope curve, obtained with the Hilbert transform method, fits well to the original data. Again, the Shannon-Nyquist sampling theorem explains why: from the sampled signal, information can be unambiguously reconstructed for signals with frequencies lower than the Nyquist frequency  $f_N = 1.5625$  MHz. Figure 2.23b shows, that the signal  $f(t)$  contains no (or better to say only a negligible amount) of signals of frequencies above the Nyquist frequency, thus the Shannon-Nyquist sampling criterion is met. Therefore, the complete envelope curve information is contained in the sampled signal, which can be extracted using the presented Hilbert transform method. This would not be as simple from the sampled signals in the time domain. Other approaches to obtain the envelope curve include filter-based methods, which pose the challenge to avoid magnitude or phase distortions in the signal during the filter design.

#### **2.8.4 Data Compression and Wireless Transfer**

The envelope curve of a signal is helpful to compress the data from wireless measurements, before it is transmitted to the server. With the limited transmission speed of 38400 bps for the wireless communication channel, transmitting the full 4096 samples with 16 bit each, as they are stored in memory, would take approximately 1.71 s if only the raw data is considered. Usually, at least a lightweight communication protocol has to be implemented to ensure the integrity of the data, which will add to the amount of data to transmit. To reduce the power consumption of the device, it is desirable to minimize the duration of transmission, as the wireless unit consumes more power when transmitting data than when receiving data or being shut down to a standby-mode. Keeping transmissions short also helps to use the available bandwidth of the wireless channel efficiently if multiple nodes communicate on the same link.

Two separate approaches are considered to decrease transmission times: data detection and data compression. Data detection means that signals are distinguished from noise, and only significant data is transmitted. Data with zero information, i.e. noise, is omitted. Data compression makes use of the fact, that the ADC only offers 12 bit resolution and not 16 bit. Thus, transmitting samples as 16 bit data would also add to the amount of data without providing additional information.

#### 2.8.4.1 Data detection

A typical signal in ultrasonic measurements consists of one or more burst signals with only noise in between these signals. An example for such a noisy signal is shown in Figure 2.24. The envelope curve of the signal can be obtained using the Hilbert transform as described in the last section. A threshold is selected that is just above the noise level. If the envelope curve rises above this threshold, the following samples are considered as information containing signals. The signal is assumed to end, when the threshold again falls below the threshold. This process is repeated until all signals have been extracted and their start and end points are saved.

Based on the previous considerations, it may seem sufficient to transmit the envelope signal once it is calculated instead of the original signal. However, this is unfavorably for

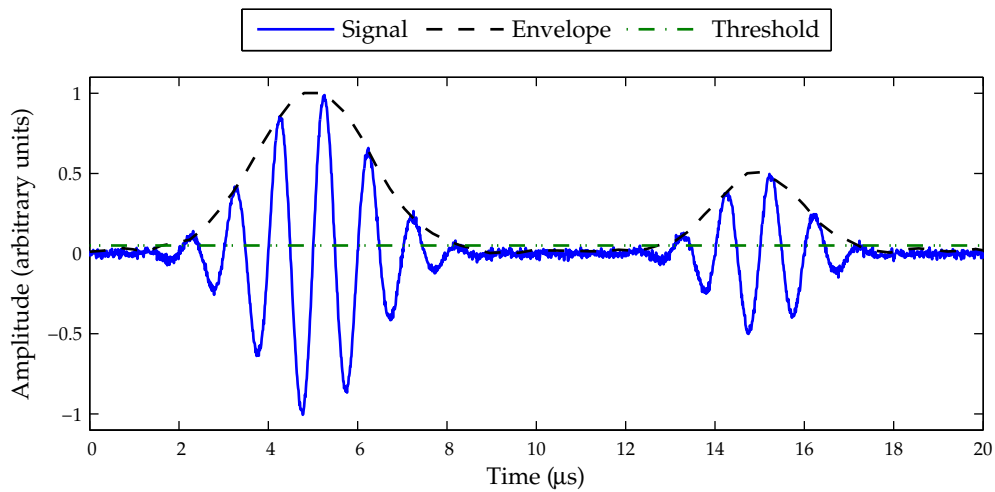


**Figure 2.24:** Example for a noisy measurement signal with two signal bursts. The envelope curve is obtained from the Hilbert transform.

two reasons: first, the original samples are 12 bit unsigned integer values. The envelope signal is calculated using the FPU in 32 bit floating point precision. Thus, the amount of data to transmit the envelope signal – if the precision shall not be reduced – is more than 2.5 times the amount of data to transmit the original samples. Second, if only the envelope signal is transmitted, the phase information contained in the original samples is lost, which prevents any signal evaluation methods for which more information besides the amplitude is needed. Therefore, only the original samples are sent. If a laptop or regular PC serves as the central server, its computational power commonly is notably higher than the computational power of the microprocessor. In this case, repeating the calculations that have been done on the microprocessor on the central server will be faster than transmitting the whole transformed data set with full precision, and will also need less energy drawn from the batteries that supply the ultrasonic device. If, however, transmission of the Fourier or Hilbert transformed data is desired, the subsequently described data transmission structure can be adapted.

#### 2.8.4.2 Data compression

The sampled signals are stored as 16 bit values in memory. However, as the ADC samples the incoming analog signal with only 12 bit, only the lower 12 digits of the 16 bit binary number are significant. Therefore, two 12bit samples can be combined to form three 8bit packages, which is the packet size used for the serial communication. Figure 2.25 illustrates this re-packing. In C, the repacking can be realized as pure combination of bit shifts and bitwise logical operations. The code is given in Figure 2.26. The compression

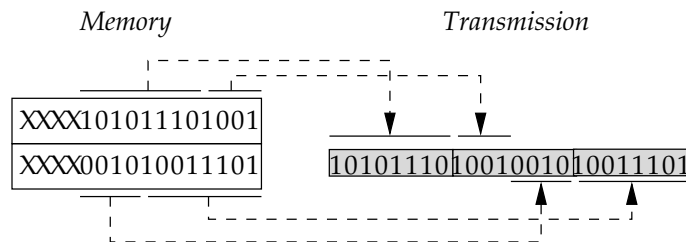


**Figure 2.25:** Repacking of 12-bit data into 8-bit packets for transmission. X describes insignificant bits which contain no information and thus are not transmitted.

```

// send_wireless(byte n) transmits data,
// n is assumed to be an 8 bit variable
send_wireless(data[0] >> 4);
send_wireless(data[0] << 4 | ((0x0FFF & data[1] >> 8));
send_wireless(data[1]);

```

**Figure 2.26:** C-Code for repacking of 12-bit data into 8-bit packets. The send\_wireless function only takes an 8-bit argument, thus only the low 8 bits are used.

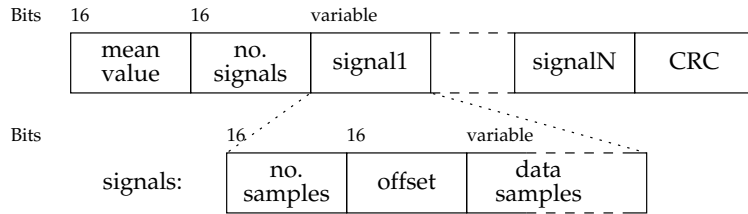


**Figure 2.27:** Data structure for the transfer of the samples to the server

must be reversed on the receiving server side to obtain the original values.

#### 2.8.4.3 Data transmission protocol

Before being transmitted, the extracted data samples have to be encoded into a data structure which allows to recover all information. The data structure is shown in Figure 2.27. For the following discussion, a “signal” refers to one identified wave burst, and a “sample” is one data point as sampled by the ADC. “Sequence” describes the original, full length sequence of sampling values, as it has been obtained by the ADC before any processing.

The first part of the structure is the 16 bit mean value of the signal, which is extracted as the 0 Hz component of the DFT of the original signal, as obtained when calculating the envelope curve using the Hilbert transform. The FFT algorithm gives the mean value as a floating point value, which is then rounded to the nearest (unsigned) integer value before transmission. The mean value can be used to replace the parts of the sampled sequence which were identified as noise and thus are not transmitted. Even though the mean value could also be represented as 12 bit number, the 16 bit value is easier to separate from the

rest of the transmitted package on the receiving side.

The next part of the structure is the number of signal bursts that are about to follow. The wave burst signals are then concatenated one after each other. Each of the signals can be of different length, thus the number of samples in the signal is the first 16 bit value to be transmitted for each signal. The 16 bit offset gives the index at which the signal can be found in the original sequence. Assuming that the server knows the sampling rate of the ADC in the ultrasonic device, the index can directly be converted to the time offset. The 12 bit data samples, which follow after the offset, are packed together into several 8 bit units as described before.

After all signals have been added to the structure for transmission, the CRC checksum of the entire structure (CRC checksum itself not included) is added. The calculation of a CRC checksum will be outlined in the next section. As explained in Section 2.5, the wireless module transmits data in packets, which each have their own CRC checksum. If the CRC checksum does not match the packet contents, the packet is dropped on the low communication level. This may lead to incomplete transmissions, as the wireless module does not ask for retransmission of dropped packets. As the data structure described before has a variable length, the receiver has no previous knowledge about how many bits to expect. If a packet gets corrupted during the transmission, i.e. the number of signals or samples is changed, and this corruption is missed by the low level CRC check – every checksum algorithm with a length shorter than the entire data only detects certain errors, others may remain undetected –, the receiver might expect the wrong amount of data and thus read a corrupted data set. Instead of adding the total number of bytes transferred, a CRC checksum of the entire structure is computed. The server can then check the received data structure against this checksum. If one of the intermediate packages should have been dropped, or one package has been corrupted which remained undetected, the CRC checksum will not match, or data which actually does not constitute the CRC checksum is taken to test the structure's integrity. Either case, the receiving server will most likely – within the scope of the error detection capabilities of the CRC checksum – be able to detect a corrupt transmission. This adds an extra level of error detection.

## 2.8.5 Cyclic Redundancy Check (CRC) Checksum

Cyclic redundancy check (CRC) checksums base on the mathematics of polynomials over the integers modulo 2. A binary number is thought of as the coefficients of a polynomial. For example, the binary number 1011 represents the polynomial  $x^3 + x + 1$ . A power of  $x$  can only be present or absent, but no other integer coefficients can occur as 0 and 1 are the only integers modulo 2. Any of these polynomials has a unique factorization into so-called “primitive” polynomials, comparable to prime integers.

For a  $M$ -bit CRC, a  $M$ -bit primitive polynomial is chosen, the so-called “generator polynomial”  $G$ . To compute the CRC of some data  $N$ , the polynomial representing this data is multiplied by  $x^M$  and then divided by the generator polynomial. The remainder of this operation is the CRC of the data set. Press et al. [33] provide more details and also an algorithm to calculate the CRC checksum.

Aside from the underlying mathematics, calculating the CRC can be realized with only bit-shift and logical exclusive-or (XOR) operations, which allows for a simple implementation both in software and in hardware. Calculating the CRC checksum can be done one bit at a time, i.e. the CRC checksum of a serial data stream is calculated based on the CRC checksum of the preceding bits that have already been processed, together with the next pending bit. Therefore, the CRC of the data structure that is used to transmit the sampled signals can be calculated on-the-fly when sending the whole data structure; the data structure needs not to be fully assembled in memory before transmission.

The choice of the generator polynomial determines the error detection capabilities of the CRC algorithm. Koopman and Chakravarty [21] compare the error detecting capabilities of different generator polynomials. Based on their findings, the generator polynomial 0xBAAD (hexadecimal) or  $(x^3 + x^2 + 1)(x^6 + x^5 + x^2 + x + 1)(x^7 + x^3 + 1)$  has been chosen. This polynomial offers a Hamming distance of 4 for sequences of up to 2048 bit. The Hamming distance describes the number of bites that at least have to be corrupted to obtain the same CRC as for an uncorrupted signal. Any number of corrupted bits less than the Hamming distance will always be detected as the CRCs won't match. At the

given ADC sampling rate of 8.3334 MHz, a 2048 bit sequence encoded as the structure described before could contain two signals of  $9.5\ \mu\text{s}$  each – a fairly realistic amount of data for ultrasonic signals.

## **2.9 Power Consumption and Cost of the Device**

### **2.9.1 Power Consumption**

The ultrasonic monitoring device is designed to run independently of external power supplies. Therefore, all power supply levels are chosen so that they can be provided by batteries. However, the energy provided by batteries is limited. For an autonomous operation of the monitoring device, it is desirable to prolong the time during which it can run before its batteries are depleted to the longest possible duration.

Table 2.1 lists the average current and power consumption of the separate parts. The current consumption is measured using a *Fluke 87* digital multimeter, and the average power consumption  $P$  is calculated from the current  $I$  and the supply voltage  $V$  as  $P = VI$ .

The measurements for the current consumption of the *TMS320F28335* DSP are taken with the *eZdsp<sup>TM</sup> F28335* board not connected to the PC, so that the JTAG controller does not consume additional power. The DSP is booted from flash memory. Depending on the operation that the DSP fulfills, it draws between 478 mA and 500 mA from its power supply. The necessary 5 V power supply can be provided by four or more stacked 1.5 V AA batteries. As an example, the *Energizer L91* lithium AA cell provides a capacity of over 2900 mAh. These batteries could supply the *eZdsp<sup>TM</sup> F28335* board for nearly 6 hours in continuous operation. Part of the measured power consumption has to be attributed not to the microprocessor, but to the peripherals included in the *eZdsp<sup>TM</sup> F28335* board. The nominal power consumption of the DSP is given in the data manual [39, Ch. 6.1] for different conditions of operation. Switching off unnecessary peripherals of the DSP contributes to reducing the power consumption of the device: for example powering down the flash memory – which might be done after copying the program code from flash to SARAM – reduces the current consumption by 35 mA. The *TMS320F28335* also offers different low-power sleep states, which can be implemented to further reduce the current

**Table 2.1:** Measured power consumption of the ultrasonic device

Part	Supply	Supply voltage	Current consumption active	Current consumption inactive	Power consumption active	Power consumption inactive
<i>eZdsp</i> <sup>TM</sup> F28335 board w/ connectorboard	after boot/idle	+5 V	478 mA	—	2.39 W	—
	taking averaged measurements	+5 V	500 mA	—	2.5 W	—
	calculations using FPU	+5 V	486 mA	—	2.43 W	—
	sending data	+5 V	480 mA	—	2.4 W	—
Signal conditioning circuit	positive supply	+9 V	20.4 mA	17.2 mA	184 mW	155 mW
	negative supply	−9 V	20.4 mA	17.2 mA	184 mW	155 mW
Output amplification circuit	positive supply output	+16 V	166 mA	< 1 $\mu$ A	2.66 W	—
	negative supply output	−16 V	164 mA	< 1 $\mu$ A	2.62 W	—
	driver stage	+9 V	19.2 mA	10.5 mA	173 mW	95 mW

consumption. Similarly, the current drawn by the wireless communication module can be reduced from 45 mA when listening for or receiving data, to 20  $\mu$ A in a power-down state [26]. These figures illustrate the need to implement a power saving scheme. A thorough analysis of the possibilities and the actual implementation is beyond the scope of this study and is left to future research.

The signal conditioning circuit and the driver stage of the output amplification circuit also draw significant amounts of current, both while active and inactive. Electrical switches, like contactors or transistors, could be used here to disconnect their power supplies while not in use. Only the output stage of the output amplification buffer does not need additional efforts to reduce the power consumption while inactive, as the used MOSFETs have a low quiescent current and both of them also disable current flow from the supply to the output while no input signal is active.

### 2.9.2 Cost of the Device

The prototype device is built using the *eZdsp<sup>TM</sup> F28335* evaluation board, which costs about \$500. This board allows to program the *TMS320F28335* DSP, and also offers advanced debugging capabilities. However, the cost for this board does not reflect the actual price of the ultrasonic detection device, as all the debugging options are not necessary for the ultrasonic monitoring device itself. Table 2.2 lists approximate costs for the core parts of each of the boards used in the device. The total approximated cost for the device itself are less than \$150 – casings, manufacturing, assembly and battery supplies not included. This shows that the proposed solution is economically feasible. Costs for the transducers and the contact wedges used for the contact ultrasound technique, which will be presented in the next chapter, are also necessary for other contact ultrasonic examination techniques and are not specific to the presented ultrasonic device. Therefore, these costs are not included in this estimation.

**Table 2.2:** Cost of the main active components of the ultrasonic device

Category	Part	Approximate price
Main board	<i>TMS320F28335</i> DSP	\$25
	128 K x 16 bit SARAM	\$5
	<i>Digi 9XCite</i> wireless module	\$40
Signal conditioning board	<i>LM7372</i> op-amp	\$5
Output amplification board	<i>74LS04</i> hex-inverter	< \$1
	<i>FDS4559</i> MOSFET	\$1
Connectors, passive components (for all boards)		~ \$50
Total		~ \$127

Cost estimates do not include casings, manufacturing and assembly of printed circuit boards, and battery supplies.

## CHAPTER III

### THEORETICAL AND PRACTICAL BACKGROUND FOR RAYLEIGH WAVE MEASUREMENTS IN STEEL SPECIMENS

This chapter first provides a brief introduction to wave propagation in elastic solids. It presents the different wave types that can propagate in an elastic half-space: longitudinal and shear bulk waves, and Rayleigh surface waves. Next, one method to generate Rayleigh surface waves in steel using an ultrasonic contact transducer and a plexiglass coupling wedge is described. The chapter finally considers the scattering of Rayleigh waves at cracks or notches. Measurement results are presented in the next chapter.

A number of comprehensive and authoritative books on the topic of wave propagation in elastic solids is available. For example, Achenbach [1] and Graff [13] can be referred to for more detailed information than what can be covered in this chapter. The derivations presented in this chapter follow Achenbach's [1] notation.

#### *3.1 Wave Propagation in Elastic Solids*

The derivation of the wave equations assumes linear material behavior. For quantities given as coordinates in a Cartesian coordinate system, Einstein's sum convention is employed to simplify the notation. Einstein's sum convention states that whenever an index appears twice in an expression, the expression is summed over for index values 1 to 3, e.g.

$$x_i y_i = \sum_{k=1}^3 x_k y_k = x_1 y_1 + x_2 y_2 + x_3 y_3. \quad (3.1)$$

A comma preceding an index (or a series of indices) denotes partial derivatives with respect to the corresponding coordinate(s). Einstein's sum convention also holds for the partial derivatives:

$$f_{i,ij} = \frac{\partial^2 f_1}{\partial x_1 \partial x_j} + \frac{\partial^2 f_2}{\partial x_2 \partial x_j} + \frac{\partial^2 f_3}{\partial x_3 \partial x_j}. \quad (3.2)$$

### 3.1.1 Linear Elasticity and the Wave Equation

In the linearized theory, the balance of linear momentum for a body of volume  $V$  with the surface  $S$  is given as

$$\int_S t_i \, dA + \int_V \rho f_i \, dV = \int_V \rho \ddot{u}_i \, dV \quad (3.3)$$

where  $\rho$  is the material's density,  $t_i$  is the vector of surface traction, and  $u_i$  is the particle displacement vector. Dots above a symbol denote partial derivatives with respect to time.

The traction vector  $t_i$  on the surface  $S$  is given by Cauchy's stress formula

$$t_i = \sigma_{ji} n_j \quad (3.4)$$

with  $n_j$  the outwards unit normal vector on the surface  $S$ .  $\sigma_{ji}$  is Cauchy's stress tensor. Substituting Cauchy's stress formula into the balance of linear momentum and using Gauss' theorem, which for an arbitrary tensor  $a_{jkl\dots p}$  is given as

$$\int_S n_i a_{jkl\dots p} \, dS = \int_V a_{jkl\dots p,i} \, dV, \quad (3.5)$$

the balance of linear momentum can be expressed as the volume integral

$$\int_V (\sigma_{ji,j} + \rho f_i - \rho \ddot{u}_i) \, dV = 0. \quad (3.6)$$

Since the balance of linear momentum has to hold for any arbitrary volume in a continuum, the integrand has to vanish at every point inside  $V$ , which gives Cauchy's first law of motion

$$\sigma_{ji,j} + \rho f_i - \rho \ddot{u}_i = 0. \quad (3.7)$$

The balance of angular momentum for a linear elastic solid yields that the stress tensor is symmetric, i.e.  $\sigma_{ji} = \sigma_{ij}$ .

For a homogeneous, isotropic, linearly elastic solid, Hooke's law expresses the stress tensor in terms of the small strain tensor  $\varepsilon_{ij}$ ,

$$\sigma_{ij} = \lambda \varepsilon_{kk} \delta_{ij} + 2\mu \varepsilon_{ij}, \quad (3.8)$$

where  $\delta_{ij}$  is the Kronecker delta, defined as

$$\delta_{ij} = \begin{cases} 1 & \text{for } i = j \\ 0 & \text{else.} \end{cases} \quad (3.9)$$

$\lambda$  and  $\mu$  are Lamé's elastic constants. The small strain tensor  $\varepsilon_{ij}$  can be expressed in terms of the displacement  $u_i$  as

$$\varepsilon_{ij} = \frac{1}{2}(u_{i,j} + u_{j,i}). \quad (3.10)$$

Clearly, the displacement tensor is symmetric. Substituting Hooke's law and the strain-displacement relation into Equation (3.7) yields the equation of motion in terms of the displacement,

$$\mu u_{i,jj} + (\lambda + \mu)u_{j,ji} + \rho f_i = \rho \ddot{u}_i. \quad (3.11)$$

The last equation can also be stated in vector notation as

$$\mu \nabla^2 \mathbf{u} + (\lambda + \mu) \nabla \nabla \cdot \mathbf{u} = \rho \ddot{\mathbf{u}}, \quad (3.12)$$

where body forces  $f$  have been neglected.

Further analysis of wave phenomena presented in this study will be limited to the case of plane waves.

### 3.1.2 Propagation of Plane Longitudinal and Shear Waves

A plane displacement wave, which propagates in the direction defined by the unit propagation vector  $\mathbf{p}$  with phase velocity  $c$ , and for which the particle displacement is in the direction of the unit displacement vector  $\mathbf{d}$ , is given by

$$\mathbf{u} = f(\mathbf{x} \cdot \mathbf{p} - ct)\mathbf{d}. \quad (3.13)$$

In the general case,  $f$  is an arbitrary function. The vector  $\mathbf{x}$  denotes the position vector. For plane waves, it is assumed that the wavefront's displacement, stress and strain are independent from the position  $\mathbf{x}$  in the plane  $\mathbf{x} \cdot \mathbf{p} = \text{const.}$ , which is perpendicular to the propagation direction  $\mathbf{p}$ .

Substituting expression (3.13) for a plane wave into the equations of motion (3.12) yields

$$(\mu - \rho c^2)\mathbf{d} + (\lambda + \mu)(\mathbf{p} \cdot \mathbf{d})\mathbf{p} = 0. \quad (3.14)$$

Since the propagation vector  $\mathbf{p}$  and the displacement vector  $\mathbf{d}$  are two different unit vectors, the last equation can only be satisfied for either  $\mathbf{p} = \pm \mathbf{d}$  or  $\mathbf{p} \cdot \mathbf{d} = 0$ .

$\mathbf{p} = \pm \mathbf{d}$ : The particle displacement is parallel to the propagation direction of the wave.

This wave type is therefore called a *longitudinal wave*. As  $\mathbf{p} \cdot \mathbf{d} = \pm 1$ , the wave speed is  $c^2 = (\lambda + 2\mu)/\rho = c_L^2$ .

$\mathbf{p} \cdot \mathbf{d} = 0$ : The particle displacement is perpendicular to the direction of propagation. This

wave is therefore called a *transverse* or *shear wave*. As  $\mathbf{p} \cdot \mathbf{d} = 0$ , the wave speed is  $c^2 = \mu/\rho = c_T^2$ .

Since  $\lambda \geq 0$  and  $\mu \geq 0$ , the longitudinal wave speed will always be higher than or equal to the shear wave speed.

In general, the displacement vector  $\mathbf{d}$  for a shear wave can have any direction in a plane normal to the propagation vector  $\mathbf{p}$ . However, if a two-dimensional plane of propagation is considered (e.g. the  $(x_1, x_2)$ -plane) which contains the propagation vector  $\mathbf{p}$ , then two types of shear waves can be distinguished: if the displacement vector  $\mathbf{d}$  also lies in the plane of propagation, the shear wave is called a “vertically polarized” or SV-wave; if  $\mathbf{d}$  is perpendicular to the plane of propagation, the wave is called a “horizontally polarized” or SH-wave.

In a homogeneous, isotropic material, the longitudinal and the shear wave speed are nondispersive, i.e. frequency-independent. Table 3.1 gives approximate values for the density and the wave propagation speeds in steel, the propagation medium considered in this work.

**Table 3.1:** Approximate material properties for steel (cf. [1, Table 4.1])

Property	Value
Density $\rho$	7800 kg/m <sup>3</sup>
Longitudinal wave speed $c_L$	5900 m/s
Shear wave speed $c_T$	3200 m/s

### 3.1.3 Reflection and Refraction of Plane Waves at Interfaces

In an unbound infinite medium, longitudinal and shear waves propagate independently of and without interfering with each other. However, as soon as the propagation medium

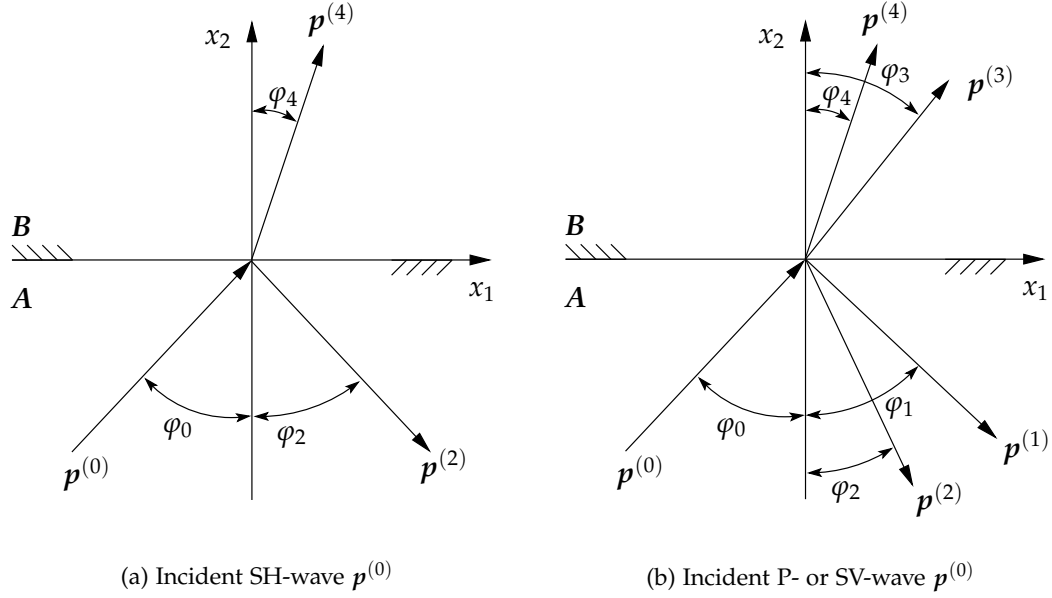


**Figure 3.1:** Reflection and refraction of waves at an interface

is only semi-infinite in the direction of propagation, and the medium shares a common interface with another medium, waves are reflected and refracted at this interface. Figure 3.1 illustrates how the incident wave  $p^{(0)}$  in material  $A$  in the most general case gives rise to four waves: two reflected waves with propagation vectors  $p^{(1)}$  and  $p^{(2)}$  in  $A$  and two refracted waves with propagation vectors  $p^{(3)}$  and  $p^{(4)}$  in material  $B$ . For convenience, the waves are subsequently referred to by their propagation vectors.

For the discussion of reflection and refraction, only time harmonic plane waves, propagating in the  $(x_1, x_2)$ -plane, are considered. The displacement field for such a wave is given as

$$\mathbf{u}^{(n)} = A_n \mathbf{d}^{(n)} \exp \left[ k_n \left( x_1 p_1^{(n)} + x_2 p_2^{(n)} - c_n t \right) \right], \quad (3.15)$$

where  $n$  denotes the index of the wave,  $n = 0 \dots 4$ ,  $c_n$  is the respective phase velocity of the wave  $n$  – the shear wave velocity in the respective medium for SV- or SH-waves, or the longitudinal wave velocity in the respective medium for P-waves – and  $k_n = \omega/c_n$  is called the wave number. Note that all waves which appear due to reflection and refraction of  $p^{(0)}$  have the same angular frequency  $\omega$ .

If the incident wave  $p^{(0)}$  is a SH-wave, it will only give rise to two waves: one reflected

and one refracted SH-wave. The propagation vector of these waves,  $\mathbf{p}^{(2)}$  and  $\mathbf{p}^{(4)}$ , enclose the angles  $\varphi_2$  and  $\varphi_4$  with the  $x_2$  axis as illustrated in Figure 3.1a. Assuming an ideal contact at the interface, the displacements and stresses have to be continuous, which is met if

$$\varphi_2 = \varphi_0 \quad \text{and} \quad \sin \varphi_4 = \frac{c_T^B}{c_T^A} \varphi_0. \quad (3.16)$$

The amplitudes  $A_i$  of the waves are given by

$$\frac{A_2}{A_0} = \frac{\mu^A \cos \varphi_0 - \mu^B c_T^A / c_T^B \cos \varphi_4}{\mu^A \cos \varphi_0 + \mu^B c_T^A / c_T^B \cos \varphi_4} \quad \text{and} \quad \frac{A_4}{A_0} = \frac{2\mu^A \cos \varphi_0}{\mu^A \cos \varphi_0 + \mu^B c_T^A / c_T^B \cos \varphi_4}. \quad (3.17)$$

If, however, the incident wave  $\mathbf{p}^{(0)}$  is a P-wave or a SV-wave, it will give rise to four waves: one reflected ( $\mathbf{p}^{(1)}$ ) and one transmitted ( $\mathbf{p}^{(3)}$ ) P-wave, and one reflected ( $\mathbf{p}^{(2)}$ ) and one transmitted ( $\mathbf{p}^{(4)}$ ) mode converted SV-wave. Again assuming perfect contact, the equilibrium of displacement and traction at the interface yield

$$k_0 \sin \varphi_0 = k_1 \sin \varphi_1 = k_2 \sin \varphi_2 = k_3 \sin \varphi_3 = k_4 \sin \varphi_4 \quad (3.18a)$$

$$k_0 c_0 = k_1 c_L^A = k_2 c_T^A = k_3 c_L^B = k_4 c_T^B. \quad (3.18b)$$

These equations constitute Snell's law for the ultrasonic waves,

$$\sin \varphi_1 = \frac{c_L^A}{c_0} \sin \varphi_0, \quad \sin \varphi_2 = \frac{c_T^A}{c_0} \sin \varphi_0, \quad (3.19a)$$

$$\sin \varphi_3 = \frac{c_L^B}{c_0} \sin \varphi_0, \quad \sin \varphi_4 = \frac{c_T^B}{c_0} \sin \varphi_0. \quad (3.19b)$$

The amplitudes of the waves also follow from the equilibrium of displacement and traction at the interface. For two waves  $m$  and  $n$ , the equations

$$A_m d_1^{(m)} = A_n d_1^{(n)} \quad \text{and} \quad A_m d_2^{(m)} = A_n d_2^{(n)} \quad (3.20)$$

have to hold, where  $d_1$  is the particle displacement in the  $x_1$  direction, and  $d_2$  the particle displacement in the  $x_2$  direction. These conditions yield a system of equations which can be found as Equation 5.86 in [1]. These equations and their analytic solutions will not be considered here. Note that when a wave is reflected at the interface, the reflected wave of the same type will enclose the same angle as the incident wave, i.e. for an incident

P-wave, the angle of the reflected P-wave will be equal to the incident angle, and for an incident SV-wave, the angle of the reflected SV-wave will be equal to the incident angle.

Consider the expression for  $\sin \varphi_3$ , given as the left expression in Equation (3.19b) for the case of an incident P-wave, i.e.  $c_0 = c_L^A$ . If the longitudinal wave speed  $c_L^B$  in medium **B** is greater than the longitudinal wave speed in medium **A**, a P-wave  $\mathbf{p}^{(0)}$  in medium **A** will only give rise to a P-wave in medium **B** for  $\frac{c_L^B}{c_L^A} \sin \varphi_0 < 1$ . This expression yields the critical incident angle

$$\varphi_{0,\text{cr}} = \arcsin \frac{c_L^A}{c_L^B}. \quad (3.21)$$

If the incident angle is equal or higher than the critical angle,  $\varphi_0 \geq \varphi_{0,\text{cr}}$ , the energy that for smaller angles would propagate as a P-wave in medium **B** will propagate as a surface wave along the interface.

### 3.1.4 Propagation of Rayleigh Waves

Besides showing reflection and refraction phenomena, the presence of a surface for a semi-infinite medium also makes the propagation of a third type of wave possible: Rayleigh surface waves propagate along the free surface of an elastic semi-infinite medium. These waves are confined to the vicinity of the boundary, and the displacement field decays exponentially with the distance from the free surface. As the wave propagates along the surface, most of the energy carried by the wave is bound to the surface. This means, the energy only spreads in two dimensions and not in three as for bulk waves. Therefore, Rayleigh waves suffer less from geometric attenuation than bulk waves.

Consider a plane time-harmonic wave propagating in the  $x_1$  direction along the surface  $x_2 = 0$  with the displacement field

$$u_1 = E e^{-bx_2} \exp[jk(x_1 - ct)] \quad (3.22a)$$

$$u_2 = F e^{-bx_2} \exp[jk(x_1 - ct)] \quad (3.22b)$$

$$u_3 = 0. \quad (3.22c)$$

The coefficients in these equations bear no indices, as only one medium is considered. The real part of  $b$  is assumed to be positive so that the wave amplitude decreases with

increasing depth. The wave speed  $c$  and the wave number  $k = \omega/c$  are quantities describing Rayleigh waves, and their values are distinct from the values for longitudinal or shear waves.

Substituting this displacement field into the equations of motion (3.12) yields two homogeneous equations for the constants  $E$  and  $F$ . For these equations to have a nontrivial solution, the determinant of the coefficients of the arising system of equations must vanish. This leads to the equation

$$[c_L^2 b^2 - (c_L^2 - c^2) k^2] [c_T^2 b^2 - (c_T^2 - c^2) k^2] = 0, \quad (3.23)$$

with the roots

$$b_1 = k \sqrt{1 - \frac{c^2}{c_L^2}} \quad \text{and} \quad b_2 = k \sqrt{1 - \frac{c^2}{c_T^2}}. \quad (3.24)$$

The roots are real and positive if  $c < c_T < c_L$ . Corresponding amplitude ratios are

$$\left(\frac{F}{E}\right)_1 = -\frac{b_1}{jk} \quad \text{and} \quad \left(\frac{F}{E}\right)_2 = -\frac{jk}{b_2}. \quad (3.25)$$

The complex amplitude ratios show that the displacement  $u_1$  and  $u_2$  are  $90^\circ$  out of phase. The particles move in an elliptical shape when a Rayleigh wave propagates. The semi-major axes of the ellipses are normal and the semi-minor axes are parallel to the free surface. At the surface, the normal displacement of particles is about 1.5 times the in-plane displacement.

Substituting the roots  $b_1$  and  $b_2$  and the amplitude ratios  $(F/E)_1$  and  $(F/E)_2$  into the displacement field (3.22) yields a general solution which depends on the amplitudes  $E_1$  and  $E_2$ . The conditions for a stress free surface,  $\sigma_{21}|_{x_2=0} = 0$  and  $\sigma_{22}|_{x_2=0} = 0$  yield two homogeneous equations for these amplitudes. Again, for a nontrivial solution to exist, the determinant of the coefficients of the amplitudes  $A_1$  and  $A_2$  has to vanish, which leads to the Rayleigh wave equation for the phase velocity  $c_R$  of Rayleigh waves:

$$\left(2 - \frac{c_R^2}{c_T^2}\right)^2 - 4\sqrt{1 - \frac{c_R^2}{c_L^2}}\sqrt{1 - \frac{c_R^2}{c_T^2}} = 0. \quad (3.26)$$

Note that the Rayleigh wave equation is frequency-independent, thus Rayleigh surface waves are non-dispersive. It can be shown that only one positive real root exists for Equation (3.26), for which  $0 < c_R < c_T$ .

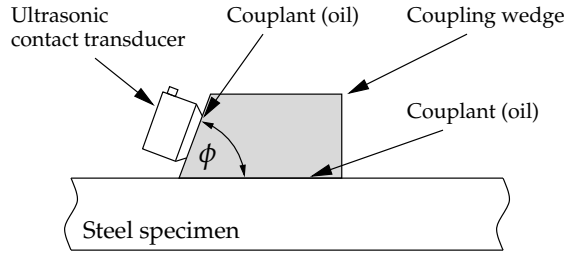
The displacement amplitudes of Rayleigh waves decay exponentially with the depth, proportional to  $e^{-bx_2}$ . To estimate the maximum occurring amplitudes, only the root  $b_2$  needs to be considered as  $c_L > c_T$  yields  $b_2 < b_1$ , and the slower decaying part dominates the maximum amplitudes. Substituting Equations (3.24) into the displacement field (3.22), and noting that the wave number  $k$  is defined as  $k = 2\pi/\lambda$ , it becomes apparent that the amplitudes of the displacement field decay proportional to  $\exp(-\eta x_2/\lambda)$ , where  $\eta = 2\pi\sqrt{1 - c^2/c_T^2}$ . The ratio  $c_R/c_T$  typically takes values in the range 0.862–0.955 (cf. [1, Table 5.1]), depending on Poisson's ratio  $\nu$  ( $0 \leq \nu \leq 0.5$ ). Thus, at a depth of one wavelength from the surface, the amplitudes decay to 15 % or less of the amplitudes at the top. As the stress shows similar decay, it is obvious that most of the energy of Rayleigh waves propagates in a layer up to one wavelength depth from the surface.

Using the values for  $c_R$  and  $c_L$  given in Table 3.1, the Rayleigh wave equation (3.26) yields the Rayleigh wave speed  $c_R = 2963 \text{ m/s}$ . The corresponding wave length for a  $f = 1 \text{ MHz}$  frequency signal is  $\lambda = c_R/f = 2.963 \text{ mm}$ .

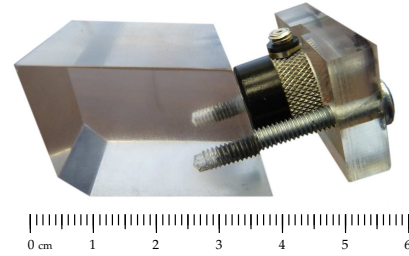
### 3.2 Generation of Rayleigh Waves Using Contact Wedges

The ultrasonic device uses two *Panametrics A103S* 1 MHz longitudinal wave contact transducers, which have a circular contact face of 0.5 in in diameter. One transducer generates ultrasonic waves, the second transducer detects them. The transducers are attached to coupling wedges, which at the interface of wedge and steel convert longitudinal waves in the wedge to Rayleigh waves in the steel specimen, and vice versa. Figure 3.2a illustrates how a transducer and a wedge are set up and attached to a steel specimen. Couplant oil, which is added on the interfaces between the transducers and the wedges, and also on the interfaces between the wedges and the surface of the specimen, compensates for imperfections in the flatness of the surfaces and so improves the contact and the transmission of waves. As the thickness of the couplant layer is small compared to the overall dimensions and the wavelength, its influence will be neglected in the following treatment of the Rayleigh wave generation.

The conversion of longitudinal waves to Rayleigh waves is based on the refraction of



(a) Setup for Rayleigh wave generation



(b) Wedge with attached transducer

**Figure 3.2:** Generation of Rayleigh waves using a contact transducer and a wedge

waves at the interface. As established during the presentation of reflection and refraction of waves in the preceding chapter, the refraction at an interface obeys Snell's law. Consider any type of incident wave  $p^{(0)}$  and the corresponding reflected wave  $p^{(4)}$  (cf. Figure 3.1a which illustrates this for the special case of an incident SH-wave). Denoting the angles of their respective propagation vectors with the surface normal as  $\varphi_0$  resp.  $\varphi_4$ , and their respective (depending on wave type and material) phase velocities as  $c_0$  resp.  $c_4$ , Snell's law (cf. also Equation (3.19)) states

$$c_0 \sin \varphi_0 = c_4 \sin \varphi_4. \quad (3.27)$$

Let  $c_W$  denote the phase velocity of a longitudinal wave in the wedge,  $c_R$  as before the Rayleigh wave speed in steel, and  $\phi$  the angle of the incident longitudinal wave with the bottom surface normal in the wedge; geometric considerations directly yield that this angle is identical to the incline of the front surface to which the transducer is attached, as shown in Figure 3.2a. A Rayleigh wave propagates along the surface, thus its propagation vector is at a  $90^\circ$  angle to the surface normal. As  $\sin 90^\circ = 1$ , the appropriate incident angle for the P-wave in the wedge, which will give rise to a Rayleigh wave in the steel surface, is

$$\phi = \arcsin \frac{c_W}{c_R}. \quad (3.28)$$

Note that the arcsine yields a real result only for  $-1 \leq \frac{c_W}{c_R} \leq 1$ , which in turn – since the Rayleigh wave speed is positive – implies  $c_W \leq c_R$ . That is, the longitudinal wave speed in the wedge has to be lower than the Rayleigh wave speed in steel to generate a Rayleigh

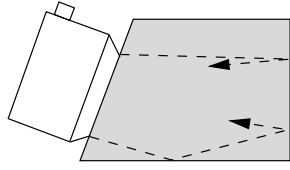
wave with the presented contact wedge method. The arcsine is strictly monotonically increasing in  $[0, 1]$ , therefore a low ratio of  $\frac{c_W}{c_R}$  will result in a smaller angle  $\phi$ , which allows the wedges to be more compact. Substituting Equation (3.28) into Snell's law (3.19b) for refracted P- and SV-waves that are generated by an incident P-wave, and noting that  $c_R^S < c_T^S < c_L^S$  yields

$$\sin \varphi_3 = \frac{c_L^S}{c_S^S} > 1 \quad \text{and} \quad \sin \varphi_4 = \frac{c_T^S}{c_S^S} > 1, \quad (3.29)$$

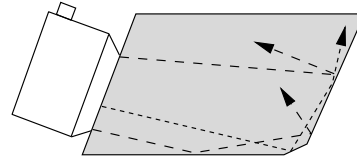
where the superscript S denotes waves in steel. Therefore, generating Rayleigh waves with a wedge cut at the critical angle in theory only gives rise to a Rayleigh wave and not to bulk waves in steel.

The longitudinal wave speed is not the only criterion for choosing the material for the wedges. A low attenuation of waves inside the wedges is also desired for efficient energy transmission. For the wedges used in this study, plexiglass has been chosen, for which the longitudinal wave speed has been measured to be  $c_W = 2750$  m/s. Using  $c_R = 2963$  m/s for the phase velocity of a Rayleigh wave in steel, the appropriate angle for the incident longitudinal wave is  $\phi = 68.1^\circ$ . Figure 3.2b shows one manufactured coupling wedge with the transducer attached. Note that the screws used to affix the transducer to the wedge are in normal orientation to the surface. Even though this configuration requires the wedges to be wider to make room for the screws, the screws are in the clamping axis of the transducer, which allows the maximum possible force to clamp the transducers to the surface, which improves the contact and therefore also the efficiency of the energy transport between the transducer and the wedge. The contact surfaces between the transducer and the wedge, and between the wedge and the specimen, should be as flat and even as possible. All other surfaces need no additional polishing and can be used with normal machine finish. A small cutout in the fixture ensures that the transducer always is attached to the same position on the wedge. Putting this cutout into the fixture instead of to the wedge allows the transducer contact surface to be even, so that it can be polished.

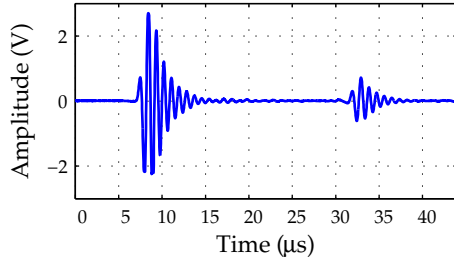
From Figure 3.2b it is apparent that the side opposing the transducer contact surface is not cut at a right angle to the bottom surface. This design mitigates the influence of



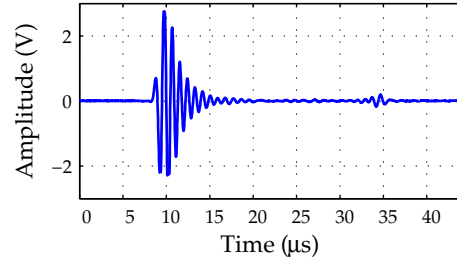
(a) Ray tracing for the wedge with right-angled opposite face



(b) Ray tracing for the wedge with sloped opposite face



(c) Time domain signal for the wedge with right-angled opposite face. The amplitude ratio between first and second signal is approximately 3.8.



(d) Time domain signal for the wedge with sloped opposite face. The amplitude ratio between first and second signal is approximately 14.4.

**Figure 3.3:** Different coupling wedges and the resulting time domain signals. The signals have been time shifted to account for the propagation delay inside the wedges. The remaining time differences are due to slightly different distances between the wedges.

reflected waves, which propagate inside the wedge and which are, due to the low attenuation coefficient of the plexiglass, not sufficiently attenuated inside the wedge. Pruell [34], Bermes [6] and Herrmann [15] examined and improved similar wedge designs for the generation of Rayleigh or Rayleigh-Lamb waves. Their designs all featured a certain headroom into which reflected wave are guided, and inside which these waves are ideally trapped, so that they do not show up as spurious signals during the measurements.

Figure 3.3 compares two different wedge designs that have been examined in this study. The top-left wedge, Figure 3.3a, has the opposite side cut at a right angle to the bottom surface. The specimen contact surface of the improved wedge, shown at the top-right in Figure 3.3b, has the same dimensions as the bottom surface of the first wedge, but additional bulk headroom is added to the right. The height of both wedges is equal. Both figures show examples of possible traces for ultrasonic rays. The transducer generates

an ultrasonic beam, which is not confined to a cylindrical pattern around the central axis of the beam, the so-called acoustic axis. The beam rather spreads in a (truncated) cone-like shape with energy spread over the cone in a Gaussian distribution centered at the acoustical axis. Figure 3.3a shows how some example rays propagate inside the first wedge with the right-angled side. Waves are reflected back from the opposite side to the transducer contact surface, from where they bounce back down to the specimen contact surface and give rise to a spurious Rayleigh wave signal. Figure 3.3c shows the corresponding time domain signal for a pulse input to the transducer, for which the wedge has been attached to a steel plate, and a second wedge-transducer-pair has been used to detect the generated Rayleigh waves. A reflected signal is observed about  $24\ \mu\text{s}$  after the main signal. The amplitude of the first signal is about 3.8 times the amplitude of the second signal. Similarly, Figure 3.3b shows example traces of ultrasonic rays in the improved wedge, which features an additional headroom and a sloped back surface. Most of the spurious signals are reflected to the top surface of the wedge and not back to the transducer contact surface. The exact angles at the back side are not critical as long as they ensure that energy is not directly reflected back to the transducer contact surface. Figure 3.3d shows the resulting time domain signal. The ratio between the first incident and the reflected signal increases compared to the first wedge design, and now the amplitude of the first signal is about 14.4 times the amplitude of the reflected signal. This increase is attributed to the improvement of both, the generating and the receiving wedge.

The improvement in signal quality is not as important for manual inspections as it is for autonomous damage assessment as intended in this study. During a manual inspection, the human operator can rather easily distinguish the original from a reflected signal, as long as the occurrence of both signals is consistent and known a priori. The operator can also change the position or distances of the wedges if the reflected signals should interfere with actual damage-indicating data. However, for autonomous damage assessment without a human operator involved, where the position of the transducer is fixed over a period of time, a clear signal with as less spurious signal content as possible greatly

improves the reliability of the assessment, and avoids false alerts. The clearness of the signal might even be further improved by adding some additional structure to the back side of the wedge, e.g. triangle-shaped vertical notches, to diffuse the reflected waves. This, however, would make the wedge manufacturing more complex and therefore also more expensive.

To determine the propagation delay that is caused by the longitudinal wave propagating inside the wedges, the propagation time of a Rayleigh wave in steel is measured for different distances between the wedges. The wavelength of the Rayleigh waves is small compared to the dimensions of the plate, so that the plate with finite dimensions can be regarded as semi-infinite medium for the propagation of Rayleigh surface waves. The propagation distances of the waves are measured between the edges of the bottom contact surfaces of the wedges. Figure 3.4 shows the propagation time for different distances between the wedges. The linear interpolation using 10 measured values is given by the least squares approximation

$$\min_{\substack{c_{R,m} > 0 \\ t_{d,m} \geq 0}} \left( \sum_{i=1}^{10} [z_i - c_{R,m}(t_i - t_{d,m})]^2 \right), \quad (3.30)$$

with  $z_i$  the propagation distances,  $t_i$  the propagation times,  $c_{R,m}$  the measured Rayleigh wave speed in steel, and  $t_{d,m}$  the measured cumulated time delay during which the waves travel the distance between the front edges of the bottom contact surfaces of the wedges to the transducers. The average delay for one wedge is therefore given as  $t_{d,m}/2$ . Linear

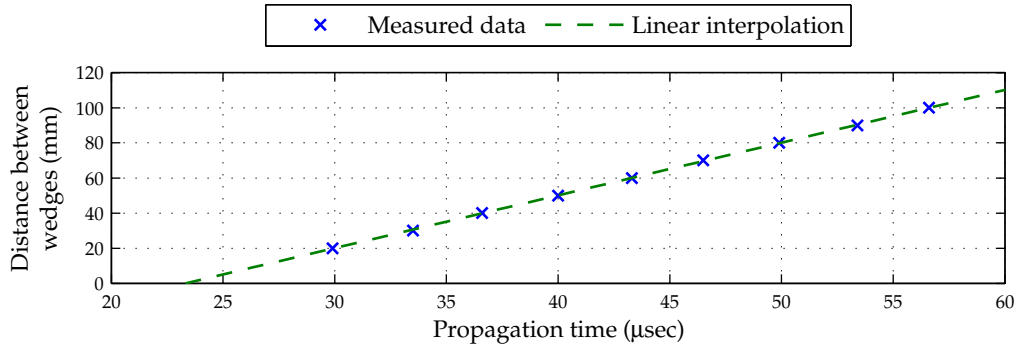


**Figure 3.4:** Measured propagation times for different propagation distances for a Rayleigh wave in steel.

interpolation of the measured data yields the Rayleigh wave speed  $c_{R,m} = 3004 \text{ m/s}$  and a cumulative propagation delay  $t_{d,m} = 23.3 \mu\text{s}$ . The difference between the theoretical Rayleigh wave speed, which was calculated using the parameters given in Table 3.1, and the actual measured wave speed is approximately 1.4 %.

### ***3.3 Crack Detection Using Rayleigh Waves***

The behavior of Rayleigh surface waves at cracks and other material flaws has been the subject of extensive research efforts. As the main objective of the study at hand is to examine the applicability of ultrasonic detection methods based on Rayleigh waves using a small self-contained device, the material presented in this section is limited to a scope which allows a phenomenological understanding of the ultrasonic measurement signals as they emerge from Rayleigh waves propagating across a surface crack. Ultrasonic measurement results will be presented in the next chapter. Some literature describing the behavior of Rayleigh waves at a crack is given below for further reference. However, this review can only present a small excerpt of the literature published on that topic. A comprehensive review of current examination techniques is beyond the scope of this study.

Achenbach [2] gives an overview over established techniques in quantitative nondestructive evaluation, and qualitatively describes the scattering of waves at cracks. Cracks, in the mathematical sense, are discontinuities in the surface of a solid body, across which the traction field is not continuous. Incident waves are reflected at the crack, which in general is of unknown size, shape or orientation. The reflection is commonly not limited to one direction, reflections of an incident wave rather generate a scattered field in the vicinity of the crack. Auld [4], Kino [20], and Mendelsohn et al. [27] derive mathematical descriptions for the scattering of acoustic waves at flaws. Cook and Berthelot [9] examine crack growth during fatigue cycle experiments in AISI 4130 steel, which originates from an elliptical “notch” in a bar. Kim and Rokhlin [19] present a low-frequency scattering model for Rayleigh waves at pit-induced cracks in AI2024-3 steel samples and compare their theoretical results to experimental data. Another study on scattering of Rayleigh

waves is by Masserey and Mazza [24], who simulate scattering at cracks in St37-2 steel and compare it to their experimental results.

The present study uses a pitch-catch setup, in which one transducer generates waves, and a second one detects the scattered signals. For the ultrasonic detection device, the pitch-catch setup offers advantages over a pulse-echo mode operation, in which the same transducer is used for signal generation and detection. The analog-digital converter on the *TMS320F28335* DSP does not tolerate the voltage levels used to generate Rayleigh waves, therefore a sophisticated circuit design would be necessary to prevent the voltages used to generate waves from entering into the signal conditioning circuits to prevent damage to the ADC. A pitch-catch setup therefore simplifies the requirements for the design of the analog circuitry.

As a pitch-catch setup is used, the forward scattered portion of a Rayleigh wave from a crack rather than backscattered reflections at a crack is of interest. Figure 3.5 illustrates how the energy contained in an incident Rayleigh wave is divided into separate propagation paths. Due to the design of the wedge, to which the receiving transducer is attached, the receiving transducer is mainly sensitive to Rayleigh waves, and also highly directional. The amplitudes of detected bulk waves, which typically also develop during

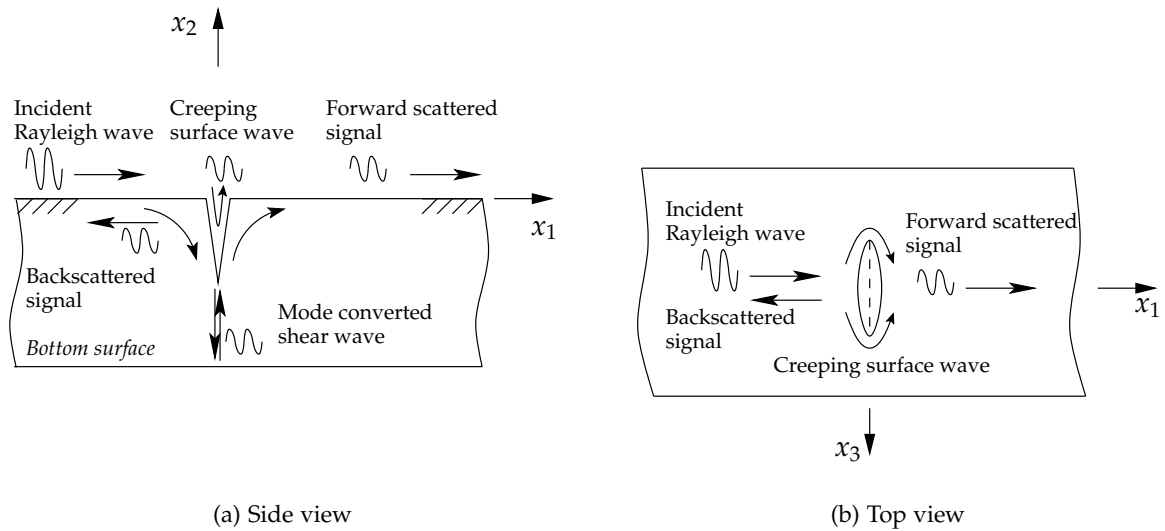


**Figure 3.5:** Scattering of Rayleigh waves at a surface crack

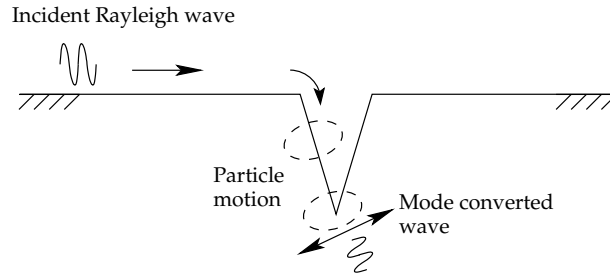


**Figure 3.6:** Conversion of a Rayleigh wave to a bulk wave at the bottom of a crack

the scattering of a wave front at a crack, will be low compared to the Rayleigh wave signals. Also, Rayleigh waves suffer less from geometric attenuation than bulk waves, an effect which becomes more pronounced with increasing propagation distances. For these reasons, only signal paths which yield to a Rayleigh wave propagating across the crack are considered.

Part of the energy of the incident wave propagates along the vertical surfaces of the crack as a creeping wave, as shown in Figure 3.5a. Viktorov [48] examined the Rayleigh wave propagation along dihedral surfaces, and he found that the amplitude of the transmitted Rayleigh wave at a  $90^\circ$  corner is about 0.7 times the amplitude of the incident wave, and up to 0.9 times for lower angles. A comparable transmission rate can be expected for the vertical surfaces of cracks. Another part of the incident energy propagates on the specimen's surface along the crack's rim, as shown in the top view Figure 3.5b. This wave and the creeping wave along the vertical surfaces propagate with the Rayleigh wave speed  $c_R$ .

Besides these pure Rayleigh wave paths, also a mode converted wave is generated as illustrated in Figure 3.6: the vertical surfaces of the crack typically enclose an angle less than  $90^\circ$ . When the Rayleigh wave that propagates along the vertical surface of the crack reaches the bottom of the crack, the particle motion of the incident surface wave excites the particles in the opposing crack surface, giving rise to a bulk wave. As seen in the last chapter, the out-of-plane displacement for Rayleigh waves is about 1.5 times the in-plane motion. Thus, more energy will be converted into a shear wave than into a longitudinal wave. The emerging shear wave propagates to the bottom of the steel plate, is reflected,

and when it reaches the crack, is converted back to a Rayleigh wave. Part of the reflected shear wave, however, does not hit the crack, and is reflected back from the top surface to the bottom surface. From there, the shear wave is again reflected back up to the crack and is converted to a Rayleigh wave. Multiple bottom-surface-bottom reflections can also occur in a similar manner.

The Rayleigh wave speed (using the measured value)  $c_{R,m} = 3004 \text{ m/s}$  and the shear wave speed in steel  $c_T = 3200 \text{ m/s}$  are of comparable magnitude, but the mode-converted shear wave travels a longer distance than the creeping Rayleigh wave. Therefore, the creeping Rayleigh wave will typically arrive earlier at the receiving transducer than the mode-converted wave. The two signals are separated by a time delay, which is proportional to the distance between the bottom of the crack and the plate bottom surface, and can therefore be distinguished in the time domain signal. The time delay could, in theory, also be used to measure the crack depth. Comparing the time delay for two cracks of depths  $D_1$  resp.  $D_2$  with negligible widths (i.e. the vertical crack surfaces are normal to the plate surface), where  $h$  denotes the height of the plate, the time delays between the direct and the mode converted wave are  $\Delta t_m = 2(h - D_m)/c_T$ ,  $m \in \{1, 2\}$ . The change in the time delay is given as

$$\Delta t = \Delta t_2 - \Delta t_1 = \frac{2(h - D_2)}{c_T} - \frac{2(h - D_1)}{c_T} = 2 \frac{D_1 - D_2}{c_T}. \quad (3.31)$$

A change in the crack depth of 1 mm will lead to a time delay of 625 ns, which is slightly more than five ADC sampling periods. In turn, the ADC sampling period of 120 ns corresponds to a change in depth of 0.19 mm. Thus, the ADC sampling rate limits the sensitivity for time-based methods. However, one should bear in mind that scattered signals typically consist of the superposition of different reflections propagating along different paths, which makes it difficult to determine the exact start of a signal with good accuracy. This, combined with the limited time resolution of the ADC, poses certain challenges to time-based damage assessment; the examination of these challenges is left to future work.

## CHAPTER IV

### ULTRASONIC MEASUREMENTS: EXPERIMENTS AND RESULTS

This chapter presents the results of preliminary ultrasonic measurements, in order to show that the proposed procedure to generate and detect Rayleigh waves can be used to monitor surface breaking cracks in steel. For this, measurements are taken in two different ways: firstly, using commercial off-the-shelf ultrasonic equipment, and secondly, using the prototype device. The measurements taken with commercial equipment are unaffected by noise in the signal conditioning circuit or other imperfections of the prototype device. Using a significantly higher sampling rate than used in prototype device, the influences of sampling and quantization errors can be examined. These measurements also allow for a quantitative analysis of the signals that are measured as part of the forward scattered wave field of a Rayleigh wave at a notch. The results from these measurements are compared to results obtained from measurements with the prototype device. The signal amplitudes and gains in all experiments are in accordance with the designated output levels and possible gain of the proposed ultrasonic device.

For the measurements with the commercial ultrasonic equipment, an *Agilent 33250A* signal generator generates a 1 MHz sine wave burst, which is amplified by a *ENI 325LA RF Power amplifier* to an output level of  $\pm 15$  V before being fed to the transducer. This output level is slightly higher than the resulting output for the  $\pm 18$  V square wave signal, however the maximum ratings of the parts in the output amplification circuit would allow to reach these voltage levels if an appropriate power supply was used. On the detection side, the amplifier that is included in a *Panametrics 5058PR pulser/receiver* amplifies the signals received by the transducer to the desired level of  $-1.5$  V to  $1.5$  V. This range corresponds to the input range of the analog-digital converter (ADC) when the DC offset is neglected. The amplifier gain during the measurements does not exceed 20 dB, a gain which the analog signal conditioning circuit can attain (cf. Chapter 2.7.2). The amplified

signal is fed into a *Tektronix TDS 5034 digital storage oscilloscope* which digitizes and saves the data with a sampling rate of  $500 \text{ MS/s}$ . To analyze the influence of the lower ADC sampling rate, the recorded signal is downsampled to  $8.3334 \text{ MS/s}$  and quantized to match the 12 bit resolution of the ADC.

#### 4.1 Test Specimen and Measurement Procedure

The proposed ultrasonic measurement method is tested with a steel plate ( $241 \text{ mm} \times 152 \text{ mm} \times 25.3 \text{ mm}$ ), into which notches of different depths have been cut using electrical discharge manufacturing (EDM) to simulate surface breaking cracks. Figure 4.1 shows the top view of the plate and the location of the notches. The dimensions of the plate, and the positions of the notches on the plate allow for the examination of one notch at a time, with negligible disturbances in the resulting scattered wave field from the edges of the plate or from adjacent notches. Table 4.1 lists the dimensions of the four notches that are examined. Changes in the width of the notches are a result of the manufacturing process. The bottom and the sides of the notches are not necessarily straight and flat, but may be coarse and vary slightly in depth as indicated in Figure 4.2 as a result of the EDM. Figure 4.2 also illustrates the pitch-catch setup that is used for the ultrasonic measurements, i.e. one transducer-wedge pair generates (or transmits) Rayleigh waves, and a second transducer-wedge pair detects (or receives) them.

For taking ultrasonic measurements, the wedges are set up on both sides of a notch

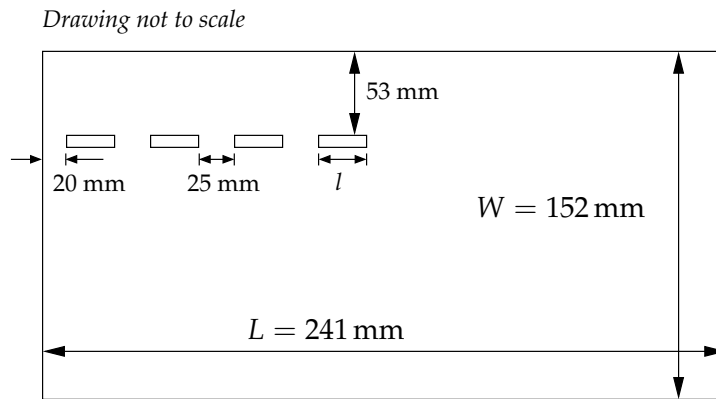


**Figure 4.1:** Test specimen with notches made using electric discharge machine

**Table 4.1:** Dimensions of the notches cut into the test specimen (measured using calipers)

No.	Depth $D$ (mm)	Width $w$ (mm)	Length $l$ (mm)
1	0.5	0.58	9.3
2	1.2	0.58	9.4
3	2.3	0.63	9.3
4	3.2	0.70	9.3

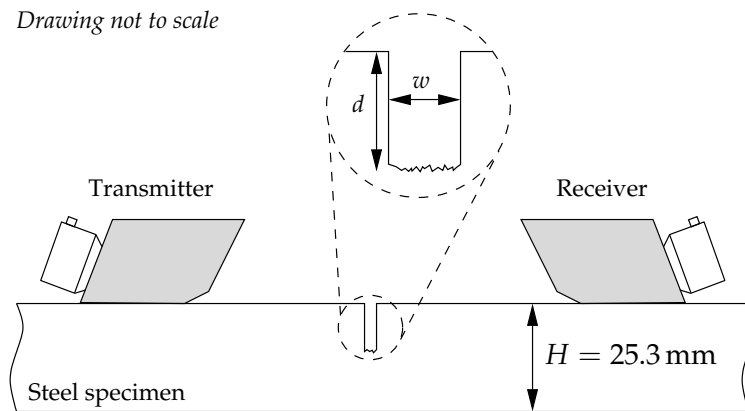


**Figure 4.2:** Ultrasonic examination of notches in test specimen

with their front surfaces at equal distances to the notch. The sides of the wedges are aligned with the help of the edge of a second steel plate in order to ensure that the acoustical axes of both transducers are coplanar. Aligned that way, the transducers are moved in the direction perpendicular to the notches, while the transmitting transducer generates a wave burst signal. The amplified output of the receiving transducer is monitored on the oscilloscope. When the acoustical axes of the transducers align with the middle of the notch, the signal amplitude of the first arriving signal is observed to be minimal. The wedge positions for each minimum are marked, so that the measurements with the prototype device can be taken with the wedges at the same positions. The oscilloscope is switched from sample to average mode, in which multiple measurements are averaged. This cleans up the signal and attenuates noise. As long as the oscilloscope is always triggered at the same moment – which is achieved by feeding the trigger output of the signal generator into the trigger input of the oscilloscope – no distortion of the original signal is

to be expected (given that the measurement responses are time-invariant).

As described in Chapter 3.2, couplant oil is added between the bottom surface of the wedges and the specimen to compensate for surface irregularities and to ensure acoustic coupling. Adhesive forces, which act between the thin couplant layers and the wedges, and also between the couplant layer and the steel specimen, hold the wedges in place during measurements. No additional clamping mechanism is employed. To attain a comparable thickness of the couplant layer among different measurements, a sufficient amount of oil couplant is added between the wedge and the specimen, and the wedge is pressed down hand-tight so that superfluous couplant oil is pressed out to the sides. The adhesive forces of the remaining layer of couplant oil affix the wedge to the specimen. This ensures a consistent contact during the measurement of different notches, among which the wedges have to be relocated on the specimen.

#### ***4.2 Results of Measurements Taken with Commercial Ultrasonic Equipment***

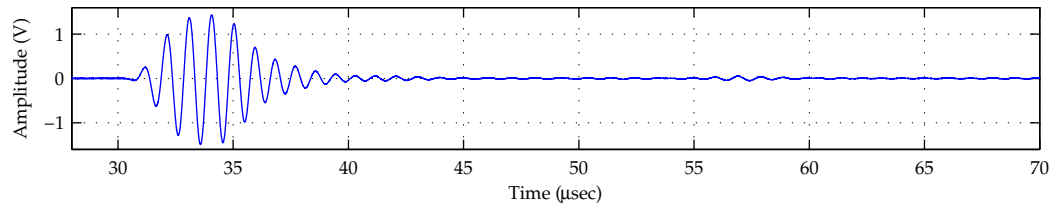
Figure 4.3 shows the time domain signals recorded during the ultrasonic measurements of the notches in the specimen using commercial equipment. For these measurements, the wave generating transducer is driven with a burst of four cycles. The received signal is amplified with a gain of 12 dB. The distance between the front of the bottom surfaces of the wedges and each notch during a measurements is 10 mm. When comparing the time scales of Figure 4.3 to the propagation distance of the waves in steel, bear in mind that the signals need about  $23.3 \mu\text{s}$  to travel the distance inside the wedges. The following propagation paths can be distinguished in the time domain based on the arrival time of the signals:

**after 31  $\mu\text{s}$ :** creeping Rayleigh wave originating from the main signal, which travels along the vertical surfaces and the rim of the notch;

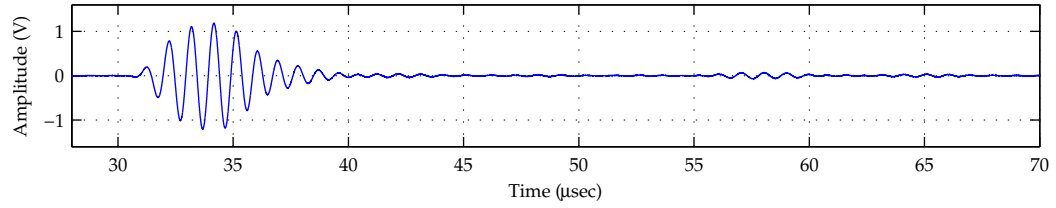
**after 47  $\mu\text{s}$ :** bottom reflection of the mode converted shear wave;

**after 55  $\mu\text{s}$ :** creeping Rayleigh wave originating from signal reflections inside the wedge;

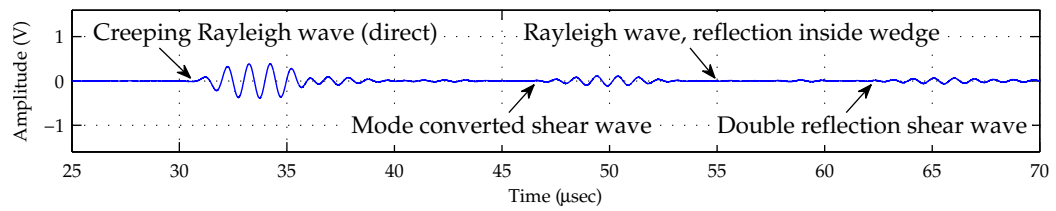
**after 63  $\mu\text{s}$ :** bottom-surface-bottom reflected mode converted shear wave.



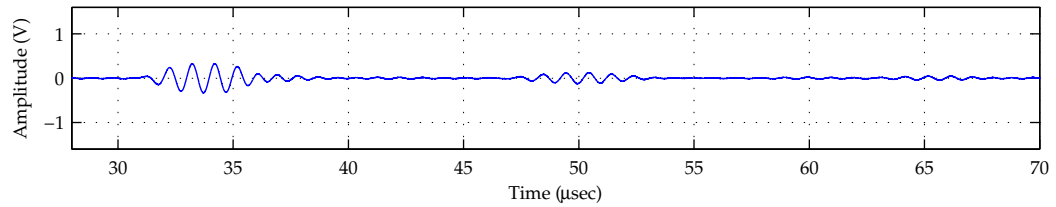
(a) undamaged specimen



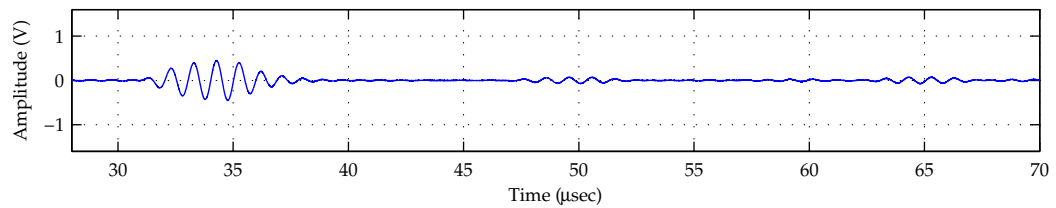
(b) 0.5 mm deep notch



(c) 1.2 mm deep notch



(d) 2.3 mm deep notch



(e) 3.2 mm deep notch

**Figure 4.3:** Ultrasonic measurement signals in the time domain for different notch depths, taken with commercial ultrasonic equipment.

Comparing the time domain signals, it is apparent that the amplitude of the creeping Rayleigh wave signal decreases with increasing depth of the notch when considering notch depths from 0 mm to 2.3 mm, as more energy is reflected back from the notch or converted to a shear wave. The decrease in amplitude between 1.2 mm and 2.3 mm is not as prominent as the decrease from 0.5 mm to 1.2 mm, which is attributed to the exponential decay of stress and displacement with increasing depth, which leads to a similar distribution of the energy. The higher signal amplitude for the 3.2 mm notch compared to the 2.3 mm notch is unexpected given the so far monotonic decrease in the amplitudes, it even exceed the amplitudes of the 1.2 mm notch. One possible explanation for this phenomenon is that the shape of the notch is different from the other notches due to tolerances in the EDM manufacturing process. However, as to obtain a quantitative relation between notch/crack shape and the resulting signals is beyond the scope of this study, this unexpected behavior has not yet been examined in detail.

About  $47 \mu\text{s}$  after the start of the measurement, the mode-converted bottom reflection signal arrives. Its amplitude increases with increasing notch depth for the first four measurements. The differences between the signal amplitudes are not as prominent as for the first (Rayleigh) wave signal. Again, the 3.2 mm notch opposes this trend, which is as before attributed to a possibly different notch geometry.

For damage assessment, only the direct Rayleigh wave and the mode-converted shear wave signals are considered; the second reflection inside the wedge and multiple shear wave reflections signals are left out of the considerations, as their amplitudes are comparably small and they thus have a poor signal-to-noise ratio (SNR). The observed decrease of the amplitude of the first, direct signal, and the increase of the amplitude of the second, reflected signal suggest to use the ratio of the amplitudes of these two signals to assess material damage.

Several different interpretations can be found for the “amplitude” of a signal, which lead to different amplitude ratios. Possible choices are: the maximum positive peak of

a signal (subsequently termed “max”); the maximum negative signal peak, which corresponds to the minimum value of a signal (thereafter termed “min”); the maximum absolute value of a signal (termed “abs”); and the maximum of the envelope curve obtained from the Hilbert transform (termed “env”). Table 4.2 shows the different amplitude ratios as they are found during two sets of measurements. Except for the last measurement of the 3.2 mm notch, the values are decreasing with increasing depth of the notch. These values support the assumption that the amplitude ratio may be used to assess the severity of damage. However, the scope of the experiments with only four notches, from which one yields contradictory results, certainly is not sufficient to derive a relation between signal ratios and notch depth with the necessary substantiality; the necessary deeper analysis is left to further studies.

### 4.3 Influence of Sampling on the Ultrasonic Signals

As the objective of this study is to investigate how ultrasonic detection techniques can be implemented on a microprocessor, the influence of the changes in the signal caused by sampling and quantization of the values in the ADC is examined. As an example, Figure 4.4 shows the ultrasonic measurement signal for the 1.2 mm notch as it would

**Table 4.2:** Amplitude ratios, direct signal over mode converted reflected signal for measurements taken with commercial equipment (Figure 4.3 shows time signals from measurement no. 1)

Measurement no.	max/min/ abs/env	Notch depth				
		undamaged	0.5 mm	1.2 mm	2.3 mm	3.2 mm
1	max	70.0	51.6	3.45	2.62	6.33
1	min	74.5	55.1	3.50	2.61	6.28
1	abs	72.8	52.5	3.47	2.61	6.28
1	env	69.5	50.2	3.46	2.60	6.30
2	max	59.7	44.8	3.76	2.62	8.61
2	min	67.2	50.3	3.77	2.66	8.75
2	abs	62.1	45.8	3.77	2.64	8.62
2	env	61.5	43.1	3.76	2.62	8.71

*max* are maximum values of the time domain signal, *min* are minimum values (i.e. the negative values), *abs* uses absolute values, and *env* the envelope curve obtained from the Hilbert transform

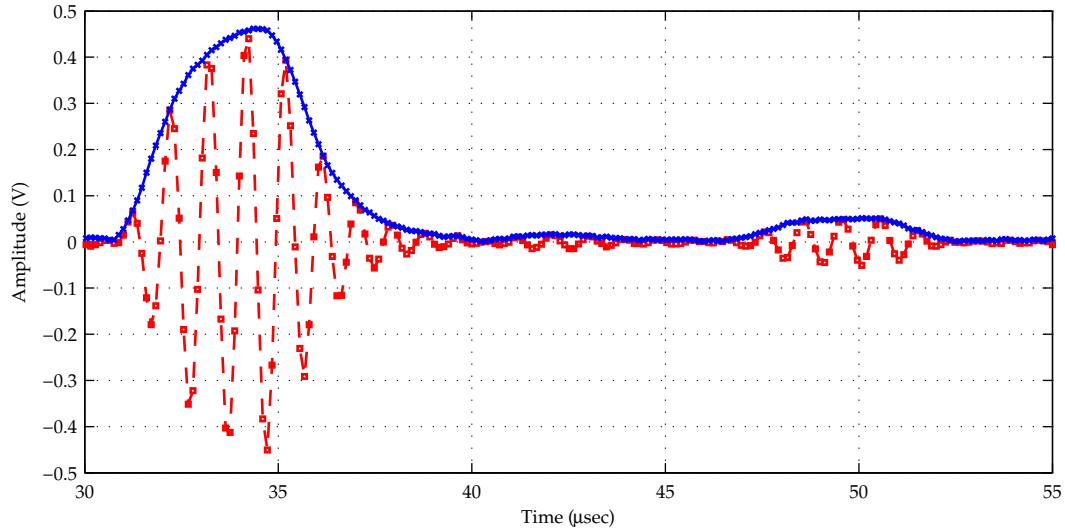


**Figure 4.4:** Downsampled and quantized ultrasonic measurement signal for 1.2 mm deep notch. The envelope signal is obtained from the Hilbert transform of the downsampled signal.

be acquired by the ADC (neglecting the DC offset in the ADC). The original signal shown in Figure 4.3c has been downsampled to match the ADC sampling frequency of 8.3334 MHz, and has been quantized to match the 12 bit resolution, which equals steps of  $\Delta V = 0.733 \text{ mV}$  in voltage (cf. Chapter 2.7.2). The markers show the obtained sampling points, the lines connecting the markers correspond to a linear interpolation of the intermediate values. The envelope curve has been obtained using the Hilbert transform as presented in Chapter 2.8.

In Table 4.3, the amplitudes of the original signal are compared to the amplitudes of two different sets of data derived from the original sequence: the signal termed as “Downsampled” has only been downsampled to match the ADC sampling frequency; the signal termed “+ Quantization” has been downsampled to the ADC sampling frequency and has additionally been quantized to match the 12 bit ADC resolution.

First, compare the relative errors for the downsampled signal to these of the downsampled and quantized signal for the first signal burst. The relative errors are for both maximum-value and envelope-curve based measurements practically identical; they only differ by at most 0.1 percentage points. The minor influence of the quantization error

**Table 4.3:** Comparison of the absolute amplitudes of original vs. downsampled signal for measurement series no. 1

Notch depth	max/env	Signal	Peak amplitude of wave burst (V)				
			Original	Downsampled	Error (%)	+ Quantization	Error (%)
undamaged	max	first	1.435	1.355	5.61	1.355	5.61
0.5 mm			1.185	1.137	4.05	1.138	4.02
1.2 mm			0.386	0.381	1.50	0.380	1.57
2.3 mm			0.331	0.318	3.71	0.318	3.81
3.2 mm			0.449	0.437	2.49	0.437	2.50
undamaged		second	0.021	0.019	8.76	0.019	7.11
0.5 mm			0.023	0.022	5.10	0.022	4.31
1.2 mm			0.112	0.101	9.98	0.100	10.3
2.3 mm			0.126	0.125	0.87	0.125	0.71
3.2 mm			0.071	0.068	3.53	0.068	3.92
undamaged	env	first	1.497	1.494	0.22	1.494	0.22
0.5 mm			1.210	1.205	0.37	1.205	0.39
1.2 mm			0.391	0.389	0.51	0.390	0.46
2.3 mm			0.334	0.333	0.32	0.333	0.36
3.2 mm			0.459	0.457	0.27	0.457	0.34
undamaged		second	0.022	0.020	9.40	0.020	8.73
0.5 mm			0.024	0.023	5.56	0.023	4.86
1.2 mm			0.113	0.111	1.46	0.113	1.17
2.3 mm			0.128	0.125	2.46	0.125	2.32
3.2 mm			0.073	0.070	4.38	0.068	4.18

*max* are maximum values of the time domain signal, *env* uses the envelope curve obtained from the Hilbert transform. Errors figures are calculated with higher precision and then rounded to the used precision, thus they don't directly match the listed rounded absolute values.

on the relative errors is not surprising considering that the signal amplitudes of the first signals are 500 and more times the quantization error. For the second signal burst with much lower signal amplitudes, the changes in the relative error caused by the quantization is higher, as the quantization steps remain unchanged but the signal amplitudes are lower. However, the maximum difference in the relative errors caused by quantization counts only 0.7 percentage points. Thus, most of the error introduced by downsampling and quantization must be attributed to the downsampling in time, the influence of the quantization is minor.

Next, compare the relative errors for the maximum-value based measurements to these of the envelope curve based measurements. For the first signal burst, the relative error of the amplitudes in the *max* measurement is found to be between 1.50 % and 5.61 % for both the non-quantized and the quantized signals. Comparing these values to the relative errors for the envelope-curve based detection, which are at most 0.51 %, confirms the prior made assumption that the envelope-curve of a downsampled signal can be used to obtain the original signal amplitudes with good accuracy – at least for the first wave burst. For the second signal burst, the relative errors of the sampled signal are significantly higher, and are up to nearly 10% for both the maximum-value and the envelope-curve based methods. In this case no method is preferable over the other. The higher relative errors are attributed to the presence of noise in the measured signal. The influence of noise on the second signal is more severe than its influence on the first signal, as the signal amplitudes are lower. The influence of noise on the measurements and the found amplitudes may be reduced by employing digital filter techniques.

The amplitude ratios that correspond to the presented measurements are shown in Table 4.4. The relative error in the amplitude ratios obtained from the downsampled signal compared to the ratios obtained from the original signal is up to 10.1 %. This error is not surprising, as both the amplitude of the first and the second signal, which are used to calculate the amplitude ratio, have errors compared to the original signal as discussed before. These uncertainties have to be taken into account for any damage assessment method that is based on the signal amplitudes.

**Table 4.4:** Comparison of the amplitude ratios original vs. downsampled signal for measurement series no. 1

Notch depth	max/env	Original signal	Downsampled signal	Error (%)	Downsampled and quantized signal	Error (%)
undamaged	max	70.0	72.4	3.46	71.1	1.62
0.5 mm		51.6	52.2	1.11	51.8	0.31
1.2 mm		3.45	3.78	9.43	3.79	9.74
2.3 mm		2.62	2.54	2.87	2.54	3.12
3.2 mm		6.33	6.39	1.07	6.42	1.48
undamaged	env	69.5	76.5	10.1	76.0	9.31
0.5 mm		50.2	52.9	5.49	52.5	4.73
1.2 mm		3.46	3.49	0.96	3.49	0.72
2.3 mm		2.60	2.66	2.2	2.66	2.01
3.2 mm		6.30	6.57	4.29	6.56	4.00

*max* are maximum values of the time domain signal, *env* uses the envelope curve obtained from the Hilbert transform. Errors figures are calculated with higher precision and then rounded to the used precision, thus they don't directly match the listed rounded absolute values.

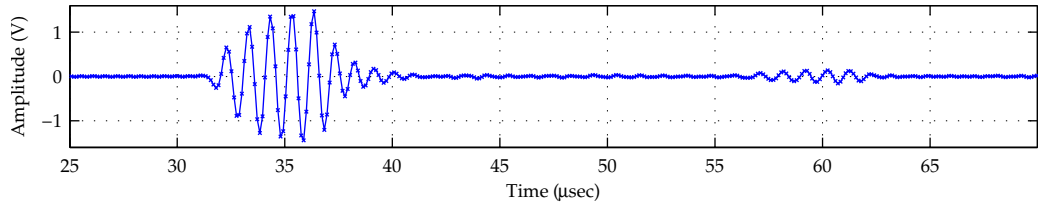
#### *4.4 Results of Measurements Taken with the Prototype Device*

For the measurements that are taken with the prototype device, a burst of five cycle is used to drive the transducer. As the implemented output amplification circuit for the prototype device is not able to generate a symmetric output signal (cf. Chapter 2.6.3), the transducer is driven by a purely positive output burst of 0–32 V. The gain of the signal conditioning circuit and the DC offset are adjusted, so that the received signals that are obtained for an undamaged specimen make use of nearly the full ADC input range without being saturated. The wedges are set up at a distance of 10 mm to the notches. Figure 4.5 shows the acquired signals for different notch depths. The DC offset has been subtracted from the samples to allow for a comparison with the results from the measurements with commercial equipment.

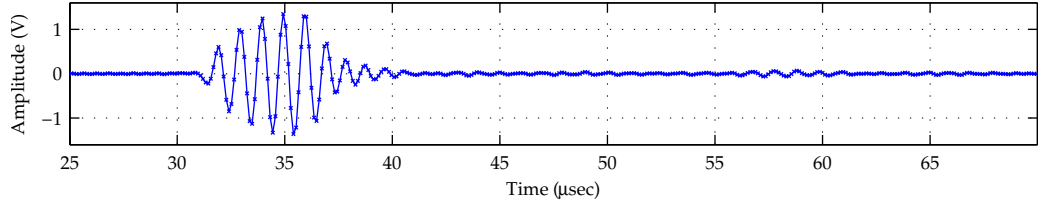
The acquired signals show the same features as the measurement results taken with commercial ultrasonic equipment. The different propagation paths can be distinguished as indicated in Figure 4.5c. The amplitude of the signals show the same qualitative behavior as in the earlier presented results. The amplitudes of the creeping, direct Rayleigh wave decreases with increasing notch depth, and the amplitude of the mode converted shear wave increases with increasing notch depth. The signal obtained from the 3.2 mm notch opposes these trends, which is also consistent with the earlier presented results, and therefore is again attributed to a possibly different notch geometry.

Table 4.5 lists the amplitude ratios for the measurements taken with the prototype device. The ratios decrease with increasing notch depth, which – within the limited scope of the experiments conducted – suggests, that the amplitude ratio can also be used as criterion to evaluate notches with the ultrasonic device.

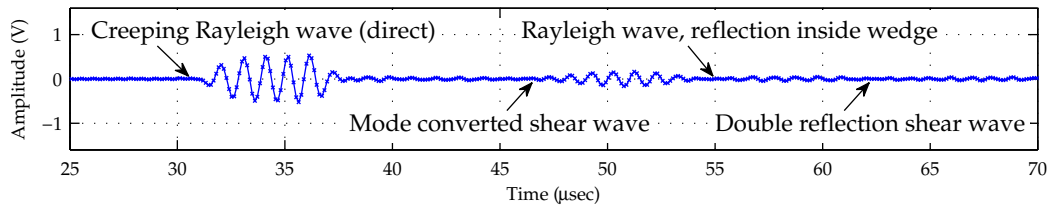
The amplitude ratios, which are found for the undamaged and the 0.5 mm deep notch, are about 20–30 % smaller than the corresponding amplitude ratios that have been obtained using commercial ultrasonic equipment (cf. Table 4.2). This difference is attributed to the higher noise level in the signals acquired by the prototype device, which mainly affects the weak bottom reflection signal. For the next two notches of 1.2 mm and 2.3 mm in



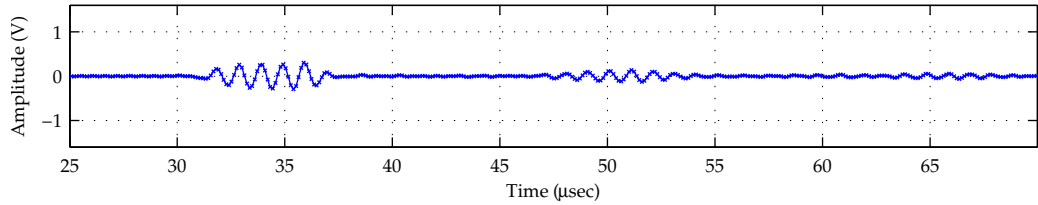
(a) undamaged specimen



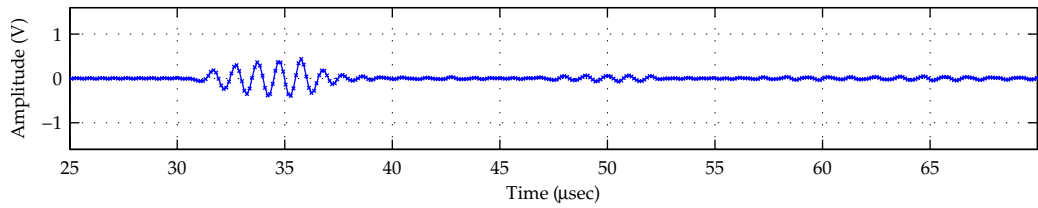
(b) 0.5 mm deep notch



(c) 1.2 mm deep notch



(d) 2.3 mm deep notch



(e) 3.2 mm deep notch

**Figure 4.5:** Ultrasonic measurement signals in the time domain for different notch depths, taken with the prototype device. The markers indicate the sampling points.

**Table 4.5:** Amplitude ratios, direct signal over mode converted reflected signal for measurements taken with the prototype device (Figure 4.5 shows the corresponding time domain signals)

max/min/ abs/env	undamaged	Notch depth			
		0.5 mm	1.2 mm	2.3 mm	3.2 mm
max	47.1	35.0	3.28	2.20	6.36
min	51.4	44.8	3.24	2.53	5.48
abs	47.1	35.4	3.26	2.20	6.13
env	45.5	36.0	3.24	2.22	6.13

depth, the difference decreases, and for them is on the order of 10–15%. For these notches, the amplitude of the bottom reflection is larger, and the influence of the measurement noise therefore decreases. The 3.2 mm notch is not considered in the comparison, as for this notch no consistent results could be obtained using the commercial ultrasonic equipment.

## CHAPTER V

### CONCLUSION AND FURTHER WORK

This chapter summarizes the research conducted and gives an outlook on future work. It also describes the impact of the research.

#### *5.1 Conclusion*

This research examines the applicability of continuous ultrasonic monitoring of surface notches in steel using a small, battery-powered, self-contained device. Ultrasonic monitoring techniques are local approaches that can serve as a supplement to existing global structural health monitoring (SHM) techniques. Global techniques are able to detect severe large-scale damage of a structure, but are insensitive to smaller local damage until this damage grows to an extent where it can severely affect the safety of the entire structure. The continuous health monitoring of civil structures is necessary due to their age and present shape, as demonstrated by the presented statistical data about the decay of bridges in the U.S. Monitoring of local damage in such aged in-service structures is essential in order to avoid the often fatal consequences associated with failures of such structures, which can arise from undetected growth of initially small damages in safety-critical parts.

In this study, Rayleigh waves with a frequency of 1 MHz are used for the ultrasonic monitoring. A hardware and software design for generating and detecting these waves is proposed. The device includes a data acquisition unit, which samples data at a sampling rate of 8.3334 MHz with 12 bit resolution. This sampling frequency is sufficiently high to digitize the band limited signal output of the used narrowband transducer and to acquire all information provided in these signals. However, as the sampling frequency is not significantly higher than the signal frequencies, the influences of the sampling on the signal can not be neglected in the time domain. Signals measured with commercial

equipment, which are then downsampled and quantized to match the characteristics of the analog-digital converter in the device, demonstrate the influence of sampling. The analysis of these signals illustrates that frequency-based data evaluation methods are preferable to time-based methods in the given configuration as they yield a better precision. Using the implemented FFT algorithm, frequency domain information can be obtained from the data. For the reasons stated before, the implemented data processing method, which includes an algorithm to extract wave bursts from the signals for efficient data compression before transmission, are frequency-based algorithms. It is concluded, that the influence of the sampling has to be taken into account for the development of algorithms for autonomous damage assessment, and that the influences are significantly less in the frequency domain.

For the amplification of the relatively weak measured ultrasonic signal, a signal conditioning circuit has been proposed. Powered by two 9 V block batteries, this circuit is well-suited to sufficiently amplify the detected Rayleigh wave signals so that the amplified signals span nearly the full ADC input range. This decreases the effects that distortions, which are inherent to sampling operations, have on the quality of the sampled signals. Output signal generation, however, still remains one of the major challenges for the device. This study proposes an output boost circuit, which is suitable to generate ultrasonic wave signals from the square wave burst output of the pulse-width-modulation interface to drive the transducer. This demonstrates that ultrasonic experiments can be conducted with such a small device, under the limitation of battery power. However, the circuit's output is confined to positive voltages only, it is not able to generate the desired symmetric output signal. The DC offset is undesirable as it causes additional dissipative power losses in the circuit. Thus, improvements to the signal generation circuit should be one of the main objectives of future research.

This study also presents a contact wedge method to generate Rayleigh surface waves in steel. Rayleigh waves have the advantage of a lower geometric attenuation over bulk waves, as their energy is confined to a small layer at the surface, and so only spreads in two instead of three dimensions as is the case for bulk wave. The method presented for

Rayleigh wave generation is very efficient, which enables ultrasonic measurements that have excitation voltages significantly lower than the otherwise typical voltage spikes of often more than 100 V generated by commercial equipment.

Communication of the device with a central server is realized using a wireless connection, which can send data over a distance of up to 300 m. The wireless transmission channel eliminates the need to run long cables on the structure, which is a very time-consuming and costly process. All communication is initiated by a central server, and the ultrasonic detection device acts upon the server's requests. With the communication scheme presented, an operator with a laptop, to which a matching wireless transceiver is connected, can query measurement results from an ultrasonic device when he is in an adequate range, which can for example mean while he drives over a bridge that is equipped with the devices. This saves a considerable amount of time and money compared to manual local inspections, for which the inspector has to reach the location of the damage. In the long term, when autonomous damage assessment is implemented on the device, the central server could be a stationary computer connected to the power grid or some other reliable power source, which queries all the devices installed on a structure, and transmits the data or possibly found alerts on telephone lines or via cell phone to maintenance personnel, which can then react in a timely manner.

## ***5.2 Outlook on Further Work***

The results from this study serve as first step and basis towards the development of a fully autonomous ultrasonic detection device. All parts are now designed and assembled in order to show the feasibility of ultrasonic monitoring using such a device. Every part on its own may be reconsidered in order to reduce power consumption, or increase the signal-to-noise ratio for the signals. Besides eradicating the remaining limitations of the output boost circuit, it will also be interesting to investigate other ways by which the amplitudes of the output amplification circuit can be increased without consuming excessive amount of energy, in order to get stronger signals. Signal generation circuits could also operate independently from the PWM module, however for any method a reliable

synchronization of the sampling with the start of the output signal must be ensured.

The power consumption of the devices used in this study has been analyzed using the characteristics given in the data sheets and using measured data. As energy is limited due to the use of batteries, future research should also consider possibilities to further reduce the current drawn from the device. For the microprocessor and wireless communication module, using sleep states and turning off unnecessary peripherals will help to reduce the power consumption. The external circuits could be modified to include electrical switches like contactors or transistors, which disconnect the battery supply from the electronics and so completely switch off the circuits while they are not used for measurements. Also, power harvesting technologies like the use of ambient vibrations and solar panels are worth investigating.

The measurements taken in this study serve as a proof-of-concept for the proposed ultrasonic examination technique. A more thorough examination of the device's performance during measurements of real crack growth is still pending. The experiences gained from such experiments will also give important feedback for further improvements of the device. Also, the effect of longer propagation distances between the wedges has to be considered in future experiments.

The scope of this study includes qualitative considerations of the scattered wave field of Rayleigh waves, and measurement data obtained from a small number of different samples. For a completely autonomous damage assessment, methods have to be investigated which allow a quantitative evaluation of the dimensions of notches or cracks based on the measured signals, or which at least can evaluate the severity of damage. Such methods have to be tested in experiments, which consider more notches than examined in this study to deduce assertions with the necessary substantiality.

With the possible spread of such local ultrasonic detection devices over a structure in the future, message relay methods and intercommunication between nodes will be of interest to extend the possible communication range.

### ***5.3 Contribution and Impact***

The research conducted in this study contributes to the efforts of improving the safety and reliability of civil structures. The development of a system for continuous and autonomous monitoring of the local damage at critical points in civil structures helps to detect critical conditions in-time, and to take measures to avoid catastrophic failures with their associated consequences, which often include a significant number of casualties.

## APPENDIX A

### ANALYSIS OF THE SIGNAL CONDITIONING CIRCUIT

#### A.1 Non-inverting Amplifier with Offset Correction

Figure A.1 shows the non-inverting amplifier stage. The potentiometers  $R_2$  and  $R_5$  have been replaced by equivalent resistances. Applying Kirchoff's current law to the voltage divider formed by the potentiometer  $R_2$  yields

$$\frac{+V - V_{\text{wiper}}}{(1 - \alpha)R_2} + \frac{-V - V_{\text{wiper}}}{\alpha R_2} = \frac{V_{\text{wiper}} - v_i}{R_3} \quad (\text{A.1})$$

and also

$$\frac{V_{\text{wiper}} - v_i}{R_3} = \frac{v_i}{R_4} + \frac{v_i - v_1}{\beta R_5}. \quad (\text{A.2})$$

Solving the last equation for  $V_{\text{wiper}}$  yields

$$V_{\text{wiper}} = v_i \left( \frac{R_3}{R_4} + \frac{R_3}{\beta R_5} + 1 \right) - v_1 \frac{R_3}{\beta R_5}. \quad (\text{A.3})$$

Equation (A.1) can be rewritten as

$$\left[ (1 - \alpha)\alpha R_2 + R_3 \right] V_{\text{wiper}} = (2\alpha - 1)R_3 V + (1 - \alpha)\alpha R_2 v_i, \quad (\text{A.4})$$

and combining this equation with Equation (A.3) and solving for  $v_1$  yields

$$v_1 = -\frac{(2\alpha - 1)\beta R_5}{(1 - \alpha)\alpha R_2 + R_3} V + \left[ \frac{\beta R_5}{(1 - \alpha)\alpha R_2 + R_3} + \frac{\beta R_5}{R_4} + 1 \right] v_i. \quad (\text{A.5})$$

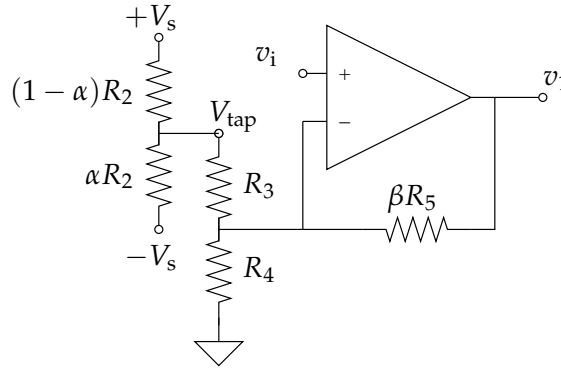


**Figure A.1:** Amplifier with offset correction, potentiometers have been redrawn as resistors with variable values

## A.2 Lowpass Filter

Using Kirchhoff's current law, the following relation between the voltages  $v_1$  and  $v_2$  in the filter stage shown in Figure A.2a can be found:

$$\frac{v_2 - v_1}{R_6} = \frac{v_2}{\frac{1}{j\omega C_4}}. \quad (\text{A.6})$$

Solving this equation for  $v_2/v_1$  yields the frequency response characteristic

$$\frac{v_2}{v_1} = G_{\text{filt},1}(j\omega) = \frac{1}{j\omega R_6 C_4 + 1}. \quad (\text{A.7})$$

For the analysis of the active two-pole filter stage shown in Figure A.2b, the op-amp is assumed to be ideal. Thus, the voltage at its positive and negative input pin will always be equal, and due to the feedback from the output, these voltages will always equal  $v_3$ . Kirchhoff's current law yields

$$\frac{v_c - v_3}{R_7} = \frac{v_c - v_3}{\frac{1}{j\omega C_6}} + \frac{v_c - v_3}{R_8} = (v_c - v_3) \left( j\omega C_6 + \frac{1}{R_8} \right) \quad (\text{A.8})$$

and

$$\frac{v_c - v_3}{R_8} = \frac{v_3}{\frac{1}{j\omega C_5}} = j\omega C_5 v_3, \quad \Leftrightarrow \quad v_c = (1 + j\omega R_8 C_5) v_3. \quad (\text{A.9})$$

Plugging the last equation into Equation (A.8) and solving for  $v_3/v_2$  yields the frequency response

$$\frac{v_3}{v_2} = G_{\text{filt},2}(j\omega) = \frac{1}{(j\omega)^2 R_7 R_8 C_5 C_6 + j\omega (R_7 + R_8) C_5 + 1}. \quad (\text{A.10})$$

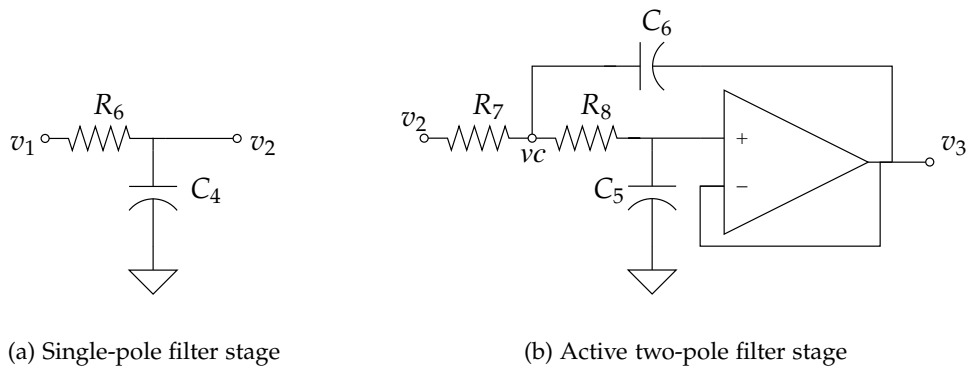


**Figure A.2:** Filter circuits

## APPENDIX B

### PROGRAM CODE

```
#define SWAP(a,b) tempr = (a);(a) = (b);(b)=tempr
Uin16 m, i, j, n2, n4;          // unsigned 16 bit integer
float64 tempr;                 // 64 bit floating point number

n2 = Nc>>1;
n4 = n2 >> 1;
j = 0;

for(i = 0; i <= n2-2; i+=2)
{
    if (i < j)
    {
        SWAP(input[2*i],input[2*j]);
        SWAP(input[2*i+1],input[2*j+1]);
        SWAP(input[2*(i+n2+1)],input[2*(j+n2+1)]);
        SWAP(input[2*(i+n2+1)+1],input[2*(j+n2+1)+1]);
    }
    SWAP(input[2*(i+1)],input[2*(j+n2)]);
    SWAP(input[2*(i+1)+1],input[2*(j+n2)+1]);

    m = n4;

    while( m <= j)
    {
        j -= m;
        m >>= 1;
    }
    j += m;
}
```

**Figure B.1:** Yong's [53] bit reversal algorithm, adapted for complex numbers

```

mmax = 2;
while (mmax < 2*N)
{
    istep = 2*mmax;

     $w_p = \exp\left(\mp \frac{2\pi i}{mmax}\right)$ ; /* implemented using lookup-table */
    w = 1;

    for (m = 0; m < mmax; m += 2)
    {
        for(i=m; i<n; i+=istep)
        {
            /*FFT butterfly*/
            j = i + mmax;
            input[j] = input[i] - w × input[j];
            input[i] = input[i] + w × input[j];
        }

        w = w × wp; /*update the fft exponential*/
    }
    mmax = 2*mmax;
}

```

**Figure B.2:** Pseudo-code for the complex FFT algorithm

## REFERENCES

- [1] ACHENBACH, J. D., *Wave Propagation in Elastic Solids*. North-Holland, 1995.
- [2] ACHENBACH, J., "Quantitative nondestructive evaluation," *International Journal of Solids and Structures*, vol. 37, pp. 13–27, 2000.
- [3] ALTER, D. M., "Using PWM output as a digital-to-analog converter on a TMS320F280x digital signal controller." <http://focus.ti.com/lit/an/spraa88a/spraa88a.pdf>, September 2008. SPRAA88A, Last accessed: 08/16/2009.
- [4] AULD, B. A., "General electromechanical reciprocity relations applied to the calculation of elastic wave scattering coefficients," *Wave Motion*, vol. 1, no. 1, pp. 3 – 10, 1979.
- [5] BEDROSIAN, E., "A product theorem for Hilbert transforms," *Proceedings of the IEEE*, vol. 51, pp. 868–869, 1963.
- [6] BERMES, C., "Generation and detection of nonlinear Lamb waves for the characterization of material nonlinearities," Master's thesis, Georgia Institute of Technology, School of Civil and Environmental Engineering, 2005.
- [7] ÇELEBI, M., "Seismic instrumentation of buildings (with emphasis on federal buildings)." USGS Project no.: 0-7460-68170, United States Geological Survey (MS977), Menlo Park, CA, USA, November 2002.
- [8] CHANG, P. C., FLATAU, A., and LIU, S. C., "Review paper: Health monitoring of civil infrastructure," *Structural Health Monitoring*, vol. 2, pp. 257–267, 2003.
- [9] COOK, D. A. and BERTHELOT, Y. H., "Detection of small surface-breaking fatigue cracks in steel using scattering of Rayleigh waves," *NDT&E International*, vol. 34, pp. 483–492, 2001.
- [10] DIGI INTERNATIONAL INC., "Application note – 900 MHz vs 2.4 GHz." <http://www.digi.com/support/kbase/kbaseresultdet1.jsp?kb=64>. Last accessed: 07/25/2009.
- [11] ELGAMAL, A., CONTE, J. P., MASRI, S., FRASER, M., FOUNTAIN, T., GUPTA, A., TRIVEDI, M., and ZARKI, M. E., "Health monitoring framework for bridges and civil infrastructure," in *Structural Health Monitoring 2003* (CHANG, F.-K., ed.), pp. 123–130, 2003.
- [12] GOLD, B. and RADER, C. M., *Digital Processing of Signals*. New York: McGraw-Hill, 1969 (reprinted 1983).
- [13] GRAFF, K. F., *Wave Motion in Elastic Solids*. Dover publications, 1975.
- [14] HAHN, S. L., *Hilbert Transform in Signal Processing*. Artech House, 1996.
- [15] HERRMANN, J., "Generation and detection of higher harmonics in Rayleigh waves using laser ultrasound," Master's thesis, Georgia Institute of Technology, School of Civil and Environmental Engineering, 2005.

- [16] HOROWITZ, P. and HILL, W., *The Art of Electronics*. New York, NY, USA: Cambridge University Press, 1989.
- [17] JOHNSON, D. and ASSOCIATES, "300V Peak to peak signal generator." <http://www.discovercircuits.com/PDF-FILES/300vpp.pdf>, June 03 2000. Last accessed: 08/16/2009.
- [18] KARP, A. H., "Bit reversal on uniprocessors," *SIAM Rev.*, vol. 38, no. 1, pp. 1–26, 1996.
- [19] KIM, J.-Y. and ROKHLIN, S. I., "Surface acoustic wave measurements of small fatigue cracks initiated from a surface cavity," *International Journal of Solids and Structures*, vol. 39, pp. 1487–1504, 2002.
- [20] KINO, G. S., "The application of reciprocity theory to scattering of acoustic waves by flaws," *Journal of Applied Physics*, vol. 49, no. 6, pp. 3190–3199, 1978.
- [21] KOOPMAN, P. and CHAKRAVARTY, T., "Cyclic redundancy code (CRC) polynomial selection for embedded networks," in *Dependable Systems and Networks, 2004 International Conference on*, pp. 145–154, June-1 July 2004.
- [22] LYNCH, J., WANG, Y., LOH, K., YI, J.-H., and YUN, C.-B., "Performance monitoring of the Geumdang Bridge using a dense network of high-resolution wireless sensors," *Smart Materials and Structures*, vol. 15, no. 6, pp. 1561–1575, 2006.
- [23] MARPLE, JR., S. L., "Computing the discrete-time 'analytic' signal via FFT," *IEEE Trans. Signal Process.*, vol. 47, pp. 2600–2603, Sept. 1999.
- [24] MASSEREY, B. and MAZZA, E., "Characterization of surface cracks using Rayleigh waves," in *Review of progress in quantitative nondestructive evaluation*, vol. 760 of *AIP Conference Proceedings*, pp. 805–812, 2005.
- [25] MAXSTREAM, INC., "XCite™ advanced programming & configuration – advanced manual v1.1." [http://ftp1.digi.com/support/documentation/advancedprogrammingmanual\\_xcite.pdf](http://ftp1.digi.com/support/documentation/advancedprogrammingmanual_xcite.pdf), August 2005. Last accessed: 08/16/2009.
- [26] MAXSTREAM, INC., "9XCite™ OEM RF module product manual v2.1." [http://ftp1.digi.com/support/documentation/productmanual\\_xcite\\_oem\\_rfmodule.pdf](http://ftp1.digi.com/support/documentation/productmanual_xcite_oem_rfmodule.pdf), January 2007. Last accessed: 08/16/2009.
- [27] MENDELSON, D. A., ACHENBACH, J. D., and KEER, L. M., "Scattering of elastic waves by a surface-breaking crack," *Wave Motion*, vol. 2, pp. 277–292, 1980.
- [28] MOCK, G., "Advanced linker techniques for convenient and efficient memory usage." <http://focus.ti.com/lit/an/spraa46a/spraa46a.pdf>, December 2008. SPRAA46A, Last accessed: 08/16/2009.
- [29] MOORE, M., PHARES, B., GRAYBEAL, B., ROLANDER, D., and WASHER, G., "Reliability of visual inspection for highway bridges, volume I: Final report," Technical Report FHWA-RD-01-020, U.S. Department of Transportation, Federal Highway Administration, June 2001.
- [30] NATIONAL SEMICONDUCTOR, "LM7372 Data sheet." <http://www.national.com/ds/LM/LM7372.pdf>, June 24 2008. Last accessed: 08/16/2009.

- [31] OPPENHEIM, A. V., SCHAFER, R. W., and BUCK, J. R., *Discrete-Time Signal Processing (2nd ed.)*. Upper Saddle River, NJ, USA: Prentice-Hall, Inc., 1999.
- [32] PANAMETRICS, "Data sheet ultrasonic transducer A103S," tech. rep.
- [33] PRESS, W. H., TEUKOLSKY, S. A., VETTERLING, W. T., and FLANNERY, B. P., *Numerical Recipes in C (2nd ed.): The Art of Scientific Computing*. New York, NY, USA: Cambridge University Press, 1992.
- [34] PRÜLL, C., "Generation and detection of Lamb waves for the characterization of plastic deformation," Master's thesis, Georgia Institute of Technology, School of Civil and Environmental Engineering, 2007.
- [35] REILLY, A., FRAZER, G., and BOASHASH, B., "Analytic signal generation—tips and traps," *IEEE Trans. Signal Processing*, vol. 42, pp. 3241–3245, Nov. 1994.
- [36] SOHN, H., C.R., F., HUNTER, N., and WORDEN, K., "Structural health monitoring using statistical pattern recognition techniques," *Journal of dynamic systems, measurement, and control*, vol. 123, pp. 706–711, 2001.
- [37] SPECTRUM DIGIAL, INC., "Technical reference eZdsp F28335." <http://focus.ti.com/lit/ds/symlink/tms320f28335.pdf>, 2007. Last accessed: 08/16/2009.
- [38] STRASER, E. G. and KIREMIDJIAN, A. S., "A modular, wireless damage monitoring system for structures." Report No. 128, John A. Blume Earthquake Engineering Center, Department of Civil and Environmental Engineering, Stanford University, Stanford, CA, November 1998.
- [39] TEXAS INSTRUMENTS, "Data manual TMS320F28335/28334/28332." <http://focus.ti.com/lit/ds/symlink/tms320f28335.pdf>, Sept. 2008. SPRS439E, Last accessed: 08/16/2009.
- [40] TEXAS INSTRUMENTS, "Running an application from internal flash memory on the TMS320F28xxx DSP." <http://focus.ti.com/lit/an/spra958h/spra958h.pdf>, Sept. 2008. Application Report, SPRA958H, Last accessed: 08/16/2009.
- [41] TEXAS INSTRUMENTS, "TMS320x2833x, 2823x Enhanced pulse width modulator (ePWM) module." <http://focus.ti.com/lit/ug/sprug04a/sprug04a.pdf>, October 2008. SPRUG04A, Revised July 2009, Last accessed: 08/16/2009.
- [42] TEXAS INSTRUMENTS, "TMS320x2833x, 2823x System control and interrupts reference guide." <http://focus.ti.com/lit/ug/sprufb0c/sprufb0c.pdf>, May 2009. Last accessed: 08/16/2009.
- [43] U.S. DEPARTMENT OF TRANSPORTATION, FEDERAL HIGHWAY ADMINISTRATION, "Memorandum: Public disclosure of National Bridge Inventory (NBI) data." <http://www.fhwa.dot.gov/Bridge/nbi/20070517.cfm>. Last accessed: 08/12/2009.
- [44] U.S. DEPARTMENT OF TRANSPORTATION, FEDERAL HIGHWAY ADMINISTRATION, "National bridge inventory 2008 data (ASCII files)." <http://www.fhwa.dot.gov/Bridge/nbi/ascii.cfm?year=2008>. Last accessed: 08/16/2009.

- [45] U.S. DEPARTMENT OF TRANSPORTATION, FEDERAL HIGHWAY ADMINISTRATION, "Deficient bridges by state and highway system as of december 2008." <http://www.fhwa.dot.gov/Bridge/nbi/defbr08.cfm>, February 2009. Last accessed: 08/12/2009.
- [46] U.S. DEPARTMENT OF TRANSPORTATION, FEDERAL HIGHWAY ADMINISTRATION, "FHWA bridge programs structure type by year built." <http://www.fhwa.dot.gov/Bridge/structyr.cfm>, February 2009. Last accessed: 08/12/2009.
- [47] U.S. DEPARTMENT OF TRANSPORTATION, FEDERAL HIGHWAY ADMINISTRATION, FEDERAL TRANSIT ADMINISTRATION, "2006 status of the nation's highways, bridges, and transit: Conditions & performance." Report to Congress, Executive Summary, 2006.
- [48] VIKTOROV, I. A., *Rayleigh and Lamb Waves – Physical Theory and Applications*. Plenum Press, New York, 1967.
- [49] WANG, Y., LOH, K., LYNCH, J., FRASER, M., LAW, K., and ELGAMAL, A., "Vibration monitoring of the Voigt Bridge using wired and wireless monitoring systems," in *Proceedings of the 4th China-Japan-US Symposium on Structural Control and Monitoring*, (Hangzhou, China), October 16–17 2006.
- [50] WANG, Y., LYNCH, J., and LAW, K., "Design of a low-power wireless structural monitoring system for collaborative computational algorithms," in *Proceedings of SPIE 10th Annual International Symposium on Nondestructive Evaluation for Health Monitoring and Diagnostics*, vol. 5768, (San Diego, CA), pp. 106–117, March 6–10 2005.
- [51] WANG, Y., LYNCH, J. P., and LAW, K. H., *Wireless Sensing, Actuation and Control – With Applications to Civil Structures*. Lecture Notes in Computer Science, Springer Berlin / Heidelberg, 2006.
- [52] WANG, Y., LYNCH, J. P., and LAW, K. H., "A wireless structural health monitoring system with multithreaded sensing devices: Design and validation," *Structure and Infrastructure Engineering*, vol. 3, pp. 103–120, June 2007.
- [53] YONG, A. A., "A better FFT bit-reversal algorithm without tables," *IEEE Trans. Signal Process.*, vol. 39, no. 10, pp. 2365–2367, 1991.